NASA/TP-2008-215536

Applications of a Forward-Looking Interferometer for the On-board Detection of Aviation Weather Hazards

Leanne West and Gary Gimmestad
Georgia Tech Research Institute, Atlanta, Georgia

William "Bill" Smith and Stanislav Kireev
Hampton University, Hampton, Virginia

Larry B. Cornman
National Center for Atmospheric Research, Boulder, Colorado

Philip R. Schaffner and George Tsoucalas
Langley Research Center, Hampton, Virginia

October 2008

The NASA STI Program Office . . . in Profile

Since its founding, NASA has been dedicated to the advancement of aeronautics and space science. The NASA Scientific and Technical Information (STI) Program Office plays a key part in helping NASA maintain this important role.

The NASA STI Program Office is operated by Langley Research Center, the lead center for NASA's scientific and technical information. The NASA STI Program Office provides access to the NASA STI Database, the largest collection of aeronautical and space science STI in the world. The Program Office is also NASA's institutional mechanism for disseminating the results of its research and development activities. These results are published by NASA in the NASA STI Report Series, which includes the following report types:

- TECHNICAL PUBLICATION. Reports of completed research or a major significant phase of research that present the results of NASA programs and include extensive data or theoretical analysis. Includes compilations of significant scientific and technical data and information deemed to be of continuing reference value. NASA counterpart of peer-reviewed formal professional papers, but having less stringent limitations on manuscript length and extent of graphic presentations.

- TECHNICAL MEMORANDUM. Scientific and technical findings that are preliminary or of specialized interest, e.g., quick release reports, working papers, and bibliographies that contain minimal annotation. Does not contain extensive analysis.

- CONTRACTOR REPORT. Scientific and technical findings by NASA-sponsored contractors and grantees.

- CONFERENCE PUBLICATION. Collected papers from scientific and technical conferences, symposia, seminars, or other meetings sponsored or co-sponsored by NASA.

- SPECIAL PUBLICATION. Scientific, technical, or historical information from NASA programs, projects, and missions, often concerned with subjects having substantial public interest.

- TECHNICAL TRANSLATION. English-language translations of foreign scientific and technical material pertinent to NASA's mission.

Specialized services that complement the STI Program Office's diverse offerings include creating custom thesauri, building customized databases, organizing and publishing research results ... even providing videos.

For more information about the NASA STI Program Office, see the following:

- Access the NASA STI Program Home Page at ***http://www.sti.nasa.gov***

- E-mail your question via the Internet to help@sti.nasa.gov

- Fax your question to the NASA STI Help Desk at (301) 621-0134

- Phone the NASA STI Help Desk at (301) 621-0390

- Write to:
  NASA STI Help Desk
  NASA Center for AeroSpace Information
  7115 Standard Drive
  Hanover, MD 21076-1320

NASA/TP-2008-215536

Applications of a Forward-Looking Interferometer for the On-board Detection of Aviation Weather Hazards

Leanne West and Gary Gimmestad
Georgia Tech Research Institute, Atlanta, Georgia

William "Bill" Smith and Stanislav Kireev
Hampton University, Hampton, Virginia

Larry B. Cornman
National Center for Atmospheric Research, Boulder, Colorado

Philip R. Schaffner and George Tsoucalas
Langley Research Center, Hampton, Virginia

National Aeronautics and
Space Administration

Langley Research Center
Hampton, Virginia 23681-2199

October 2008

Available from:

NASA Center for AeroSpace Information (CASI)
7115 Standard Drive
Hanover, MD 21076-1320
(301) 621-0390

National Technical Information Service (NTIS)
5285 Port Royal Road
Springfield, VA 22161-2171
(703) 605-6000

Contents

List of Figures

List of Tables

1 Executive Summary

Under the auspices of the Aviation Safety Program (AvSafe) Integrated Intelligent Flight Deck (IIFD) project, NASA is investigating remote sensors for detection of hazards to aircraft. The Forward-Looking Interferometer (FLI) is a new instrument concept for efficiently obtaining the measurements required to alert flight crews to potential weather hazards to safe flight. To meet the needs of the commercial fleet, such a sensor should address multiple hazards to warrant the costs of development, certification, installation, training, and maintenance. The FLI concept is based on passive radiometric sensing with high-resolution Infrared (IR) Fourier Transform Spectrometry (FTS) technologies that have been developed for satellite remote sensing, in addition to the detection of aerosols and gasses for other purposes. The FLI concept is being evaluated for its potential to address multiple hazards including clear air turbulence (CAT), volcanic ash, wake vortices, low slant range visibility, dry wind shear, and icing, during all phases of flight (takeoff, cruise, and landing). Additional possible applications, not addressed in this study, may include detection of runway contamination; observations of temperature and water vapor for use in weather models; and detection of pollution or other aerosols. The technology might also be applied for downward-looking atmospheric profiling of water vapor, temperature, turbulence or other applications.

Over the years, a large suite of techniques and analytical tools has been developed to assess the potential measurement performance of downward-looking imaging interferometers that were developed for space-based Earth remote sensing. Some of these analytical tools have been applied to an airborne hazard detection feasibility study for CAT, volcanic ash, and low slant range visibility conducted for NASA by the Georgia Tech Research Institute, Hampton University, and the National Center for Atmospheric Research through National Institute of Aerospace Task Order Number, NNL06AB99T. In the feasibility study, remote sensing techniques developed for space-based sensors were applied to aviation hazard detection problems in order to assess the feasibility of using FLI technology for airborne sensors. Sensitivity studies were performed on clear air turbulence, volcanic ash clouds, and for reduced slant range visibility. Characterization studies and literature searches were conducted on wake vortices, dry wind shear, and icing to determine if future sensitivity studies were warranted. Sensitivity studies were conducted using a limited set of temperature, wind, and humidity fields. The studies were performed spectrally with high enough resolution to resolve individual spectral lines of molecules such as CO_2, so as to support the use of interferometric sensors such as the FLI. The simulations were performed for single lines of sight from the sensor to/through the hazards.

The studies were based on a high spectral resolution spherical shell radiative transfer model using LBLRTM (Line-By-Line Radiative Transfer Model) for the molecular optical depths, and values obtained from the literature for volcanic ash and obscurants such as fog and haze. Two different approaches for detecting CAT were considered: detecting temperature disturbances ahead of the aircraft with measurements in the 14 - 15 μm CO_2 spectral band, and detecting water vapor disturbances using wavelengths in the 5 - 8 micron spectral region. For volcanic ash detection, two different algorithms for determining the distance to an aerosol cloud were examined. The algorithms are the "CO_2 Slicing" technique and "Window Channel" technique.

For the improvement of slant range visibility, the use of Empirical Orthogonal Functions (EOF) Regression [also called Principle Components (PC) Regression] was investigated. By definition, the EOFs, or PCs, are statistically optimal in the sense that no other set of spectral functions can be used to represent the observed radiance spectra with as small a number of independent variables. An advantage of using EOF regression is that it enables the entire spectrum of information content to be used for the sensing of these phenomena, thereby multiplexing the emission signals from all the atmospheric gases of interest as well

as those emission signals from clouds and aerosols. By using EOF regression to retrieve the geophysical characteristics of the otherwise small radiance turbulence signal, the signal-to-noise ratio of the FLI detection system may be enhanced by an order of magnitude or more. A similar signal-to-noise advantage could be gained for the detection of other weather related hazards as well.

The physical basis for FLI detection of wake vortices, dry wind shear, and icing has been investigated through literature research to determine whether sensitivity studies are warranted. In all cases, these hazards have phenomenology that should be detectable by an FLI system. Wake vortices may be detectable due to entrained water vapor from the aircraft engine exhaust, lower than ambient core temperature, and/or other entrained gasses; dry wind shear by the cooler temperature of air in a downdraft; and icing by the different optical properties of water and ice in the infrared region.

The initial feasibility studies indicate that the spectral radiance measurements by a FLI mounted on an aircraft should be able to sense or, in the case of reduced visibility, mitigate aviation weather hazards to safe flight. It was shown that, for the case of enhancing slant range visibility, Eigenvector EOF regression is a powerful method for transforming FLI spectra into products that can be used by the flight crew or by automated agents to help insure safe flight. It is likewise expected that EOF regression can be used to enable rapid and accurate predictions of the other aviation safety hazards including turbulence, volcanic ash, wake turbulence, and icing.

Future research needs have been determined to identify the next steps to be taken in the development of a FLI-based comprehensive external hazard monitor. Such future efforts should include both ground- and flight-testing of prototype FLI hardware to collect data for sensor and phenomenological characterization and validation, in addition to the development of means for measuring hazard intensity or estimating the hazard posed to the aircraft and the development of a simulation environment. The next modeling steps in the FLI applications research should be to develop and apply the EOF regression technique to predicting the intensity and distance / warning time for turbulence, volcanic ash, wake turbulence, and icing. The technique should be demonstrated for a wide variety of atmospheric situations to demonstrate the robustness of the algorithm.

CAT and Dry Wind Shear. Sensitivity studies for CAT detection included two techniques: sensing temperature fluctuations using the 650 - 780 cm^{-1} (wavenumbers 6.5 - 7.8 m^{-1}) CO_2 band and sensing water vapor fluctuations in the 1300 - 1600 cm^{-1} (wavenumbers 13 - 16 m^{-1}) region. The simulations revealed detectable signatures in both the interferogram and spectral domains for the CO_2 temperature technique at flight altitudes. Although the maximum detection range appears to be about 5 km (assuming an instrument resolution of 0.3 K), which is not as large as early investigators have claimed. But humidity anomalies in the one case for which data exists were detectable from 30 km, or with a warning time of approximately 2 min, assuming a lower instrument sensitivity of 1.0 K. Wind shear near the ground is associated with the downward motion of cooler air from higher altitudes, and the anomalously low air temperatures should be easily detectable with an FLI during a landing approach.

Volcanic Ash. The ability of an IR imager to distinguish volcanic ash clouds from water and ice clouds was verified in the 800 - 1100 cm^{-1} region, using an ash optical depth spectrum obtained from the literature. The optical properties of volcanic ash produce a large signature in the 8 - 12 cm^{-1} window region, thereby making ash detection possible with the FLI.

Low Visibility. A simulation of multi-band imaging in low slant-range visibility conditions illustrated the potential of the FLI to provide essentially unobscured IR images of

runway scenes as viewed from the air during an approach by making use of multi-spectral information to remove the effects of atmospheric obscurants (e.g. water vapor and aerosols). This capability will give pilots a clear view of runways even when an obscurant such as a ground fog is present, and it will provide high quality images to support automated detection of airborne and ground obstacles or other hazards.

Wake Vortices. Typical wake vortex properties obtained from a literature search included the core temperature as well as the concentrations of exhaust gas constituents (including water vapor) that become entrained in the vortex. Vortex core temperatures have been measured to be several degrees below ambient temperature and this temperature difference should be detectable, which suggests that an FLI will provide real-time imagery of the motion and evolution of wake vortices. The entrained gasses, including water vapor, provide additional means of detection with an FLI. Detection of wake vortices by FLI techniques is possibly the most challenging application considered due to the relatively small size of the phenomena and the geometry of the problem which would have the FLI looking down at a scene with ground, runway, and other objects as background during landing, the phase of flight that would be of most interest.

Icing. The optical properties of liquid water and ice are quite different in the spectral regions where the FLI will operate. This fact will give the FLI a capability to distinguish ice from liquid water on surfaces such as runways. In addition, the FLI may be able to detect icing conditions ahead of an aircraft during flight by discriminating supercooled liquid water drops from ice crystals.

Runway Friction. One significant cause of aircraft accidents is reduced runway friction caused by rain, frost, and snow. A relatively low spectral resolution imaging FLI spectrometer, operating from an aircraft, could be used to detect this hazardous runway condition. Using FLI data, the braking distance can be determined, and used to alert the pilot of a hazardous landing condition.

The sensitivity and characterization studies addressed the phenomenology that supports detection and mitigation by the FLI. Techniques for determining the range, and hence warning time, were demonstrated for several of the hazards, and a table of research instrument parameters was developed for investigating all of the hazards discussed above. This work supports the feasibility of detecting multiple hazards with an FLI multi-hazard airborne sensor, and for producing enhanced IR images in reduced visibility conditions; however, further research must be performed to develop a means to estimate the intensities of the hazards posed to an aircraft and to develop robust algorithms to relate sensor measurables to hazard levels. In addition, validation tests need to be performed with a prototype system. Further research should include ground-based measurements, airborne measurements, additional sensitivity studies, and simulations.

2 Introduction

In the fall of 2005, NASA's Aeronautics Research Mission Directorate (ARMD) initiated a restructuring of its aeronautics program to ensure that it had a strategic plan in place that enables the pursuit of long-term, cutting-edge research for the benefit of the broad aeronautics community. The three principles guiding this restructuring were: 1) NASA will dedicate itself to the mastery and intellectual stewardship of the core competencies of aeronautics in all flight regimes; 2) NASA will focus its research in areas appropriate to its unique capabilities; and 3) NASA will directly address the fundamental research needs of

the Next Generation Air Transportation System (NextGen - formerly known as NGATS) while working closely with its agency partners in the Joint Planning and Development Office (JPDO).

Using the above principles, ARMD established four programs: the Fundamental Aeronautics Program, the Aviation Safety Program (AvSafe), the Airspace Systems Program, and the Aeronautics Test Program. The Fundamental Aeronautics Program conducts cutting-edge research that produces innovative concepts, tools, and technologies that enable the design of vehicles that fly through any atmosphere at any speed. The Aviation Safety Program focuses on developing the cutting-edge tools, methods, and technologies to improve the intrinsic safety attributes of current and future aircraft that will operate in the NextGen. The Airspace Systems Program directly addresses the Air Traffic Management (ATM) research needs of the NextGen initiative as defined by the JPDO. The Aeronautics Test Program ensures the strategic availability and accessibility of a critical suite of aeronautics test facilities that are deemed necessary to meet aeronautics, agency, and national needs.

Both the restructuring of NASA's aeronautics research program and the development of the National Aeronautics R&D Policy took into consideration many of the same reports and studies that have been conducted over the past several years. These reports included the "Final Report of the Commission on the Future of the U.S. Aerospace Industry" by the Aerospace Commission, 2002, "Securing the Future of U.S. Air Transportation: A System in Peril" by the National Research Council (NRC), 2003, and "Wind Tunnel and Propulsion Test Facilities: An Assessment of NASA's Capabilities to Serve National Needs", RAND Corporation, 2003. The use of this supporting information by both parties helped contribute to the alignment of NASA's restructured aeronautics program with the new Aeronautics R&D Policy. In addition, while the recent NRC "Decadal Survey of Civil Aeronautics" (2006) was published after the restructuring of NASA's aeronautics program had begun, NASA's new aeronautics program is very well aligned with the recommendations of that study.

The Aviation Safety Program also conducts research in several critical core aeronautics competencies, including materials and structures, sensors, data mining, flight mechanics, human factors, verification and validation of complex systems, flight dynamics and control, icing physics, and intelligent and adaptive systems. Mastery of these competencies will be critical to our ability to develop innovative concepts, tools, methods, and technologies that will improve the intrinsic safety attributes of current and future aircraft operating in the National Airspace System (NAS). In addition, just as in the Fundamental Aeronautics Program, much of the foundational research conducted in the Aviation Safety program will ultimately have applicability to spacecraft as well as aircraft. For example, research in core areas such as sensors and data mining in the Integrated Vehicle Health Management project may lead to self-healing systems that are applicable not only to aircraft but to spacecraft as well. Foundational research in materials that leads to advances in our understanding of the aging and durability properties of composites and superalloys will have dual aeronautics and space applications. Foundational research in adaptive controls as part of the Integrated Resilient Aircraft Control project will likely find applications in future space missions where vehicles will be required to operate in and adapt to unknown flight environments. Finally, foundational research in human factors, sensors, and human-automation interface modeling will lead to enhancements in crew-vehicle interface technologies that may have applicability to space vehicles as well.

The Aviation Safety Program worked closely with the FAA and the JPDO in developing its research plans with a focus on developing cutting-edge technologies to improve the intrinsic safety attributes of current and future aircraft that will operate in the global NextGen. Furthermore, many of the technologies will have dual-use applications for DOD needs. As such, all four projects within the Aviation Safety Program directly support this

Policy guidance.

Specifically, the Integrated Intelligent Flight Deck (IIFD) project will pursue flight deck related technologies that ensure crew workload and situation awareness are both safely optimized and adapted to the future operational environment as envisioned by the NextGen. A key component of this research will be investigating methods to automatically monitor, measure, and assess the state of crew awareness. Project results should enable system designers to eliminate the safety risk of unintended consequences when introducing new and advanced systems into an operational environment.

As stated previously, IIFD develops flight deck technologies that mitigate operator-, automation-, and environment-induced hazards for future operational concepts. The scope includes: (a) development of crew/vehicle interface technologies that reduce the risk of pilot error; (b) development of monitoring technologies to enable detection of unsafe behaviors; (c) development of fail-safe methods for changing the operator/automation roles in the presence of detected disability states; and (d) development of a comprehensive surveillance system design that enables robust detection of external hazards with sufficient time-to-alarm for safe maneuvering to avoid the hazards.

For our purposes, a flight deck and a flight deck system are defined as follows:

- Flight Deck: A volume of space designed to accommodate at least one human operator and the interfaces between the operator and the remainder of the flight deck system.

- Flight Deck System: A system that includes (1) the entity(s) who have the authority and responsibility for directing the flight of an aircraft, (2) all subsystems that directly interface to these entity(s), and (3) the interfaces between them.

Vigilant observation of the surrounding airspace for external hazard detection is essential for operational capability and safety. There are five classes of external hazards: (1) meteorological (e.g. icing conditions, convective weather, wind gusts, turbulence), (2) environmental (e.g. volcanic ash), (3) geospatial (e.g. terrain, man-made obstacles, foreign object debris), (4) traffic, and (5) airspace constraints/restrictions. The severity of hazards associated with any of these depends on many factors such as relative proximity and closure rate.

The Forward-Looking Interferometer (FLI) is an instrument concept for efficiently obtaining the measurements required to alert flight crews to potential weather hazards to safe flight. The FLI concept is based on passive radiometric sensing with an aircraft-mounted Michelson Fourier transform spectrometer capable of measuring atmospheric conditions ahead of the aircraft for the purpose of detecting hazards to the aircraft or determining other information related to flight deck requirements. This instrument concept was initially evaluated for detecting Clear Air Turbulence (CAT), and the project was subsequently expanded to include the investigation of the feasibility of detecting other hazards such as volcanic ash, wake vortices, dry wind shear, reduced visibility, and icing conditions along the flight track of the aircraft. It is potentially applicable to external hazards in classes 1-4 above. FLI sensor data may be used alone or in combination with other sensor data such as airborne weather radar or lidar. The data it provides should complement other airborne forward-looking hazard detection, such as radar detection of turbulence or wind shear, by providing data in conditions where other sensors have insufficient signal available to allow detection. It is also anticipated to be capable of providing additional data useful in discrimination and hazard estimation. Additional possible applications, not addressed in current investigations, may include detection of runway contamination; observations of temperature and water vapor for use in weather models; and detection of pollution or other aerosols. The technology could also be applied for downward-looking atmospheric profiling of water vapor, temperature, turbulence or other applications.

The study seeks to predict instrument performance for hazard detection and measurement via models and analyses, to validate the models with experiments and to identify technical challenges that must be addressed for development of a practical sensor based on the technology. Subsequent to a successful feasibility study [1], NASA expects to attack the technical barriers to instrument development, develop and improve the models and performance predictions, and to identify the next steps to be taken in the development of a FLI-based airborne sensor. Such future efforts should include ground and flight-testing of prototype FLI hardware to collect data for sensor and phenomenological characterization and validation.

This feasibility study began with a Workshop on the Airborne Radiometric Detection of Aviation Hazards. The goals of the workshop were to review the current status of research in this technical area, to assess the resources that are available for further work, and to familiarize interested participants with the research program. The workshop included participants from government, industry, and academia. The results of the Workshop are presented in Appendix A of this report.

This report includes sensitivity studies and the characterization of various hazards occurring at cruise altitudes or during the takeoff and landing of aircraft. Sensitivity studies were conducted on CAT, volcanic ash, and low slant range visibility. Characterization to determine if sensitivity studies were warranted included wake vortices, dry wind shear, and icing.

Based on the results of the studies discussed in this report, a table of FLI radiance measurement requirements for a research instrument is presented. In addition, future research needs have been determined to identify the next steps to be taken in the development of an FLI-based airborne hazard sensor. Such future efforts should include further sensitivity studies, ground and flight-testing of prototype FLI hardware to collect data for sensor and phenomenological characterization and validation, and development of a simulation environment.

Additional information on previous wind shear studies is presented in Appendix B and candidate research instruments are described in Appendix C. A report by Larry Cornman of the National Center for Atmospheric Sciences (NCAR) is included as Appendix D. The NCAR report is divided into two parts: Part A discusses the work performed investigating methodologies for measuring turbulence from an airborne IR interferometer; Part B provides an overview of the data sets that were delivered to Hampton University in support of their simulation activities.

A feasibility study of using an FLI to detect a hazardous runway surface conditions (reduction of runway friction from ice or snow) is the subject of Appendix E, a report by William Smith.

3 Background

The long history of investigations into airborne IR radiometric detection of aviation hazards has provided examples of apparent detections of CAT and wind shear, as well as a data set that was interpreted as images of wake vortices. In addition, ground-based radiometric detection of volcanic ash clouds has been demonstrated [2], [3], [4]. However, all of the early work was done with simple instruments that had low spectral, spatial, and radiometric resolution, and most of them employed a single line of site. The detections were generally not supported by truth data, and the atmospheric conditions that the radiometers were responding to were characterized poorly, if at all. Here we define "truth data" as independent measurements of the hazard, e.g. aircraft acceleromteter measurements of turbulence or F-factor measurements for wind shear. Because the atmospheric state was not known, the performance of the radiometers as hazard sensors could not be checked with numerical

simulations. These problems led Gimmestad et al. [3] to recommend that flight tests should be conducted with a hyperspectral IR imaging system; that the flights should include truth data; and that the measurement effort should be supported by a parallel simulation effort. The study reported here is a related effort aimed specifically at assessing the feasibility of using an FLI for aviation hazard detection.

4 Sensitivity Studies

Sensitivity studies were performed on CAT, volcanic ash, and low slant range visibility. CAT sensitivity studies included the development of a high spectral resolution spherical shell radiative transfer model, based on Line-By-Line Radiative Transfer Model (LBLRTM) [5], [6] molecular optical depths. FLI simulations were conducted using three-dimensional temperature and water vapor fields associated with CAT provided by the National Center for Atmospheric Research (NCAR) in Boulder, CO. Volcanic ash cloud detection sensitivity studies have been conducted using window region spectral radiance emission observations. Two different algorithms for determining the distance to an aerosol cloud were implemented. The algorithms include the "CO_2 Slicing" technique and the "Window Channel" technique. Lastly, sensitivity studies for enhanced slant range visibility were conducted using "Empirical Orthogonal Functions (EOF) Regression" or "Principle Components (PC) Regression" to correct the effect of absorbing atmospheric constituents such as fog and aerosols.

4.1 Clear Air Turbulence (CAT)

Radiometric techniques for turbulence detection rely on atmospheric temperature and water vapor structures that depart from the background atmosphere. The radiometric techniques are indirect in the sense that they do not measure turbulent motion. Rather, they measure the temperature structure and water vapor structure of the atmosphere ahead of the aircraft and attempt to relate it to the likelihood that turbulence will be experienced.

Researchers have been studying passive IR detection of turbulence for decades. For example, in the 1970's, Peter Kuhn developed an IR radiometer that was flown and tested on three NASA aircraft in the 1979 Clear Air Turbulence Flight Test Program [7]. Kuhn's passive IR system detected CAT by detecting water vapor variability ahead of the aircraft. (In non-CAT conditions, the water vapor content is fairly constant.) Kuhn claimed that the detector had a false-alarm rate of less than 8% in clear air at altitudes above 4.4 km with a range of 60 km. However, the system was not tested with clouds in the vicinity [7].

In the study reported here, FLI simulations were conducted using three-dimensional temperature and water vapor fields associated with CAT. Techniques for determining the distance and warning time to an aircraft encounter with CAT were defined. The spectral resolution, range, and instrument noise requirements were defined for an FLI to be used to detect CAT and to determine its distance from the aircraft (i.e., warning time) by both the temperature and water vapor radiance signal techniques.

A high spectral resolution spherical shell radiative transfer model, based on Line by Line Radiative Transfer Model (LBLRTM) molecular optical depths, was developed to study phenomena at some distance from the aircraft. A pictorial display of the path seen by an FLI aboard an aircraft is shown in figure 1.

The model takes the analytical form

$$R(\nu, A, h_o) = \int_0^{TOA} B[\nu, T(s)] * [-\frac{\partial \tau(\nu, s, A)}{\partial s}] ds \tag{1}$$

where R is radiance, TOA is top of atmosphere, ν is wavenumber, A is the atmospheric state consisting of pressure p, temperature T, absorbing constituents (i.e., H_2O, CO_2, O_3,

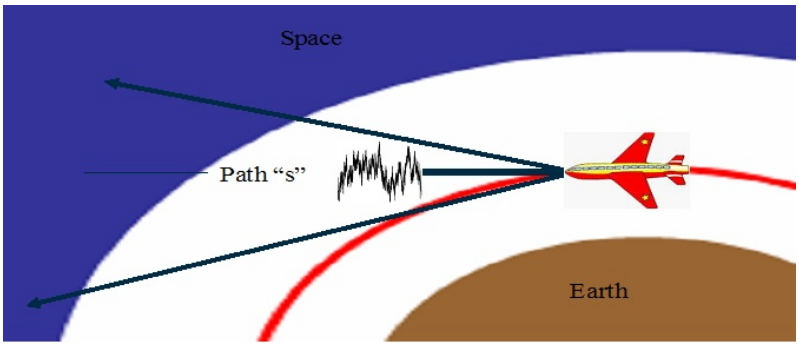

Figure 1. Path viewed by a forward-looking optical instrument aboard an aircraft.

N_2O, CO, CH_4, O_2, NO, SO_2, NO_2, NH_3, HNO_3, clouds, and aerosols), h_o is the height of the aircraft, and B is the Planck function.

The transmittance of the atmosphere betweeen the aircraft and any position along the viewed path s is

$$\tau(\nu, s, A) = \int_0^s e^{-\sigma(\nu, s', A)} ds' \tag{2}$$

where σ is the optical depth. The coordinate along the viewed path, s, is

$$s(h) = \sqrt{(r_e + h)^2 - (r_e + h_o)^2} \tag{3}$$

where h is height and r_e is the radius of the Earth.

Figure 2 shows the results of applying this model to the US Standard Atmosphere to simulate what an FLI would see in clear air when flying on an aircraft at three different altitudes. The spectral radiance is plotted versus wavenumber which would be observed by an FLI for aircraft altitudes of 1.5, 4.5, and 9.5 km. A Norton-Beer Weak Apodization was applied to interferograms simulated to a maximum optical path difference of 1.0 cm (i.e., an unapodized spectral resolution of 0.5 cm^{-1}).

The spectrum corresponds to a near-isothermal spectrum (i.e., a Planck function) for the relatively opaque 15μm CO_2 band, 650 - 750 cm^{-1}. A near-Planck radiance distribution is also observed for the strong water vapor absorption region, beyond a lower wave number limit ranging from 1250 - 1500 cm^{-1}, dependent upon instrument altitude. The strong emission by ozone within the 1000 - 1100 cm^{-1} region can also be seen in figure 2, with the relative amplitude of this emission band increasing with altitude as a result of the increase in ozone concentration and the rapid decrease of the water vapor concentration with altitude. The strong absorption/emission by methane and nitrous oxide near 1305 cm^{-1} can also be seen from the fact that the spectral radiance distribution approaches a Planck radiance spectrum as the altitude of the sensor decreases.

Figures 3, 4, and 5 show plots of the relative contribution from the atmosphere (assuming US Standard Atmospheric conditions) as a function of distance from the aircraft. Each plot indicates the total radiance at three different altitudes, 1.5, 4.5, and 9.5 km. Contributions greater than 100% are a consequence of ringing in the spectrum that remains after the weak apodization process that was performed. The higher the aircraft, the greater the contribution from spherical shells at greater distances from the aircraft. For the sensing of turbulence from the 15 μm CO_2 band, most of the signal ($\geq$ 60%) is confined to the first

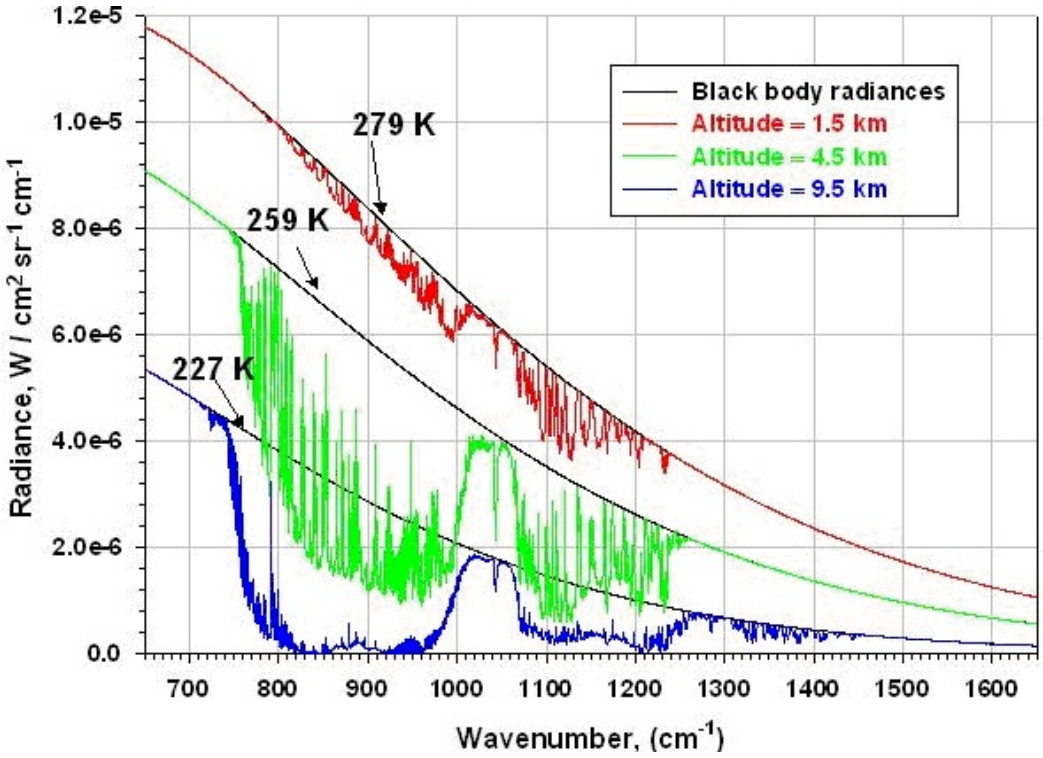

Figure 2. The spectral radiance observed by an FLI.

5 km shell ahead of the aircraft for wave numbers smaller than 722 cm^{-1}, decreasing with increasing wave number. In the "window" region of the spectrum, 800 - 1200 cm^{-1}, the FLI observes contributions from the atmosphere at distances greater than 80 km when flying at high altitude (e.g., 9.5 km).

This long range detection capability makes the technique useful for the detection of hazardous aerosol (e.g., volcanic ash clouds) contributions, providing avoidance warning times in excess of 5 minutes for a fast flying commercial jet aircraft. At middle and low atmospheric altitudes (e.g., 4.5 km and 1.5 km) the visibility of clouds and aerosol layers with distance decreases, being greatest for a narrow spectral region near 1000 cm^{-1} and the 1100 - 1150 cm^{-1} region of the spectrum. In addition, high spectral resolution is needed to optimize the FLI instrument sensitivity to contributions of radiance far from the aircraft, which results from being able to sense the radiation between the water vapor absorption lines within the "window" region of the spectrum.

4.2 Temperature Turbulence Measurement Concept

Detecting temperature fluctuations associated with CAT can be accomplished using either a fully- or partially-scanned infrared interferometer. In the partial scan approach, by observing the CO_2 resonance region of the interferogram produced by the near uniform spacing of CO_2 lines in the 13 - 15 μm region, discontinuities of temperature will produce a signal within this narrow CO_2 resonance region. The signal's amplitude is dependent upon the amplitude of the non-uniformity of atmospheric temperature. The distance from the aircraft at which these discontinuities exist should be indicated by the spectral wavelength sub-region of the 13 - 15 μm band where one begins to see the signal. For example, the stronger the signal gets near the more opaque center of the CO_2 absorption band, the closer to the aircraft the

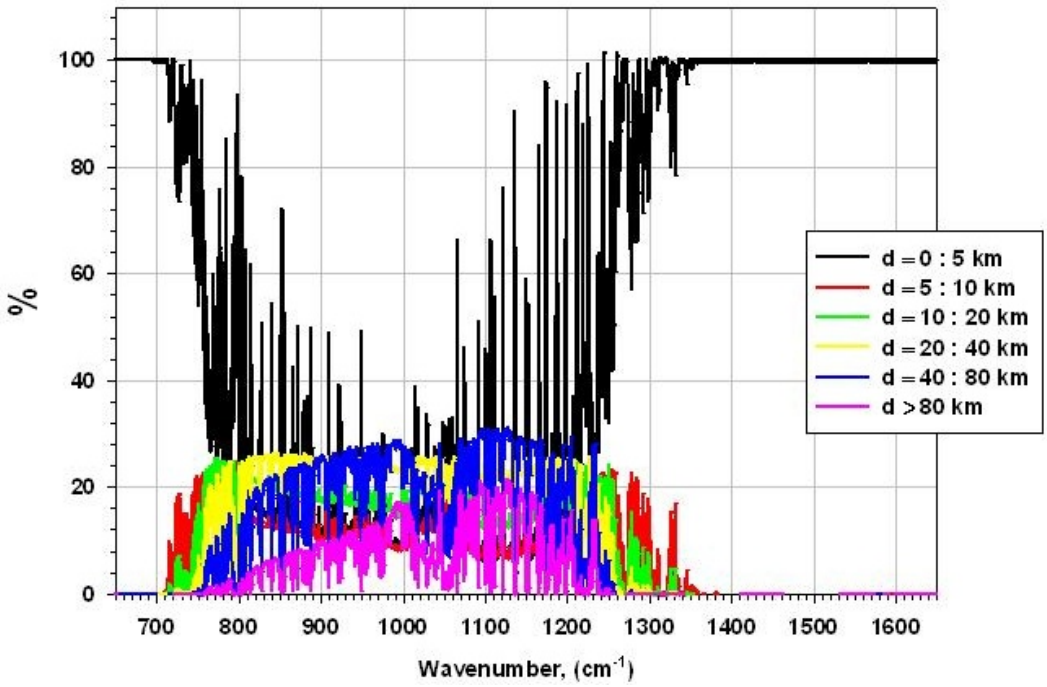

Figure 3. Contribution to the total radiance at 1.5 km.

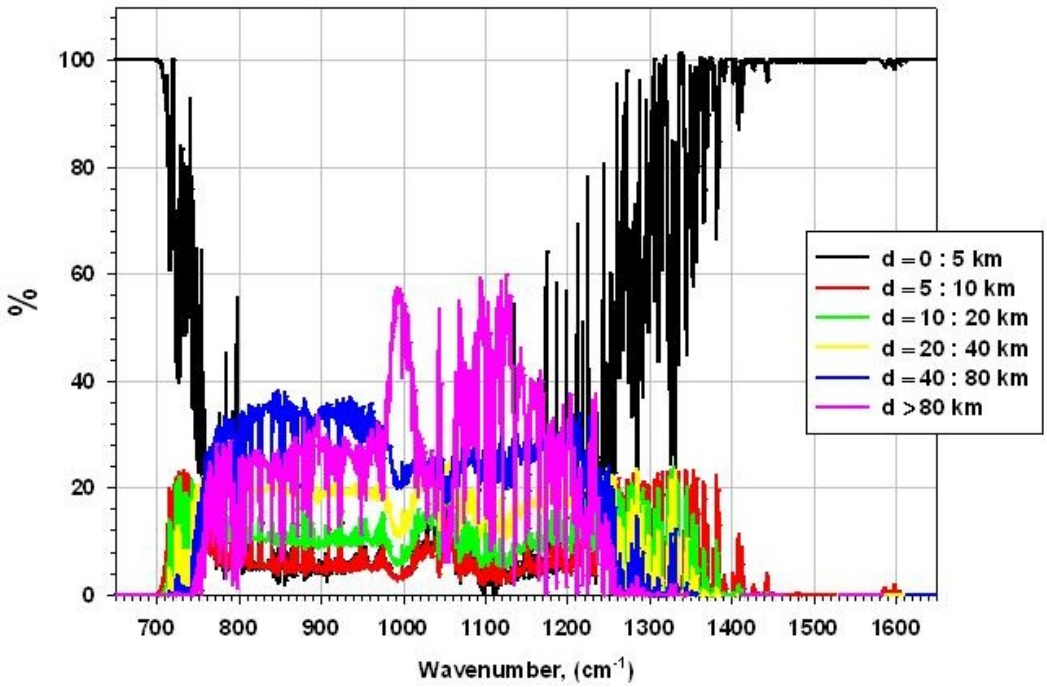

Figure 4. Contribution to the total radiance at 4.5 km.

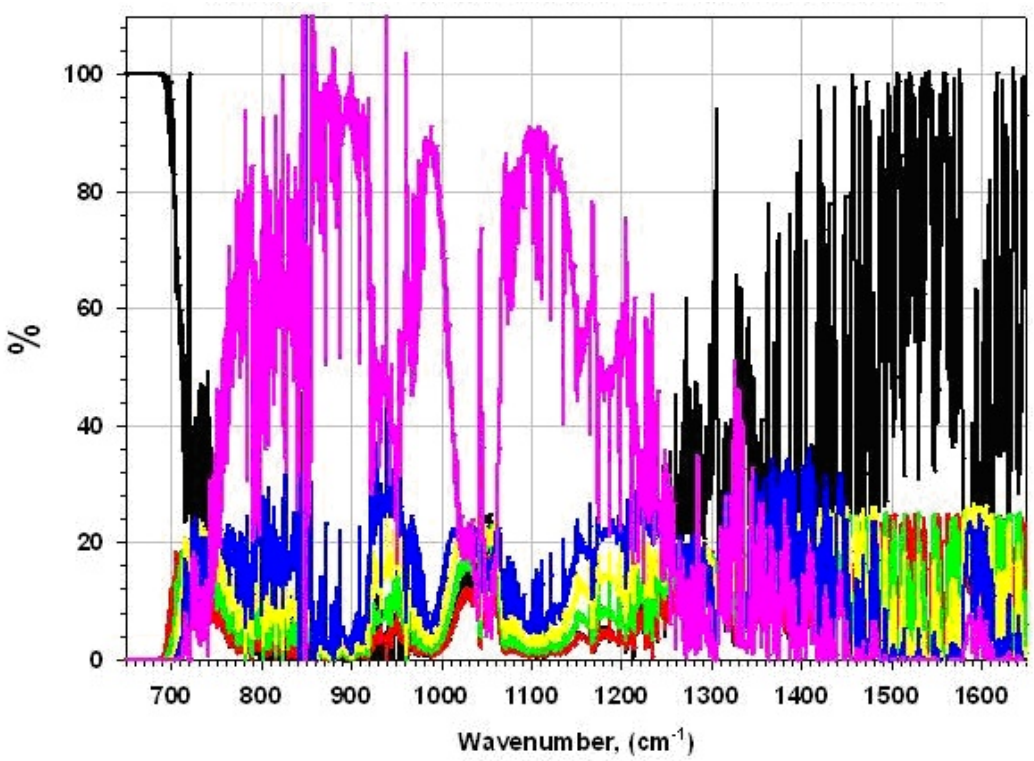

Figure 5. Contribution to the total radiance at 9.5 km.

temperature fluctuation must be occurring. The radiometric signal will be small, but FTS systems are very sensitive to very small spectral features of the radiation being detected - in this case, the relative amplitude of the CO_2 lines, which is zero for a completely uniform temperature scene.

The spherical shell radiative transfer model was applied to a one-dimensional case of turbulence-related temperature variations observed from a commercial jet aircraft, which encountered a narrow zone of severe turbulence. The top plot of figure 6 shows the radiance emission lines associated with the temperature perturbations from a severe velocity turbulence encounter by a commercial passenger jet aircraft near Houston, TX, on August 6, 2003 (shown in the time series bottom plot of figure 6). The relatively uniform spacing of the CO_2 emission lines is evident in the spectrum of turbulent radiance perturbation from a horizontally uniform temperature condition.

An analysis of the CO_2 resonance in the interferogram produced by a turbulent temperature fluctuation during the same turbulence encounter by the commercial aircraft at an altitude of 9.5 km is shown in figure 7. In this figure, the top plot is brightness temperature difference versus wavenumber while the bottom plot is the interferogram ratio $(I - I_0)/I_0$. The turbulence signal can be seen in the raw interferogram measurement from the amplitude of the CO_2 resonance region produced by the relative uniform spacing of the CO_2 emission spectral radiance variations. Thus, the temperature fluctuation signal produced by wind turbulence can be detected in either the raw interferogram or the derived spectrum of radiance observed with an FLI instrument.

Three case studies have been performed to determine both the interferogram and spectral radiance signal resulting from temperature fluctuations associated with clear air turbulence. One case is the actual temperature measurement fluctuation observed from a commercial

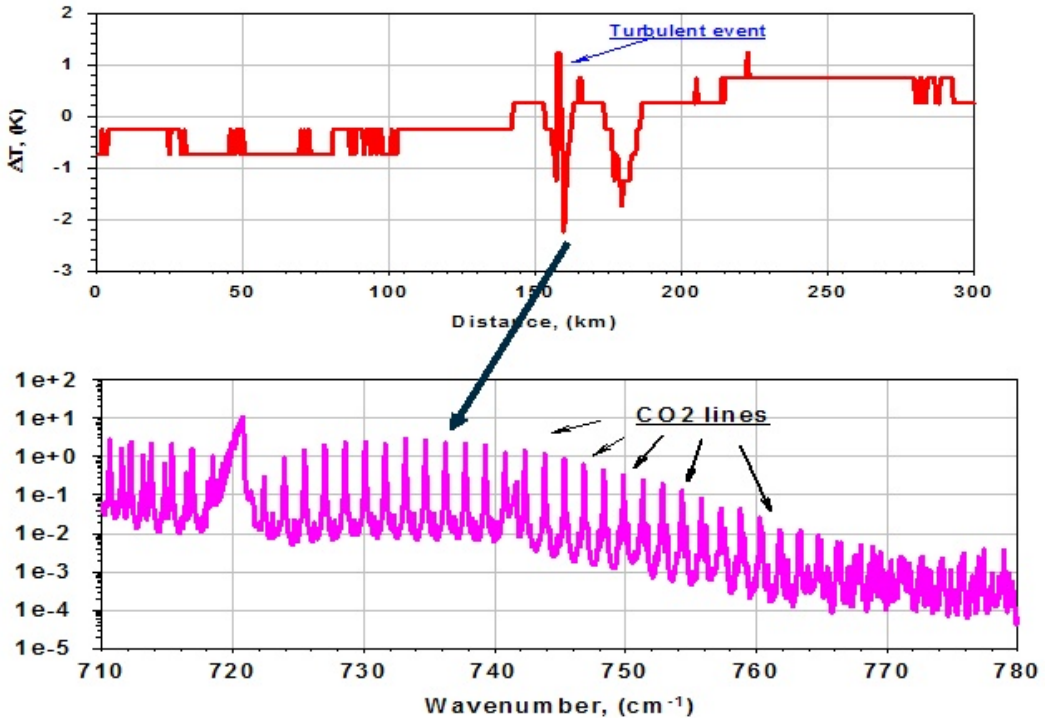

Figure 6. The radiance emission lines.

jet aircraft during an encounter with severe clear air turbulence, as described above, with the other two resulting from von Kármán simulations for moderate to weak wind turbulence conditions. All of the simulations were conducted for the aircraft within a 40, 20, 10, 5, and 0 km distance from the relatively narrow turbulent region. Figures 8, 9, and 10 show the three cases where the assumed aircraft altitude is 9.5 km. The distance to the turbulent region is associated with the wavenumber where significant spectral structure begins, moving towards larger wavenumbers with increasing distance from the turbulent regime.

As shown in figures 11, 12, and 13, there is a relatively large spectral signal when the aircraft is close to the turbulence but this signal decreases rapidly as the aircraft becomes more distant from the turbulent region. Thus, the ability of the spectral, or partial interferogram amplitude, to provide significant warning time before severe turbulence is encountered depends on the interferogram signal-to-noise ratio that can be achieved with the FLI.

Finally, figure 14 shows the altitude dependence on the spectral radiance and interferogram produced from turbulent temperature fluctuations 20 km ahead of the aircraft simulated for von Kármán case #2. In this situation, the typical commerical aircraft would have about 80 seconds of warning time. The signal maintains a nearly constant strength when the aircraft descends to 4.5 km but then decreases with a further descent to 1.5 km. The enhanced response of the FLI to turbulent temperature fluctuations at high altitudes is advantageous, since most severe clear air turbulence occurs at the higher altitudes.

4.3 Water Vapor Turbulence Measurement Concept

It may be easier to detect clear air turbulence at a greater distance using water vapor radiance measurements rather than CO_2 temperature measurements because the atmosphere may be relatively transparent due to low water vapor concentrations between the aircraft

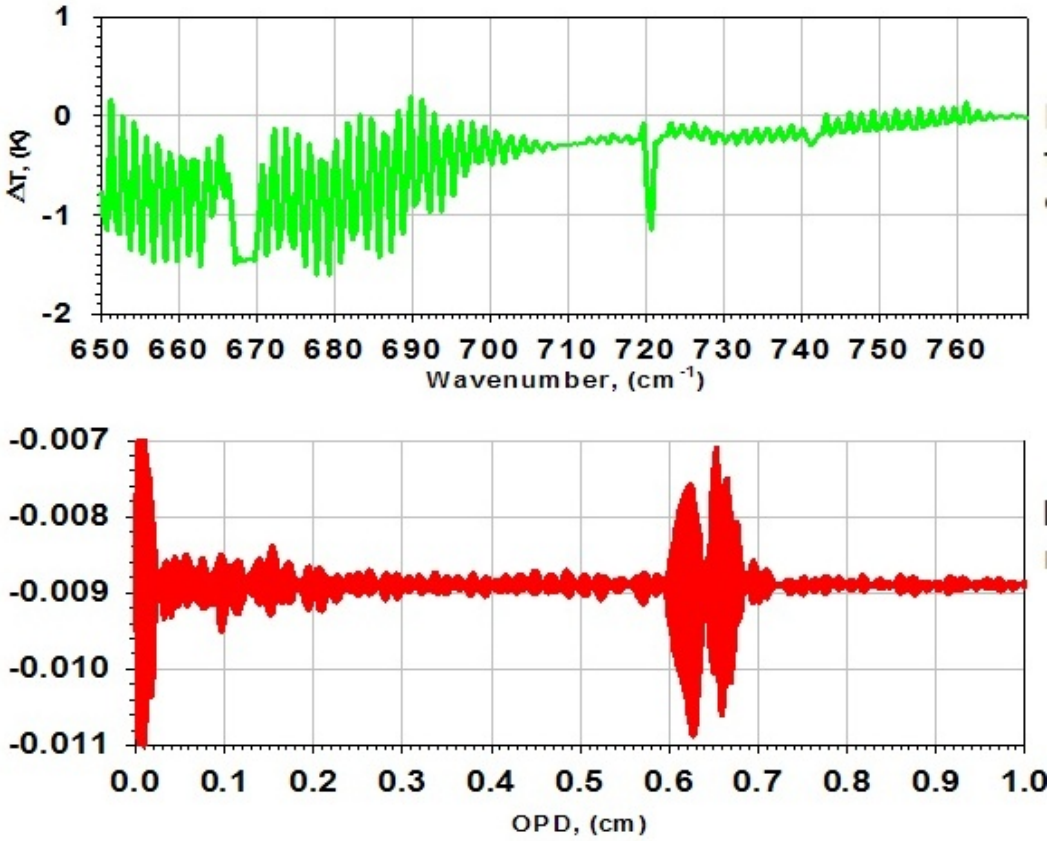

Figure 7. CO_2 resonance in the interferogram.

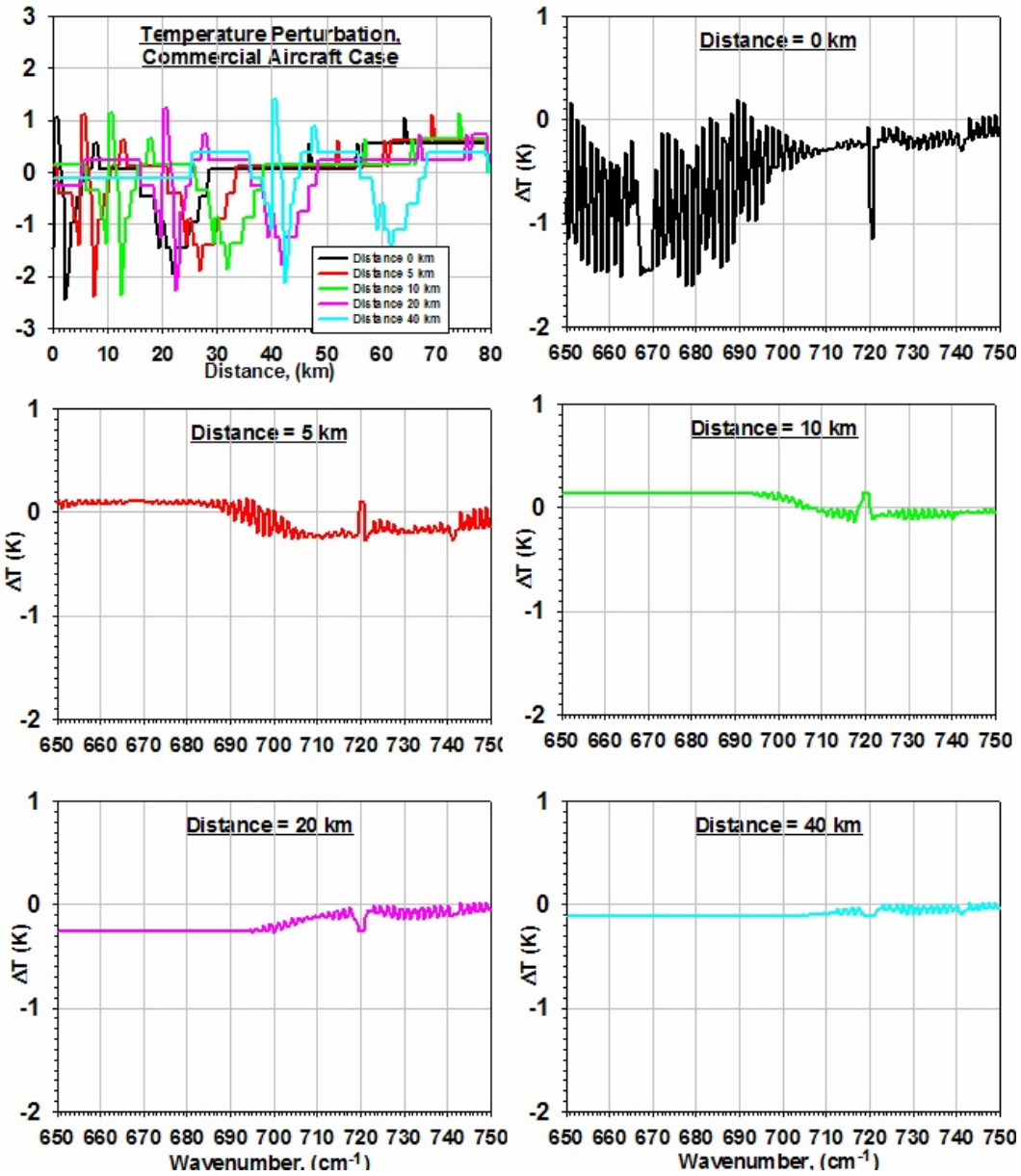

Figure 8. Temperature fluctuation and brightness temperature signal.

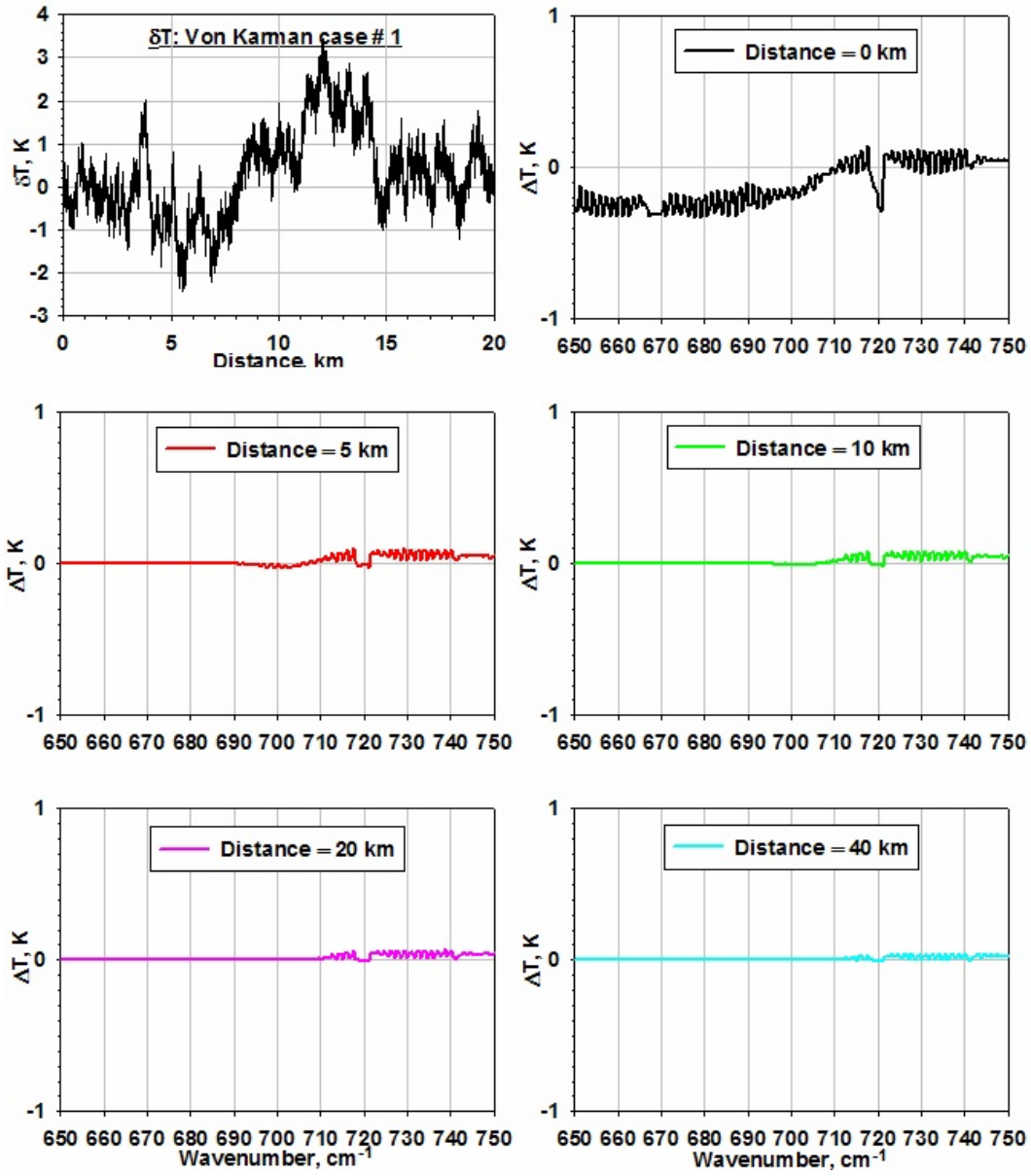

Figure 9. von Kármán case #1 simulation.

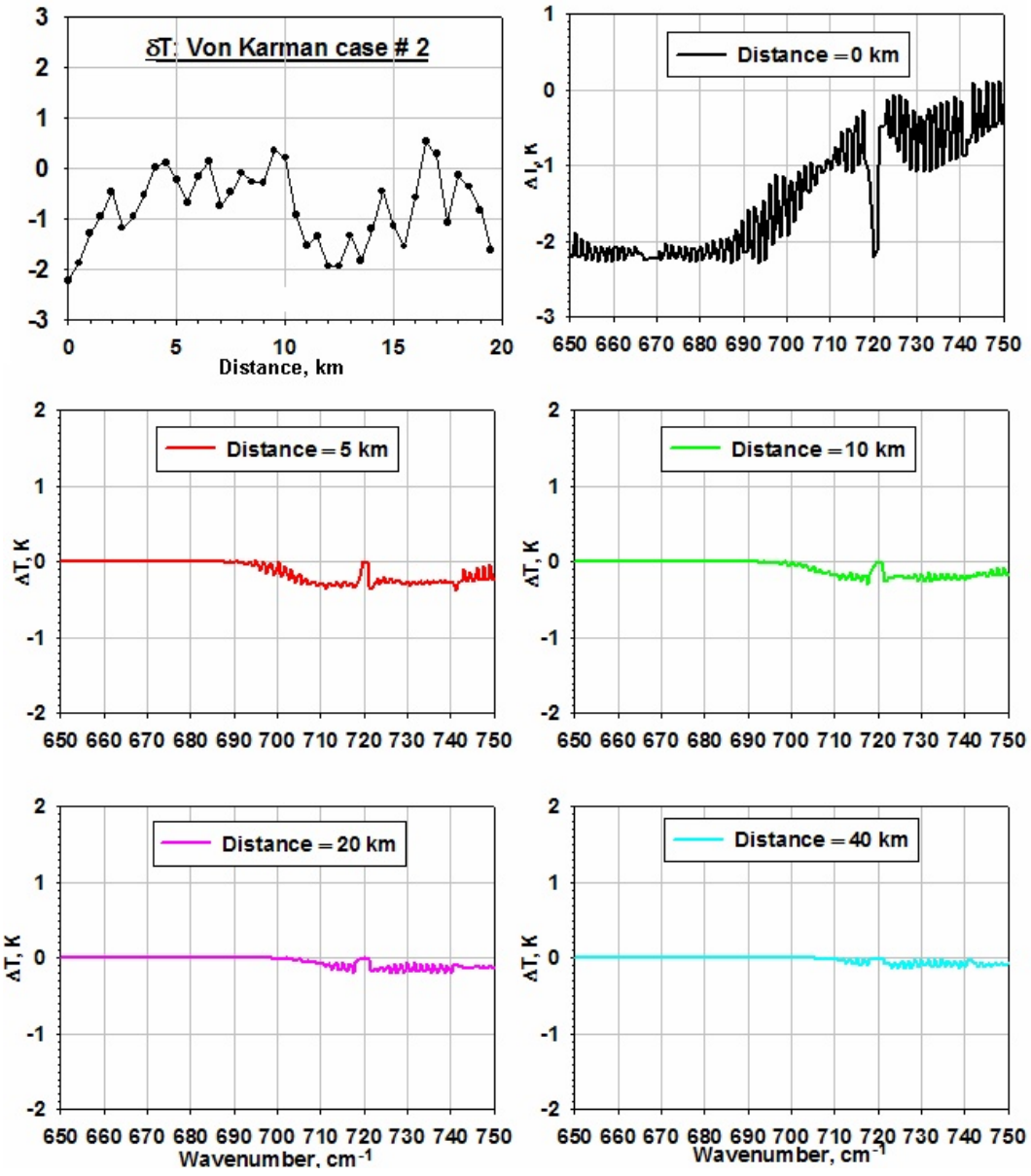

Figure 10. von K*árm*án case #2 simulation.

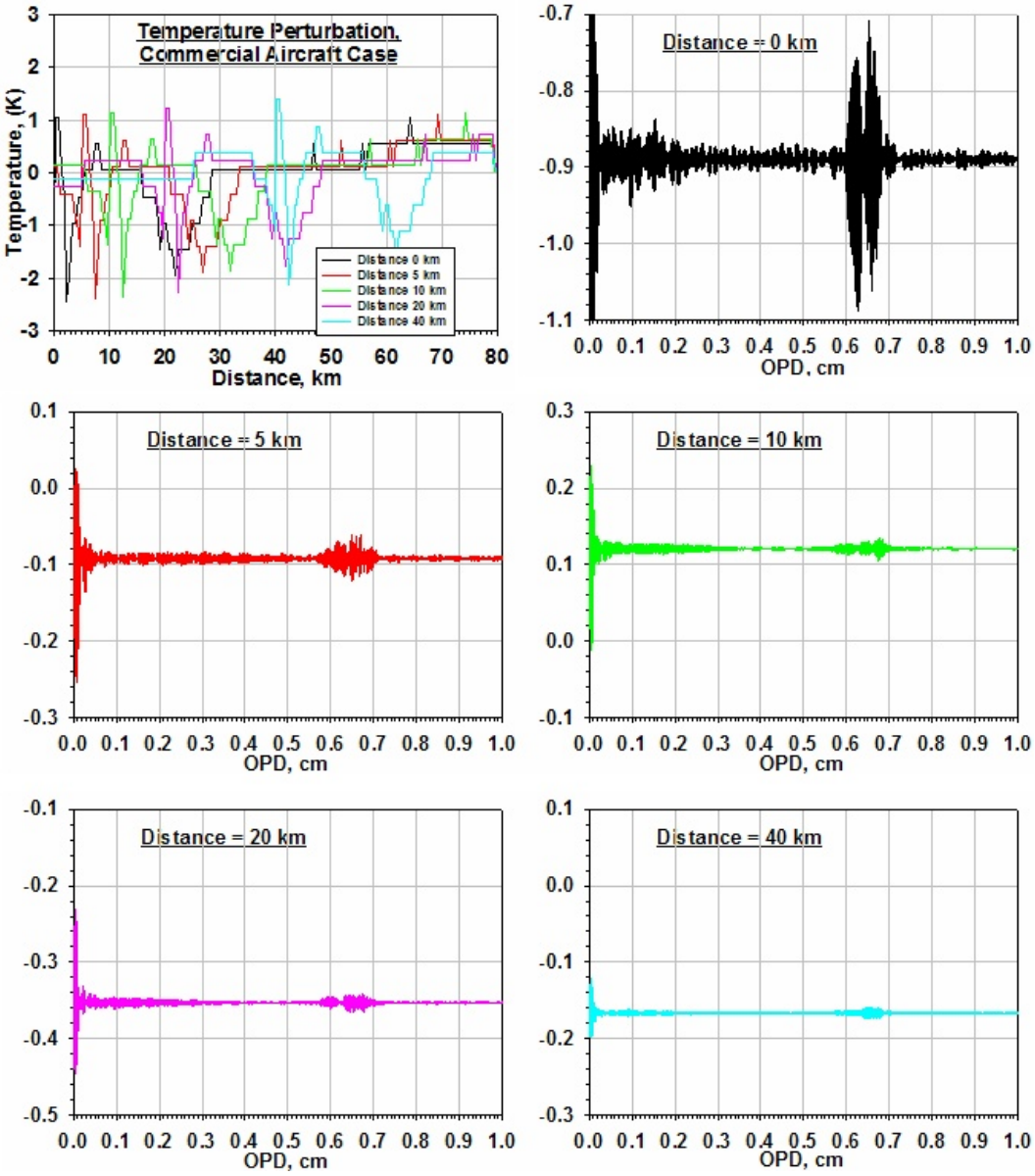

Figure 11. Commercial aircraft simulation case.

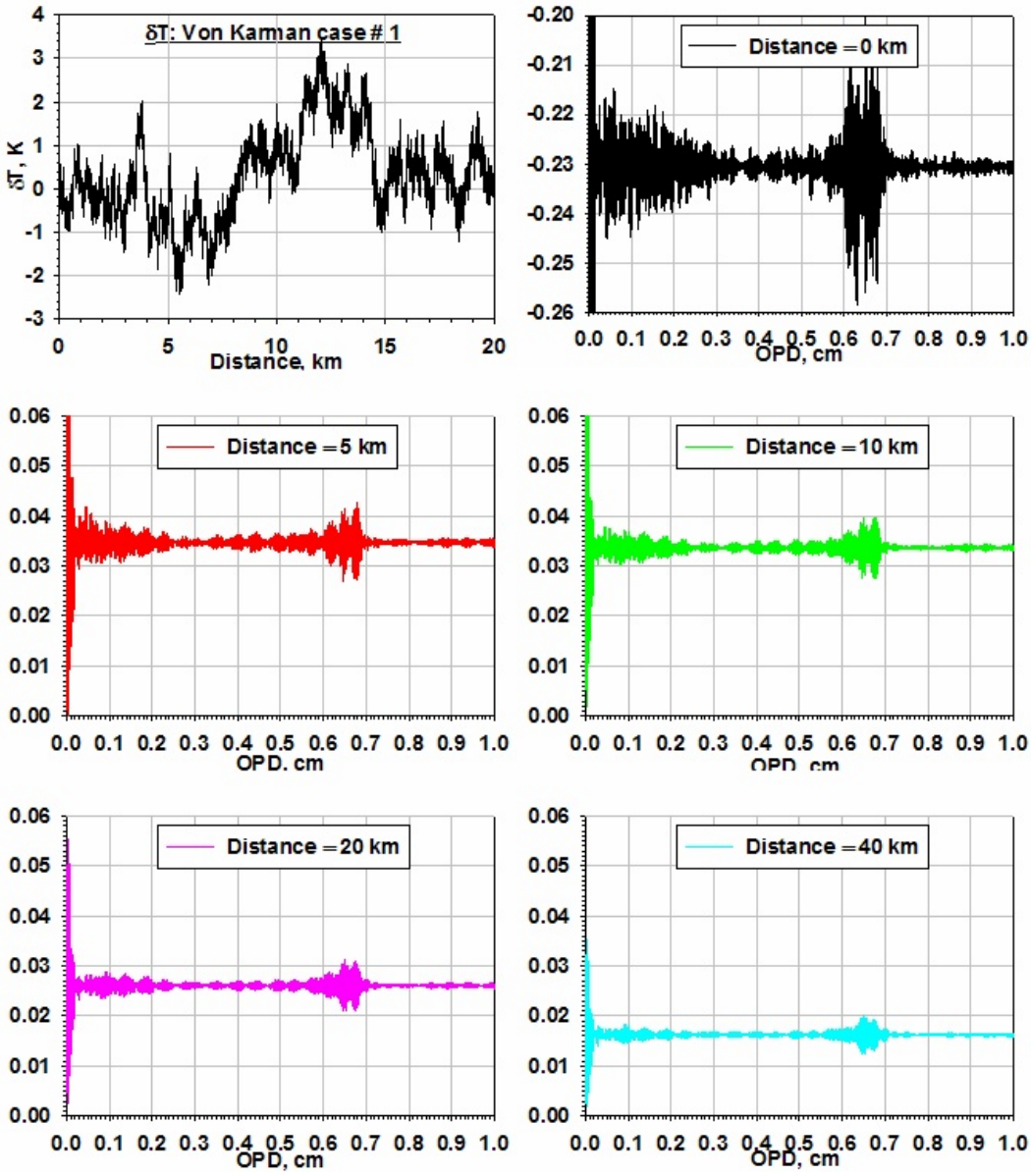

Figure 12. von Kármán case #1 severe turbulence regime.

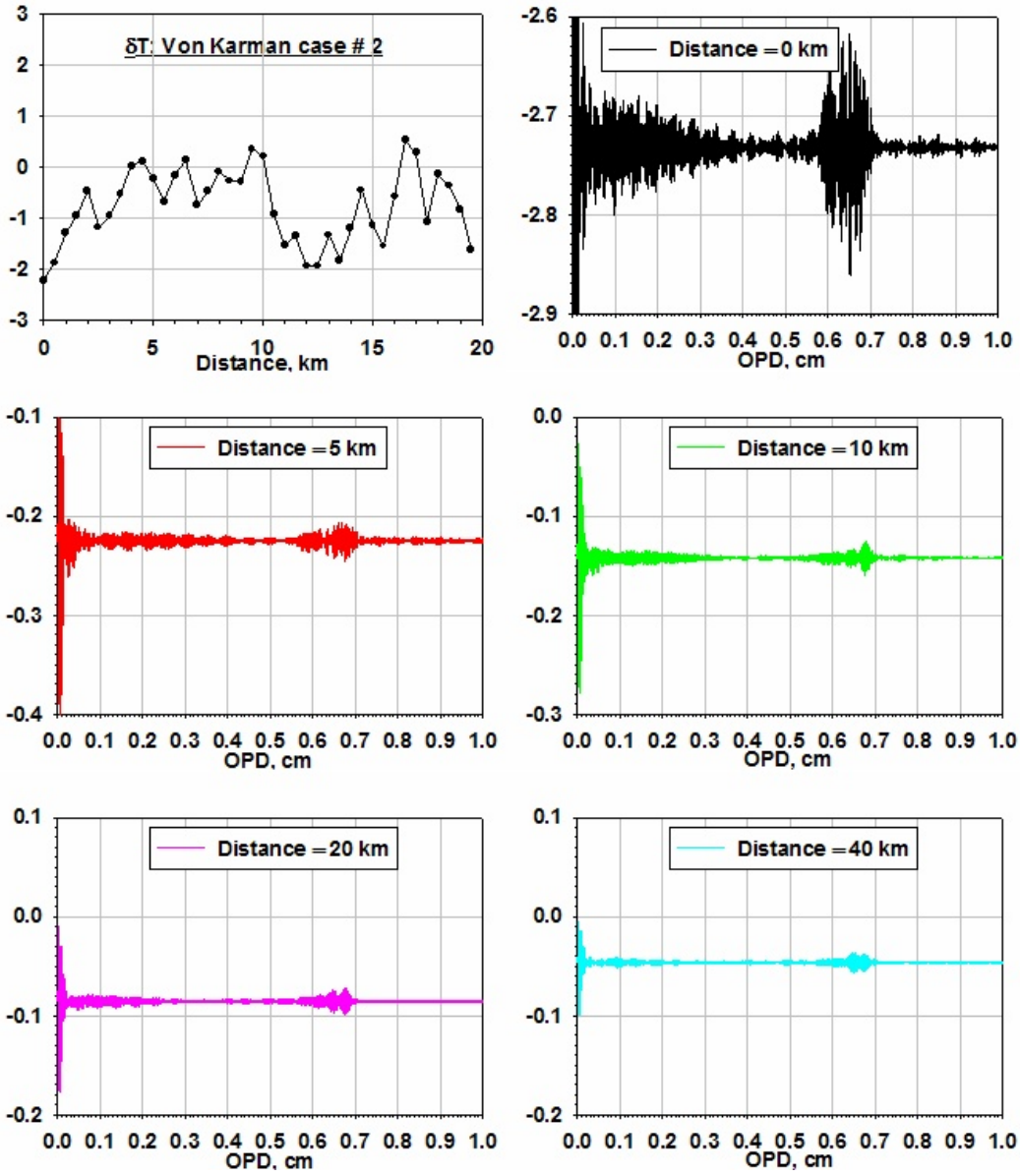

Figure 13. von Kármán case #2 severe turbulence regime.

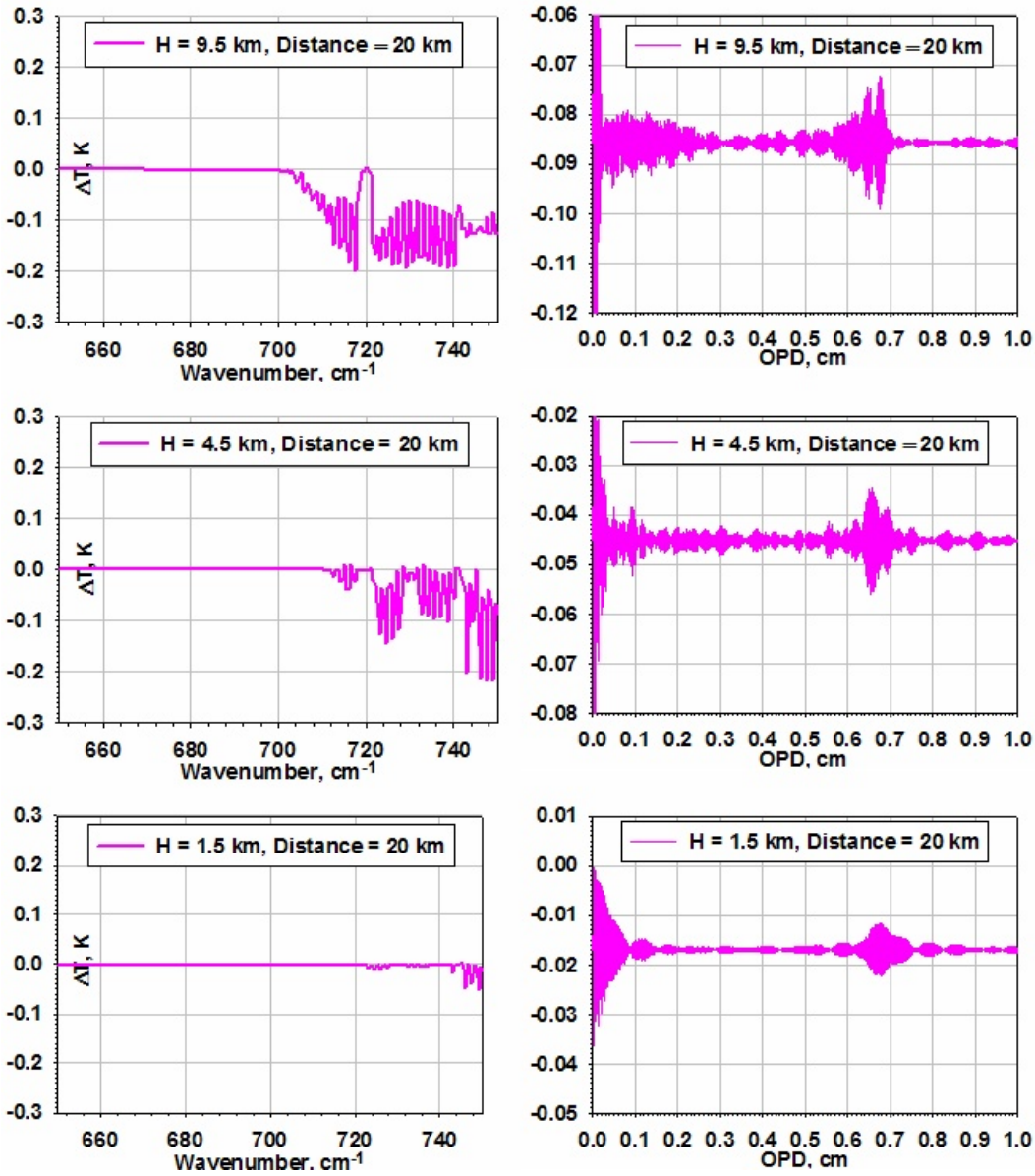

Figure 14. Variation of spectral radiance and interferogram signal.

and the turbulent region. In the turbulent region, water vapor molecules are injected into the otherwise relatively dry upper troposphere, creating a water vapor anomaly that can be detected by the FLI in the water-vapor radiant emission spectral regions.

In figure 15, the flight track of the NOAA G-IV Research Aircraft on 6 December 2003 is shown on the left side. This picture shows the location where severe turbulence was encountered by the NOAA G-IV research aircraft flying in clear air over convection, over the Atlantic ocean off the northeast coast of the US. The image on the right side is false color temperature and moisture data from a satellite depicting the conditions during the flight. The bright red and orange indicate severe convection.

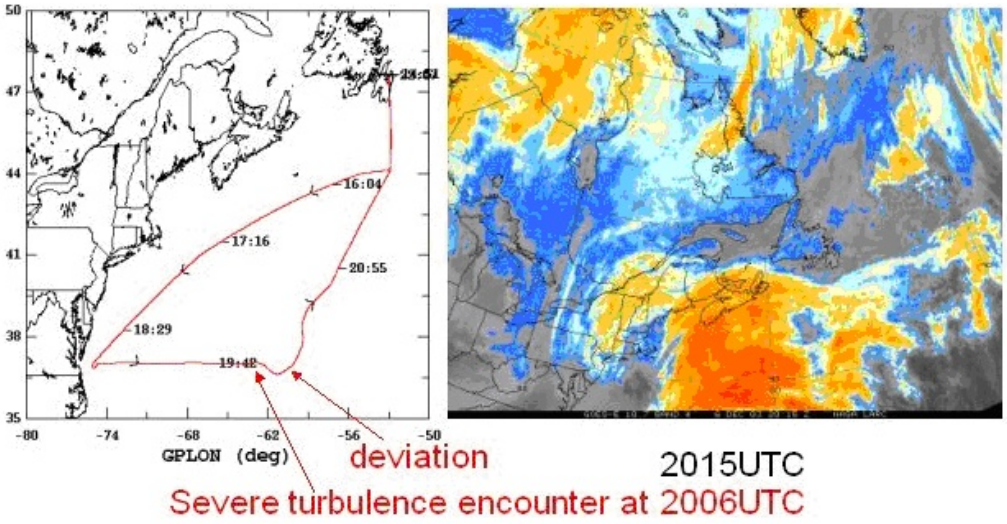

Figure 15. NOAA G-IV aircraft flight track on 6 December 2003.

Figure 16 is a series of plots of flight data from the NOAA G-IV flight on 6 December 2003. Each plot is a time series of different parameters measured from the research aircraft. The first three plots are the u (east-west), v (north-south), and w (vertical) components of wind, followed by temperature, true air speed, and altitude, and finally aircraft heading and relative humidity. The plots indicate that there is a noticeable fluctuation in relative humidity at the point of the severe turbulence encounter. As a result, there should also be a noticeable signal in FLI radiance spectra due to this severe turbulence signature in the horizontal water vapor distribution.

Figure 17 shows the spectra that would be observed for the G-IV encounter with an FLI observing the radiance spectrum from 680 - 1600 cm^{-1}. The water vapor signal of turbulence in the 1300 - 1600 cm^{-1} region is very strong ($\pm$ 2 K) as early as $\Delta t = 0$, which is about 150 seconds before the severe turbulence encounter. Moreover, this signal seems to persist over a relatively large spectral region. This persistence indicates that the spectral resolution of the FLI will not need to be as high for detecting the water vapor signal associated with severe turbulence as that required to detect the temperature signal of severe turbulence. The spectral resolution required for sensing the water vapor signal of turbulence is ≤ 2.5 cm^{-1}, whereas the spectral resolution required for sensing the temperature signal is ≤ 0.625 cm^{-1}.

4.4 Volcanic Ash

Approximately 60 volcanoes worldwide are active during a typical year, and in the North Pacific Region of the United States alone, volcanic ash is present an average of 4 days

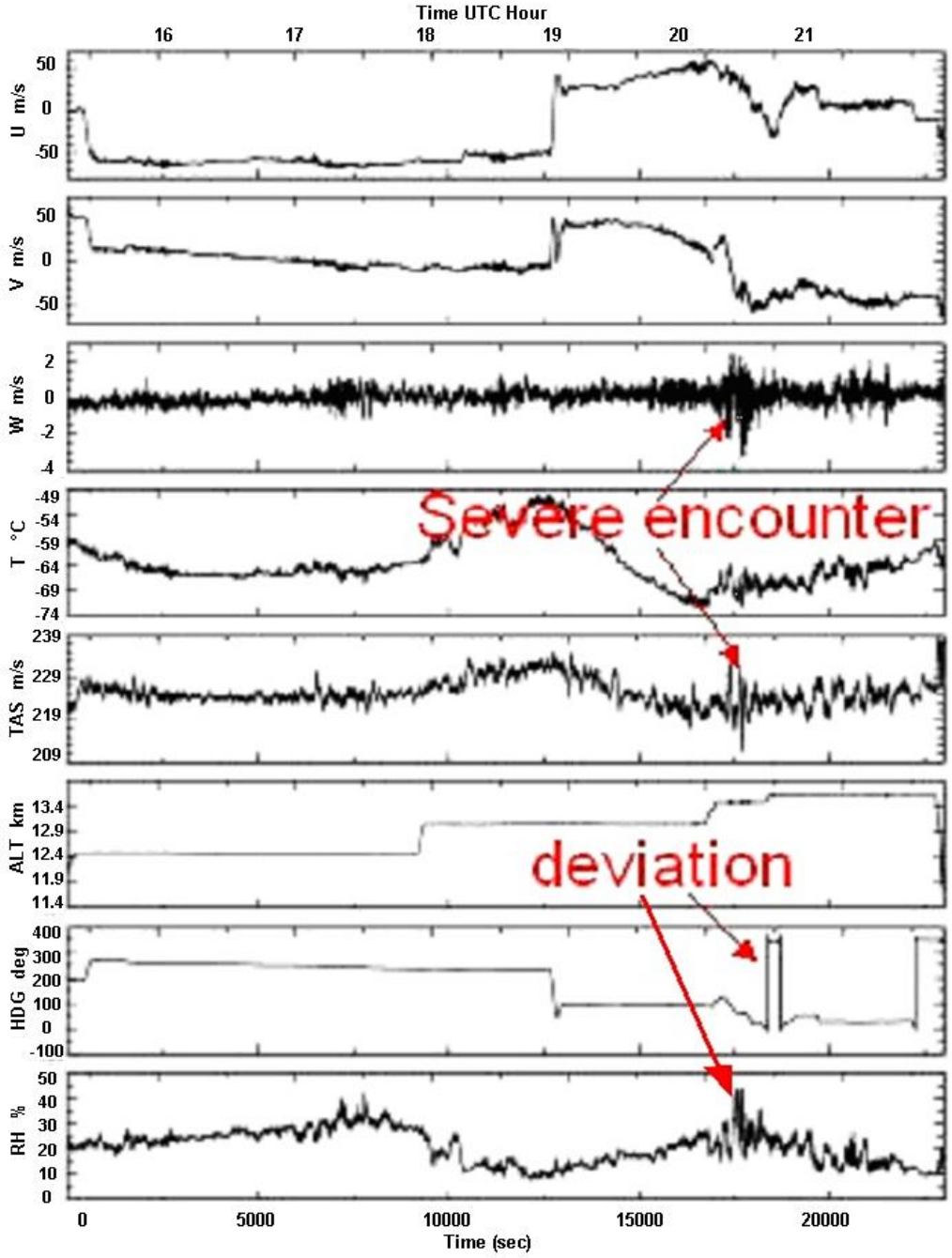

Figure 16. Time series data from the NOAA G-IV severe turbulence encounter.

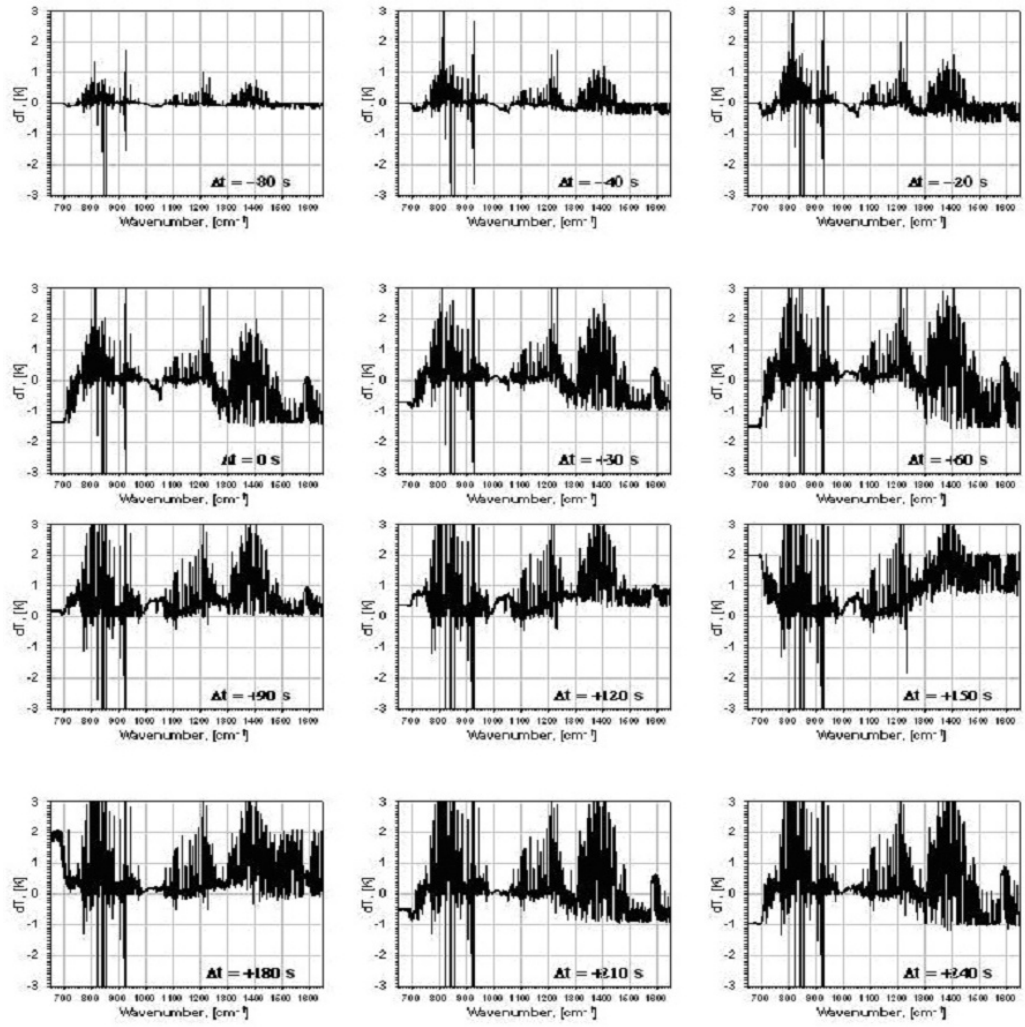

Figure 17. Radiance spectra with turbulence event occurred at about Δ t = +150.

a year where most jet aircraft fly [8]. Volcanic ash can cause jet turbine engine failure. During the time period from 1973 until 2000, about 100 reported incidents occurred where aircraft encountered volcanic ash [2]. The Geophysical Institute at the University of Alaska Fairbanks recently completed an extensive study of volcanic activity in the North Pacific. In this study, 100 years of volcanic eruption data was used to run thousands of PUFF model simulations of eruptions of volcanoes in the area [9].[1] The result was a reliable set of average data describing trends in ash migration from Northern Pacific volcanoes. They found that only 35% of volcanic eruptions in that area over the past 100 years caused ash to reach above 8 km or about 26,250 feet [10].

An Australian company, Tenix Pty Ltd, holds the patent on an airborne passive IR radiometer originally developed by Dr. Fred Prata when he was employed by the Commonwealth Scientific and Industrial Research Organisation (CSIRO) located in Melbourne, Australia.[2] The system, named the Airborne Hazards Detection System (AHDS) uses a two-band detection technique similar to satellite detection techniques for volcanic ash.

In the study reported here, investigations have been conducted into means to detect the distance and warning time for an aircraft encounter with a volcanic ash cloud using window region spectral radiance emission observations. The spectral resolution, range, and instrument noise requirements have been defined for an FLI to be used to detect a volcanic ash cloud and to determine its distance from the aircraft (i.e., warning time). Two different algorithms for determining the distance to an aerosol cloud were examined. The algorithms are the "CO_2 Slicing" technique and the ratio of "window" cloud radiance relative to the clear air.

4.4.1 "CO_2 Slicing" Technique

The "CO_2 Slicing" technique expresses the distance to an object in terms of the optical depth of CO_2 between the sensor and the object. CO_2 is a uniformly mixed gas so the optical depth is proportional to the distance between the sensor and the emitting object. The optical depth, f, and therefore distance, is determined from equation 4.

$$f = \frac{R_2^{cloud} - R_2^{clear}}{R_1^{cloud} - R_1^{clear}} \tag{4}$$

where R_2^{cloud} is cloud affected CO_2 channel radiance, R_2^{clear} is the clear air CO_2 channel radiance, R_1^{cloud} is cloud affected window channel radiance, R_1^{clear} is the window channel radiance.

In this preliminary study, the ash cloud was assumed to have a thickness of 100 km and an optical depth of unity. The distance predictor (ratio of CO_2 channel radiance to window channel radiance) was produced for cloud distances of 0, 5, 10, 20, 40, and 80 km from the aircraft FLI. Figure 18 is a plot of the ratio of carbon dioxide to window channel radiance, relative to clear air, as a function of cloud distance for aircraft altitudes of 1.5, 4.5, and 9.5 km. The plot shows the result where the 791.8 cm^{-1} Q-branch is used as the CO_2 channel and 960 - 964 cm^{-1} is used as the "window" reference. There is little sensitivity to cloud distance except at 1.5 km and for the unapodized (i.e., full spectral resolution) radiance. This result implies that the CO_2 channel used for the process is too transparent (i.e., optical depth of CO_2 between the instrument and the cloud is too close to zero) to be useful for the cloud distance determination. As a consequence, more opaque CO_2 regions should be used to determine the distance between the FLI and the ash cloud.

The detection of aerosols (such as volcanic ash) with a moderate spectral resolution interferometer is made possible by a unique spectral signature that an aerosol produces

[1] PUFF is a model that simulates the movement of airborne volcanic ash in near real-time when an eruption has occurred.

[2] Dr. Prata is currently employed at the Norwegian Institute for Air Research.

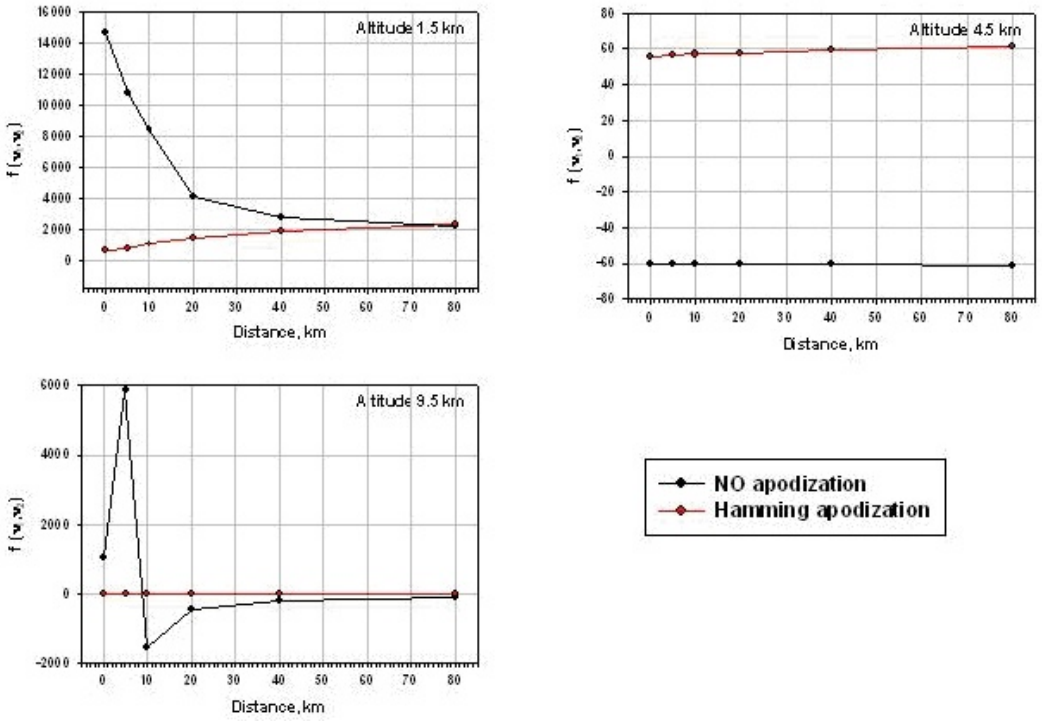

Figure 18. The ratio of carbon dioxide to window channel radiance.

in the window region relative to the spectral signature due to water droplets or ice crystal clouds, shown in Figure 19. This figure shows radiance spectra within the 11 - 12 μm window region for a downward viewing spectrometer calculated for two different aerosol particle sizes. The aerosol signature is the negative slope in the radiance distribution between 11 and 11.5 μm where the absorption decreases with increasing wavelength. For water and ice clouds, and for water vapor, the absorption increases significantly with wavelength in this same spectral region. Thus, the existence of aerosols should be easily detected from a spectral radiance emission spectrum as would be observed with an FLI.

The optical depth spectrum of volcanic ash is shown in Figure 20, which has a total optical depth of unity at 1100 cm^{-1}. The radiance and brightness temperature spectra that the FLI would observe at 1.5 km, 4.5 km, and 9.5 km with and without such an ash cloud are shown in Figure 21, assuming the aircraft is at a distance of 100 km from the ash cloud. It can be seen that the volcanic ash absorption alters the spectral distribution of radiance quite dramatically in the 800 - 1200 cm^{-1} spectral region, making the existence of a volcanic ash cloud easily detectable when the aircraft is flying above two kilometers in altitude. Near the surface (e.g., at the 1.5 km altitude), there is strong absorption by water vapor that tends to mask the aerosol spectral signature. In principle, the absolute magnitude of the radiance observed within the 800 - 1200 cm^{-1} spectral region should be proportional to the concentration of atmospheric aerosol ahead of the aircraft, whereas the amplitude of the CO_2 lines near 795 cm^{-1}, as well as the relative amplitude of the water vapor lines throughout the window region, should be indicative of how distant the volcanic ash cloud is from the aircraft. That is, the closer the aerosol layer is to the aircraft, the weaker the amplitude of the CO_2 and water vapor emission spikes seen in the spectral distribution of radiance. The absolute distance can probably be calculated using the same CO_2 slicing technique used to determine cloud altitude from satellite spectral radiance measurements [11].

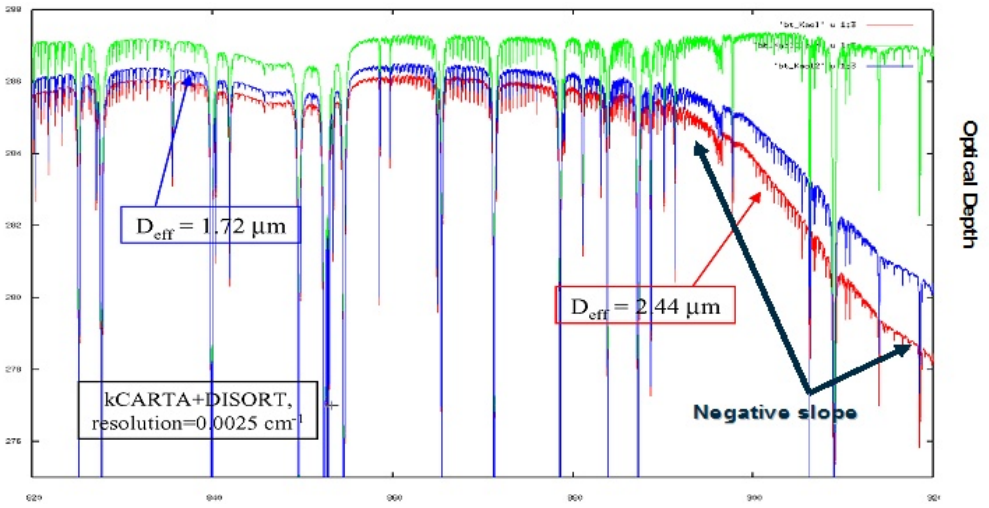

Figure 19. Aerosol particle radiance spectra within the 11 - 12 μm window region.

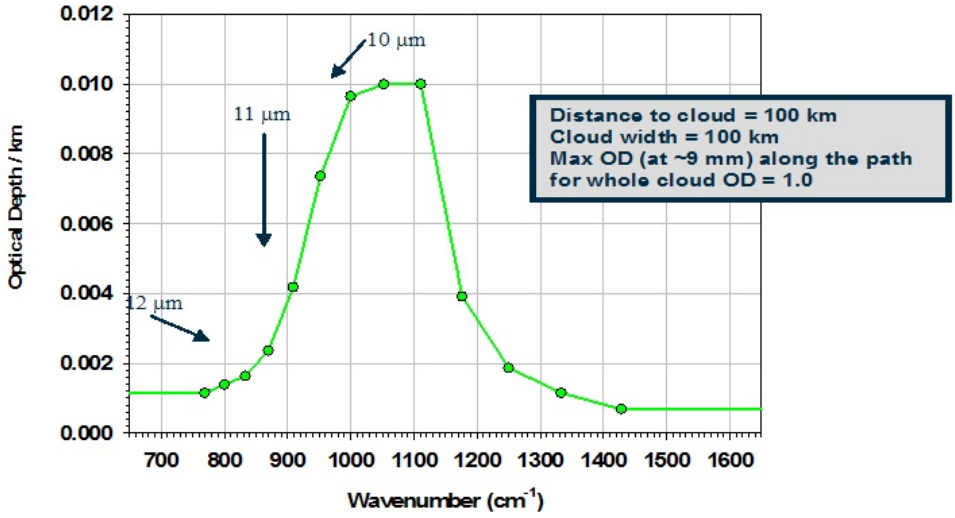

Figure 20. Volcanic ash optical depth spectrum.

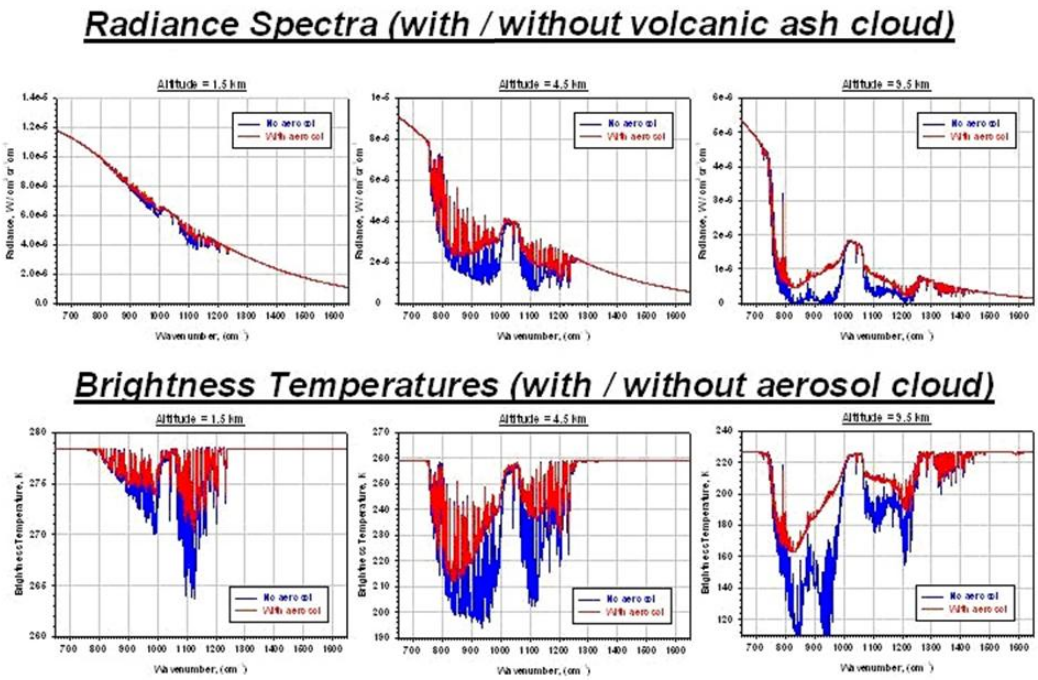

Figure 21. Brightness temperatures (with / without volcanic ash cloud).

Figure 22 shows the difference between the radiant brightness temperature spectra observed with and without a volcanic ash cloud atmospheric brightness temperature minus the clean atmospheric brightness temperature within the FLI instrument's field of view. For this situation, where the aircraft is 100 km distant from a relatively thin (i.e., the maximum spectral optical depth is unity) volcanic ash cloud there is still a very large volcanic aerosol signal in the FLI brightness temperature difference spectrum, being in excess of 50 K near 10.5 and 11.5 μm. Notice that the relative amplitude near the wavenumbers of 950 cm^{-1} and 1100 cm^{-1} reverses between high and low aircraft altitudes. This reversal in brightness temperature difference is due to the strong decrease in water vapor emission with increasing altitude at 950 cm^{-1}, relative to 1100 cm^{-1}, where it is relatively small and therefore much less dependent upon altitude. At 1100 cm^{-1}, the brightness temperature dependence with altitude is more closely related to the volcanic ash emission profile, or volcanic aerosol concentration, since the volcanic ash optical depth is a maximum at this wavenumber (see Figure 20). There may be valuable information on the distance of the aircraft from the aerosol layer in the relative amplitudes in the brightness temperature signals at 950 cm^{-1} and 1100 cm^{-1}, since the water vapor emission at 950 cm^{-1} should increase, relative to 1100 cm^{-1}, with increasing distance from the aerosol layer.

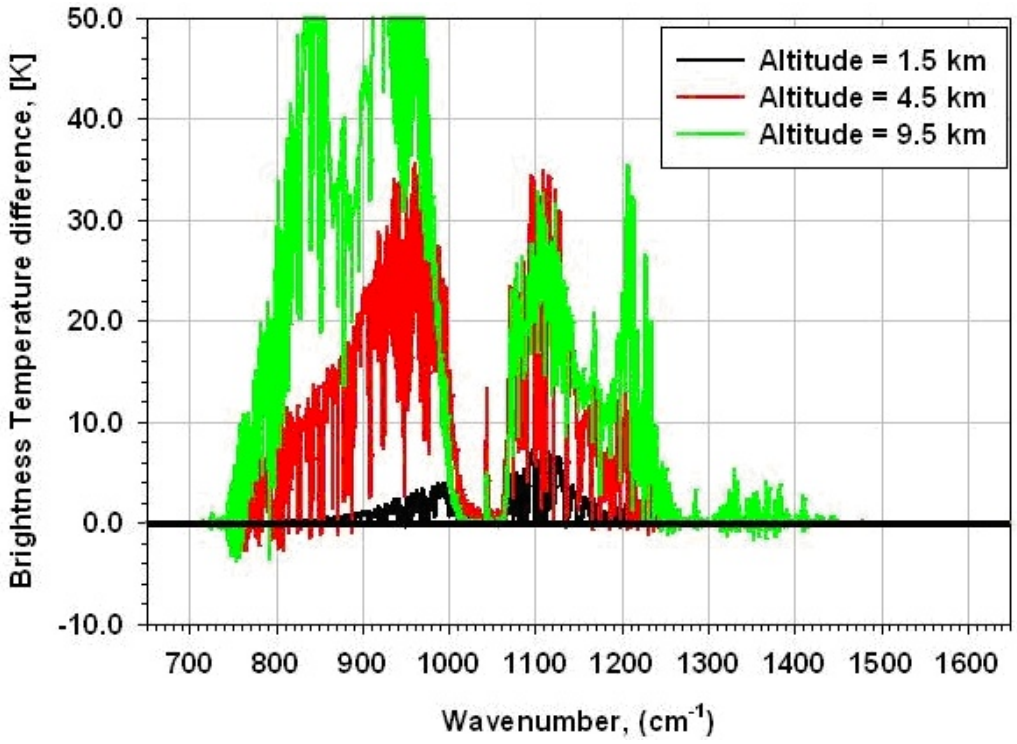

Figure 22. Difference in radiant brightness temperatures.

Figure 23 show differences in brightness temperature spectra when the ash cloud is located at distance L from the aircraft (L = 5, 10, 20, 40, and 60 km) in comparison with the corresponding brightness spectrum when L = 0 km. Ash cloud parameters: thickness along the viewing path is 20 km, maximum optical depth for the whole cloud is 0.2 at $\lambda = 9$ μm. The total amplitude of the brightness temperature differences here and their large-scale shape are clear indicators of the ash cloud presence ahead of an aircraft. They can be used to retrieve the optical depth of the cloud (i.e., concentration of aerosol particles). At the same time, the amplitudes of the H_2O, CO_2, and O_3 lines, visible in 750 - 1300 cm^{-1} range,

carry information about distance to the cloud, because they depend on the total air mass between an aircraft and an ash cloud. The farther the ash cloud is from the aircraft, the greater the amplitude of the molecular spectral lines.

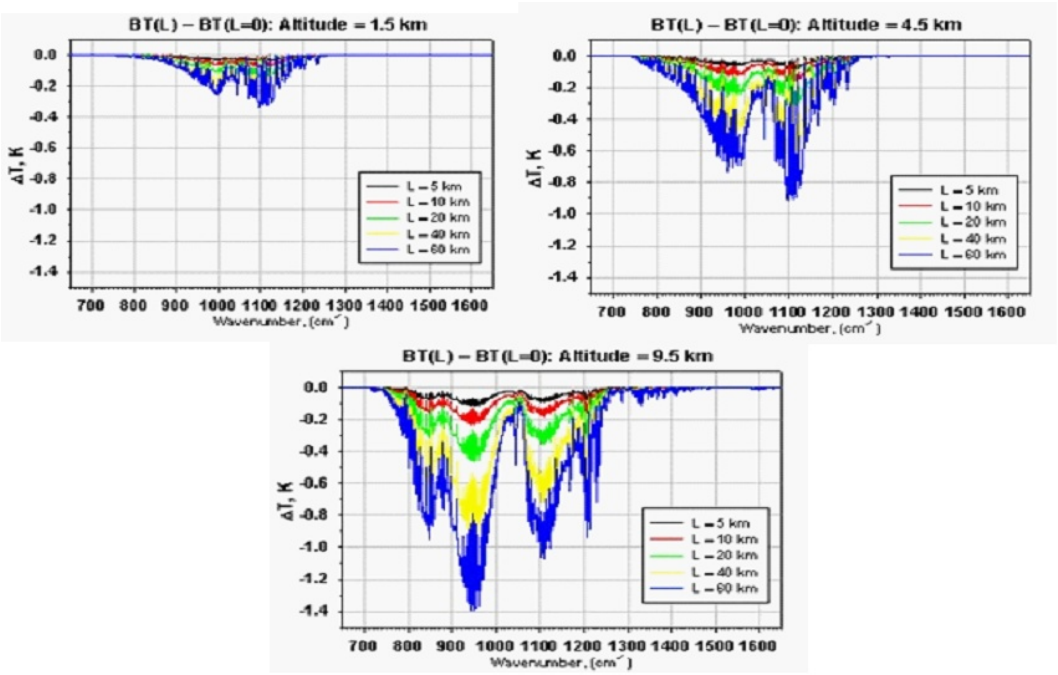

Figure 23. Difference in radiant brightness temperature spectra at a distance.

4.4.2 "Window" Channel Technique

The second method for determining ash cloud distance involves simply using the ratio of "window" cloud radiance relative to the clear air radiance to determine the ash cloud distance from the aircraft at altitudes of 1.5, 4.5, and 9.5 km. The technique is based on the fact that, because of the curvature of the atmosphere, the altitude of an object viewed along a straight-line path will vary with its distance from the instrument. Also, an ash cloud observed along the viewed path will raise the radiance that would otherwise be observed for a cloud-free path to the cold space background, since the ash cloud radiance is a function of both its temperature and its optical depth. Thus, assuming an opaque cloud, the radiance will be a function of its altitude, and therefore distance from the aircraft instrument, because of the atmospheric temperature dependence on altitude.

Figure 24 is a series of plots of the "window" cloud radiance relative to the clear air radiance as a function of aerosol distance from the aircraft. Equation 5, is used to compute the cloud radiance ratio, which shows a very strong distance signal in this measurement. To implement this technique, however, a table of this window channel ratio as a function of cloud distance for different standard atmospheric conditions and different cloud altitudes is required. A correction for the deviation of the actual atmospheric condition from the standard atmosphere could be estimated from the actual temperature and humidity measured at the aircraft. The process would be similar to estimating the surface pressure needed to obtain an altimeter setting for a particular aircraft in flight.

$$f = \frac{R_2^{cloud} - R_2^{clear}}{R_2^{clear}} \tag{5}$$

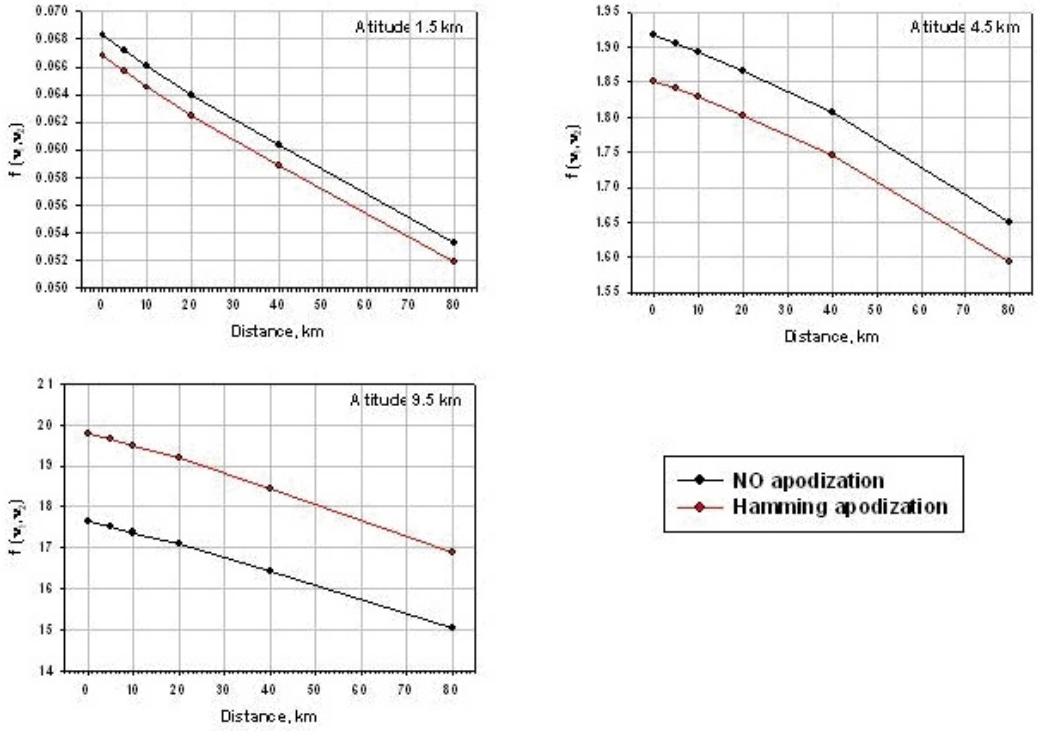

Figure 24. Ratio of cloud radiance as a function of distance.

4.5 Low Slant Range Visibility

One of the major hazards to safe flight is poor visibility during the landing portion of the aircraft flight. This condition is particularly true for commuter, business, cargo, and private aircraft, which use uncontrolled airports and which may not have precision approach capabilities such as an Instrument Landing System (ILS), Microwave Landing System (MLS), or Global Positioning System (GPS). At uncontrolled airports, there may be other obstacles (e.g., other aircraft) on the runway, which may not be seen by the pilot during a landing approach when Instrument Meteorological Conditions (IMC) exist due to poor visibility.

An FLI imaging spectrometer can be used to observe the scene ahead of and below the aircraft from multi-spectral images of the radiance spectrum emitted by these scenes. Because the optical depth of the atmosphere between the scene and the aircraft produces unique signatures in the radiance spectrum observed for each pixel of an imaging FLI, the effect of the absorbing atmospheric constituents (e.g., water vapor and aerosol) on the scene radiance can be corrected, thereby providing the pilot with enhanced imagery of the scene conditions ahead of the aircraft.

The algorithm most suitable for implementing these corrections in a real-time fashion is called "EOF Regression" or "PC Regression" [12], [13], [14], [15]. In this technique, the radiance spectrum is represented by a small number of Empirical Orthogonal Functions (EOFs), or Principle Components (PCs), which represent the information content of the

radiance spectrum in terms of a small number of statistically independent amplitudes, or PC scores, of the radiance spectrum representation functions (i.e., the EOFs or PCs). By definition, the EOFs, or PCs, are statistically optimal in the sense that no other set of spectral functions can be used to represent the observed radiance spectra with as small a number of independent variables (i.e., the EOF amplitudes or PC scores). Thus, EOF or PC expansions provide the most efficient representation of any particular spectral radiance data set.

The algorithm to produce an enhanced, or clear, image of the background from the FLI imaging spectrometer data involves predicting for each detector array pixel the background scene temperature from the spectral radiance distribution observed by that detector element. The prediction equation takes the form of a linear regression equation where the predictand is the background surface temperature and the predictors are the amplitudes, or PC scores, of the first few EOFs, or PCs, used to represent the observed radiance spectrum. As will be seen, only three or four functions, depending on spectral resolution, are required to fit the window region spectrum used to infer the surface background temperature.

The EOFs and coefficients of the prediction regression equations are obtained from a large statistical sample of FLI radiance spectra simulated for a variety of surface air temperature, surface skin temperature, aerosol, and surface visibility conditions using the LBLRTM described earlier in this report. As is common practice in the use of EOFs for remote sensing [16], the Eigenvectors are computed without the addition of noise to the simulated spectra. However, regression equation coefficients are derived using EOF amplitudes obtained from radiance spectra with random noise added at a level expected to exist for actual observations. A detailed mathematical description of the algorithm is provided below.

The algorithm is based on Principal Component Analysis (PCA) of IR spectra obtained for slant viewing of the ground from an aircraft. To predict the temperature of a ground object, the following regression scheme is used

$$T_p = T_0 + \vec{r} \cdot \vec{P} \tag{6}$$

where where T_0 is the surface air temperature, $\vec{r}$ is the vector of decomposing coefficients (PC-scores) for a given measured spectrum, $R(\nu)$, on some pre-calculated basis of Empirical Orthogonal Functions (EOF), $\{E_i\}$, and $\vec{P}$ is a vector of predicting coefficients.

$$\vec{r_i} = R(\nu) \cdot E_i(\nu) \tag{7}$$

where the subscript, i, refers to the EOF or PC number. $E_i(\nu)$ and $\vec{P}$ are calculated from the specially-designed training set of spectra.

LBLRTM was used to generate the basic set of spectra, $R(\nu, T_0)$, for a given atmospheric model (the US standard atmosphere), the geometry of observations (altitude h and zenith angle α of the viewed scene), for nominal ground temperature T_0, and for different models of aerosol loading (urban and rural aerosols) with visibilities of 5, 4, 3, and 2 km (i.e., 8 cases total).

To recalculate the spectra for another possible ground surface temperature, T_s, the following equation was used:

$$R(\nu, T_s) = R(\nu, T_0) + \tau(\nu) \cdot [B(\nu, T_s) - B(\nu, T_0)] \tag{8}$$

where $\tau(\nu)$ is total transmittance of the atmosphere for a given aerosol model, and B is the Planck function.

For each of 11 basic ground temperatures selected in one degree increments between the nominal ground temperature, plus and minus five degrees (i.e., $T_s = T_0 - 5$ K, ..., T_0, ..., $T_0 + 5$ K), 100 Gaussian random ground temperatures (with mean = T and $\sigma = 0.5$ K)

were generated, and then corresponding spectra were computed using equation (8). Thus, the full training set has 8800 spectra [i.e., $N = 8800 =$ (2 aerosol models) $\times$ (4 visibilities) $\times$ (11 basic) $\times$ (100 random perturbations of each ground temperature)] each spectrum having a different ground temperature and a varying aerosol loading.

Figure 25 shows 16 example FLI spectra computed for a spectral resolution of 2.5 cm^{-1} for a ground temperature equal to the surface air temperature of 288.2 K. Brightness temperature spectra, computed for the US Standard atmosphere for four different aerosol models (urban aerosol, rural aerosol, tropospheric extinction, and radiation fog) and four different visibilities (5 km, 4 km, 3 km, and 2 km) are shown in the figure. The aircraft altitude is 1.22 km and the instrument is viewing the ground at an angle of 20 ° below the horizon (atmospheric path between the aircraft and the surface is 3.6 km). There are four different extinction models (tropospheric extinction, urban aerosol, rural aerosol, and radiation fog) and four different surface visibilities (5, 4, 3, and 2 km) assumed for these calculations. The red spectrum represents the mean of the sixteen different spectra. It can be seen that the discrepancy between the observed brightness temperature and the ground temperature is related to the amplitude of the spectral structure across the window region: the larger the attenuation, the smaller the spectral structure when the ground temperature is equal to the surface air temperature. Also, different types of absorbers possess different broad-scale spectral shapes. Note that radiation fog, represented by the bottom four curves in the figure, has a distinct maximum brightness temperature (i.e., minimum extinction) near 10 μm (1000 cm^{-1}) while the aerosol models tend to have numerous brightness temperature maxima across the band.

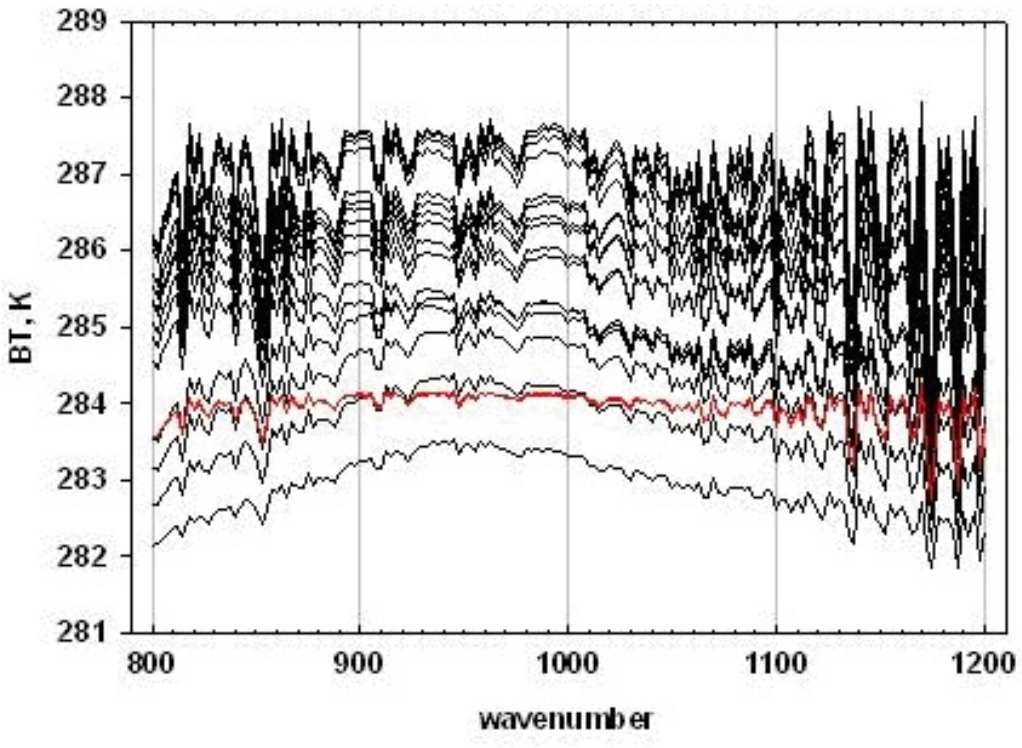

Figure 25. Brightness temperature spectra, at 2.5 cm^{-1} spectral resolution.

Figure 26 shows the FLI brightness temperature spectra for a rural extinction aerosol for 11 different ground temperatures ranging between 270 K and 310 K. The surface air temperature is 288.2 K and the surface visibility is 3 km. The aircraft altitude is 1.22 km and

the view angle is 20 ° below the horizon. Figure 26 is presented to illustrate the dependence of the spectral variability on the discrepancy between ground temperature and the surface air temperature. As can be seen, the larger the discrepancy between the surface air and ground temperatures, the greater the spectral variability of the FLI window spectrum. Also note that the absorption line features flip when the sense of the difference between the ground and air temperature changes. It is both the large scale and small-scale spectral features of the FLI spectra that relate the observed brightness temperature to the actual ground temperature, thus enabling the correction of FLI brightness temperature imagery for the attenuation by the intervening atmosphere.

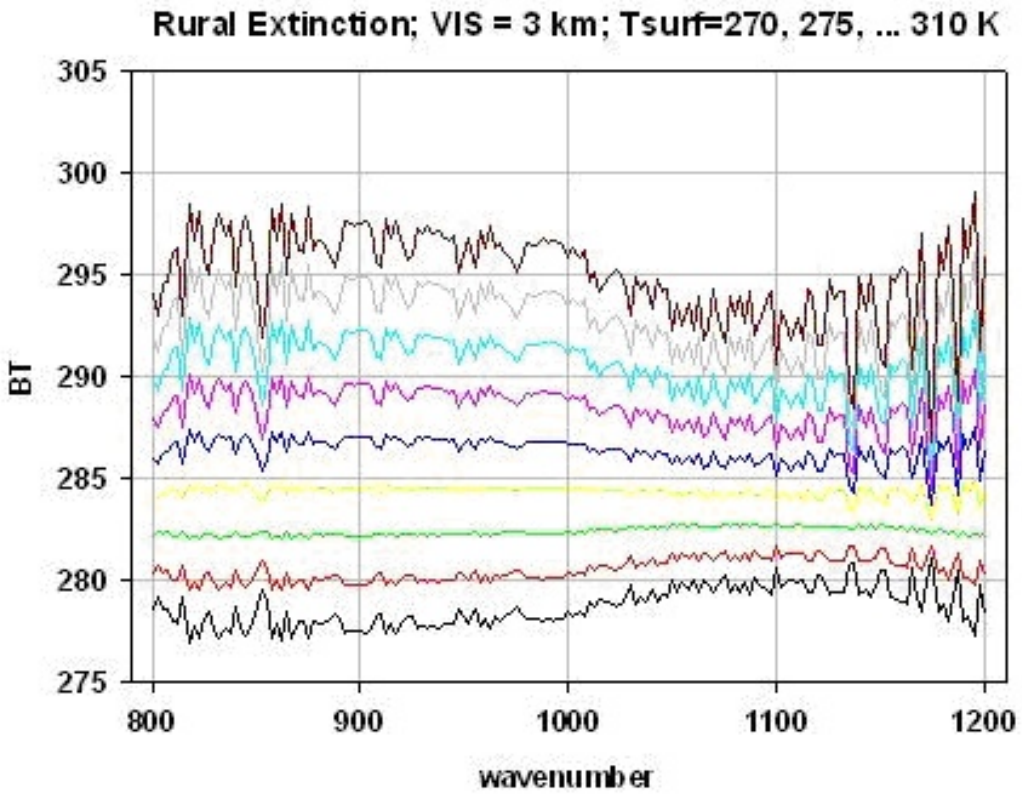

Figure 26. FLI brightness temperature spectra for a rural extinction aerosol.

Empirical Orthogonal Functions: The training spectral radiance data set described above is used to calculate a mean spectrum

$$R_0(\nu) = \frac{1}{N}\sum_{n=1}^{N} R_n(\nu, T_n) \tag{9}$$

and a statistical covariance matrix

$$cov_{i,j} = \frac{1}{N}\sum_{n=1}^{N}[R_n(\nu_i) - R_0(\nu_i)] \cdot [R_n(\nu_j) - R_0(\nu_j)] \tag{10}$$

where N is the number of radiance spectra in the training data set. A set of empirical orthogonal functions $\{E_i\}$ is calculated as eigenvectors of the covariance matrix, cov, ordered in decreasing magnitude of the eigenvalues.

Figure 27 shows the FLI brightness temperature eigenvectors, for a spectral resolution of 2.5 cm^{-1}, computed from a sample of 4400 urban aerosol and ground temperature conditions, assuming the US Standard Atmosphere. The eigenvectors are computed for an aircraft altitude of 1.22 km and a view angle of 20 degrees below the horizon. The spectral resolution is 2.5 cm^{-1}. As can be seen the different eigenvectors portray different degrees of spectral variability. Thus, the amplitudes of these EOFs (i.e., the r_i's of equation (7), above), carry the information regarding the magnitude of the spectral variability of the observed brightness temperature spectra.

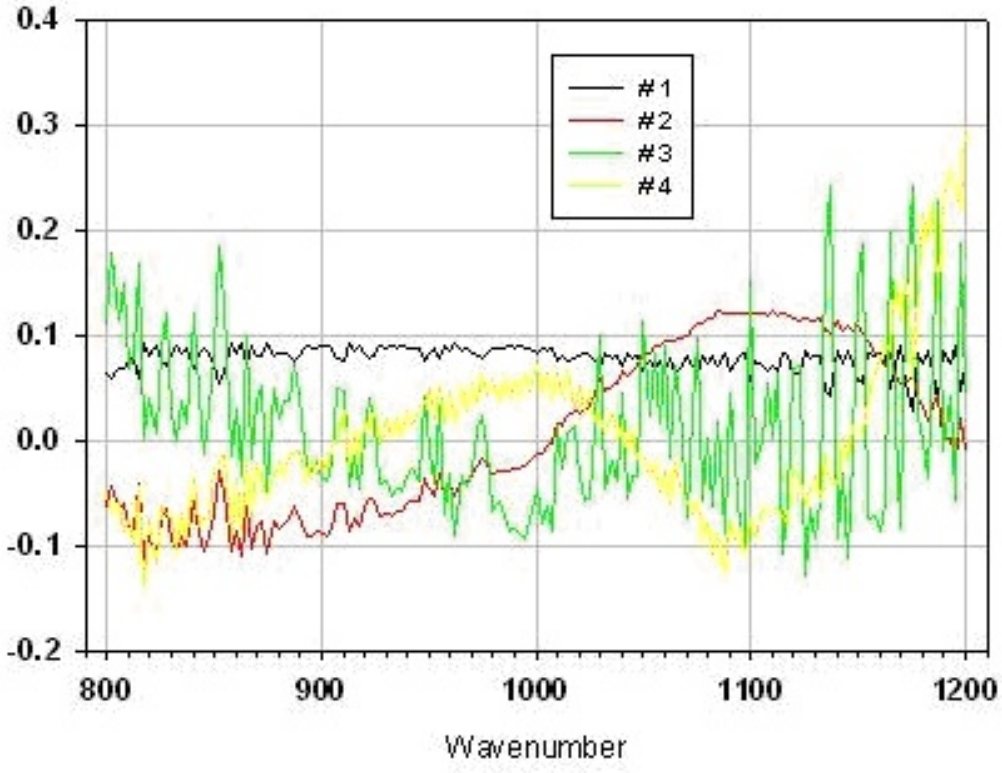

Figure 27. FLI brightness temperature spectra for urban aerosol conditions.

Figure 28 shows the eigenvalues, λ, (the sum of which is the total variance) associated with the eigenvector representation of 8800 radiance spectra computed for both rural and urban aerosol conditions. The surface visibility ranges between 2 and 5 km and the ground temperature ranges between $\pm$ 5 K of the nominal surface air temperature of 288.2 K.

The results are shown for both the 2.5 cm^{-1} and 0.6 cm^{-1} spectral resolutions considered in this study. Note that the square root of λ is plotted on a logarithmic scale in order to differentiate the two curves for the higher order EOFs. There is additional information content for the higher spectral resolution, which increases with increasing EOF number. It is noted that even though nearly twice as many EOFs are needed to explain all the variance of the high resolution spectra, as compared to the lower resolution spectra, the absolute magnitude of the residual variance is relatively small for EOF numbers beyond three.

Vector of prediction regression coefficients $\vec{P}$: Having the basis of empirical orthogonal functions, the matrix $C = |c_{i,j}|$ can be calculated, where $c_{i,j}$ are PC-scores for all spectra from the training data set; that is,

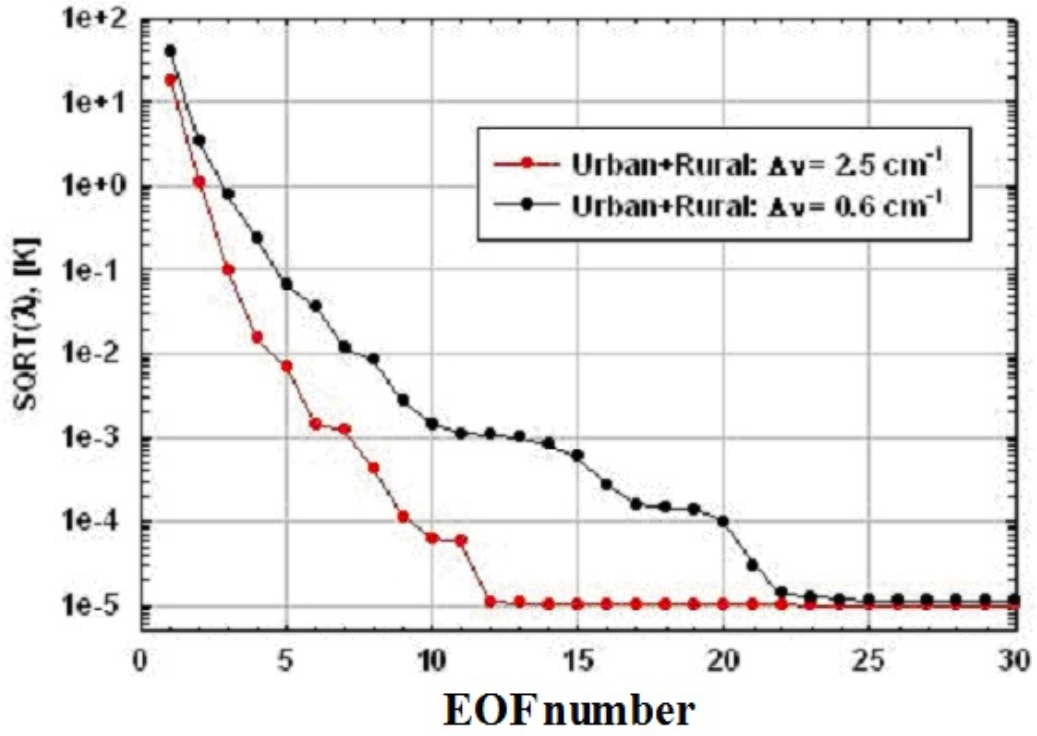

Figure 28. Eigenvalues of a matrix of the statistical covariance.

$$c_{i,j} = R_i \cdot E_j \tag{11}$$

where i refers to the training data set sample number and j refers to EOF number.

The elements of prediction vector $\vec{P} = \{p_j\}$ are computed by solving the system of linear equations $c_{i,j} \cdot p_j = T_i - T_0$, or in matrix form

$$CP = \Delta T. \tag{12}$$

Because equation (12) is an over-determined system of equations (i.e., more equations than unknowns), a least squares solution minimizes the sum of the squares of the differences between the actual ground temperatures and predicted ones. Thus, solving for that P for which $(\Delta T - CP)^T(\Delta T - CP) = min.$, the least squares solution is

$$P = (C^T C)^{-1} C^T \Delta T. \tag{13}$$

The solution is conditioned with respect to instrument noise amplification by adding Gaussian random noise, with standard deviation, σ, equal to the expected measurement noise, to each radiance measurement in the training data set before calculating the matrix C using equation (11).

Figure 29 shows the root-mean-square error of predicted surface temperature for 8800 spectra simulated for urban and rural aerosol conditions with surface visibilities ranging between 2 and 5 km and surface temperatures ranging between 283 and 293 K, for Standard Atmospheric conditions with a surface air temperature of 288.2 K. The results for four different FLI instrumental noise levels are shown. The number of EOFs required to predict the background temperature is four, or less, depending on spectral resolution and instrumental noise. This result is important in that it should be easy to perform a simple

two, three, or even four eigenvector regression estimate of surface temperature for every pixel of an imaging interferometer in real time aboard the aircraft. It can also be seen that for realistic noise levels of 0.3 K, the background temperature can be estimated with an accuracy close to 0.5 K, which is only slightly poorer than the brightness temperature noise level. Scene contrasts on the order of a one half of a degree, or more, should be easily seen in the atmospheric-extinction-corrected FLI imagery.

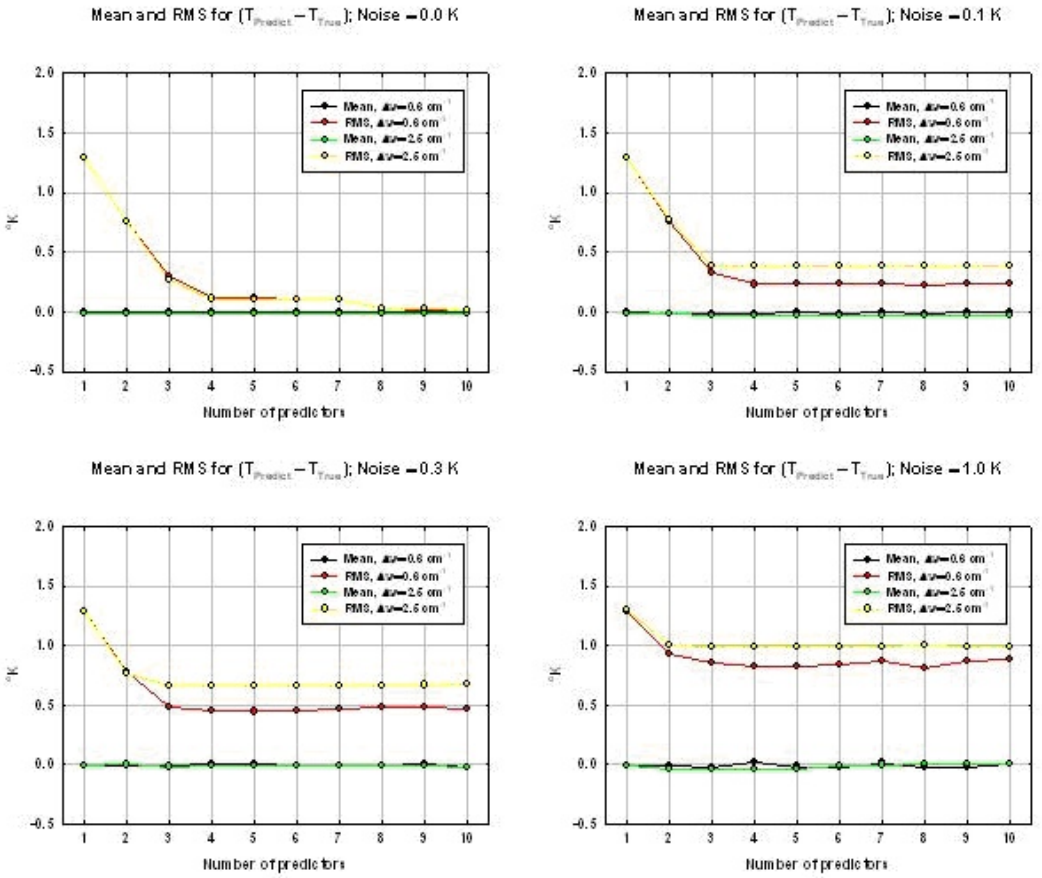

Figure 29. Root mean square error of predicted surface temperature.

Figure 30 shows, for a spectral resolution of 2.5 cm^{-1}, the dependence of predicted ground temperature accuracy on the surface visibility condition. The dependence of the accuracy on surface visibility decreases with increasing number of eigenvector amplitude predictors used for the extinction correction process; however, the residual dependence is strongly a function of instrument brightness temperature measurement noise level. If the instrument noise level can be maintained at a level near 0.1 K, then accuracies better than 0.3 K can be achieved, even under Low Instrument Flight Rules (LIFR) flight conditions (e.g., visibility $\leq$ 2 km).

FLI imagery simulations Regression prediction equations were specified to correct simulated FLI imagery for atmospheric extinction. Table 1 is a summary of the various observing conditions used for the simulations conducted to determine the radiance eigenvectors and regression equation prediction coefficients. Ranges of values for some parameters are listed.

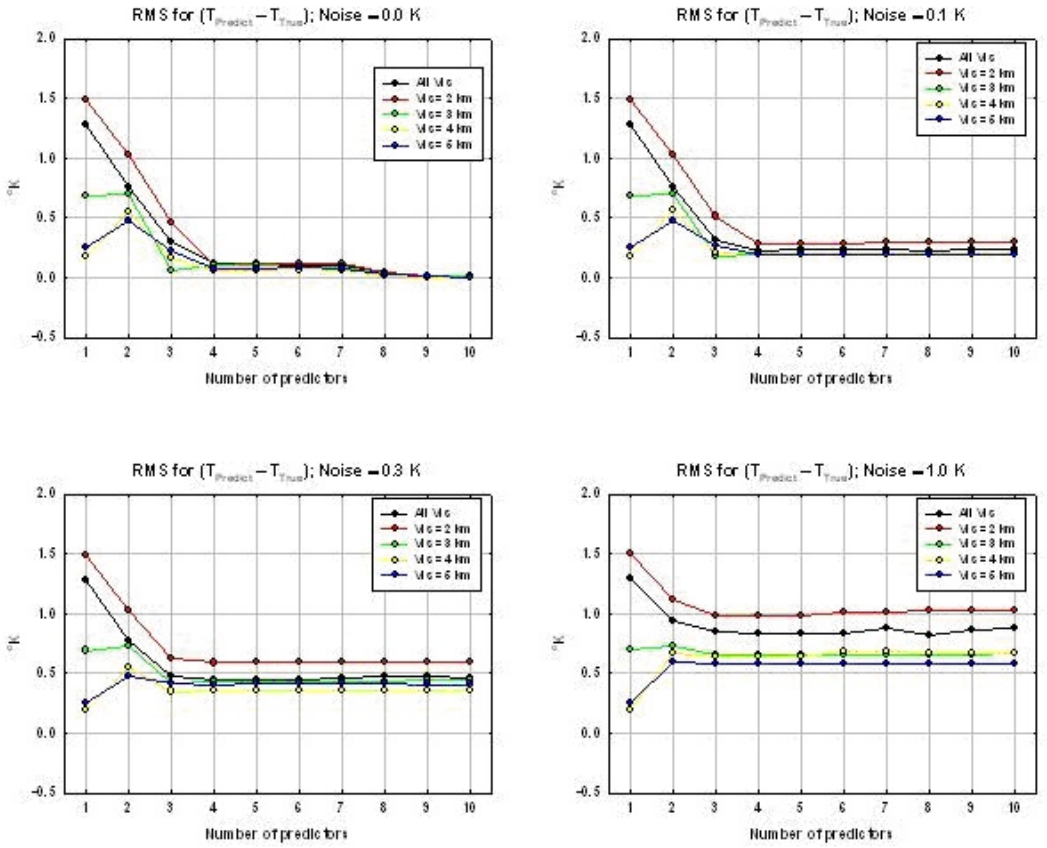

Figure 30. Dependence of predicted ground temperature accuracy.

Table 1. FLI INSTRUMENT ATMOSPHERIC/SURFACE SIMULATION VALUES

Parameter	Values
Wavenumber range	800 - 1200 cm^{-1}
Wavenumber resolution	2.5 / 0.6 cm^{-1} (low/high)
Atmospheric profiles	US Standard Atmosphere
Aerosol Models	LBLRTM Urban Aerosol and Rural Aerosol
Surface visibility	5.0, 4.0, 3.0, and 2 km
Surface air temperature (T_0)	288.2 K
Ground temperature (T_p)	283.2 to 293.2 K in increments of 1 $\pm\epsilon$ with $\sigma(\epsilon) = 0.5$ K
Aircraft Altitudes (h)	h = 4000 ft. ($\sim$1.22 km) and h = 1000 ft. ($\sim$0.3 km)
Zenith angle of observations	$\alpha = 110\,^\circ (-20\,^\circ$ to horizon)
Slant range to the ground target	$\sim$ 3.6 km for h = 4000ft.; $\sim$ 0.9 km for h = 1000ft.
Number of predictors	4
Brightness temperature noise	$\sigma(\epsilon) = 0.1$, 0.3, and 1.0 K

Figures 31 through 35 show imagery created from the FLI's most transparent channel brightness temperature and EOF regression predicted background temperature for a variety of atmospheric visibility, instrument noise level, and aircraft altitude conditions. The scene is composed of three radiating target temperatures, grass, a concrete runway, and a vehicle on the runway, their temperatures indicated in the figure legends. These radiating temperatures might represent a night-time condition where the runway is radiatively cooler than the surrounding grass. The radiating temperature difference might result from the difference in the infrared emissivity of the concrete (or asphalt) and/or the more rapid infrared cooling of the runway surface at night than the surrounding grass-covered dirt. The opposite temperature differential between the runway and the surrounding turf might be expected to occur during the day when the surface is illuminated by the sun. As simulated, one would expect contrast between a vehicle, or other object, on the runway due to its different thermal and emissivity properties from those for the runway on which it is positioned.

The EOF-regression-predicted background imagery does a remarkable job of enhancing the contrast between the runway and a possible obstruction on it. As expected, slightly better results are obtained at high spectral resolution, particularly for high noise measurement conditions. However, considering the fact that the measurement noise level of a 2.5 cm^{-1} FLI should be smaller than that for a 0.6 cm^{-1} resolution FLI (a factor of $\sim$2 for the same Michelson mirror scan rate) and the fact that the refresh rate would be improved by a factor of 4 as a result of the shorter interferogram length, the 2.5 cm^{-1} FLI system is preferred for this particular application. Further investigations into the dependence of the FLI slant range imagery on spectral resolution might reveal that even poorer spectral resolution (shorter interferogram scan time) measurements would be sufficient, thereby enabling even more continuous imagery than is possible with the higher spectral resolution system. The EOF regression algorithm works remarkably well and has the ability to retrieve very clear scene condition imagery under very low visibility conditions, even over large slant ranges. This result indicates that an FLI imaging spectrometer would be extremely useful in the cockpit to assist the pilot in seeing hazardous obstructions along the flight path and for enabling visual landings under low visibility conditions.

Figure 31 is a comparison between most transparent channel brightness temperature imagery with EOF regression enhanced imagery for an aircraft altitude of 4000 ft (slant range equal to 3.6 km), and instrument noise level of 0.1 K, and surface visibility of 1 km ($\sim$ 0.6 mi) for 0.6 cm^{-1} and 2.5 cm^{-1} spectral resolutions. The scene is composed of three radiating target temperatures, grass at a temperature of 288 K, a concrete runway at a temperature of 286 K, and a vehicle on the runway with a temperature of 290 K.

Figure 32 is a comparison between most transparent channel brightness temperature imagery with EOF regression enhanced imagery for an aircraft altitude of 1000 ft (slant range equal to 0.8 km), and instrument noise level of 0.3 K, and surface visibility of 0.25 km ($\sim$ 0.16 mi) for 0.6 cm^{-1} and 2.5 cm^{-1} spectral resolutions. The scene is composed of three radiating target temperatures, grass at a temperature of 288 K, a concrete runway at a temperature of 287 K, and a vehicle on the runway with a temperature of 289 K.

Figure 33 is a comparison between most transparent channel brightness temperature imagery with EOF regression enhanced imagery for an aircraft altitude of 1000 ft (slant range equal to 0.8 km), and instrument noise level of 1.0 K, and surface visibility of 0.25 km ($\sim$ 0.16 mi) for 0.6 cm^{-1} and 2.5 cm^{-1} spectral resolutions. The scene is composed of three radiating target temperatures, grass at a temperature of 288 K, a concrete runway at a temperature of 286 K, and a vehicle on the runway with a temperature of 290 K.

Shown in figure 34 is a comparison between most transparent channel brightness temperature imagery with EOF regression enhanced imagery for an aircraft altitude of 1000 ft (slant range equal to 0.8 km), and instrument noise level of 1.0 K, and surface visibility of 0.5 km ($\sim$ 0.32 mi) for 0.6 cm^{-1} and 2.5 cm^{-1} spectral resolutions. The scene is composed of three radiating target temperatures, grass at a temperature of 288 K, a concrete runway

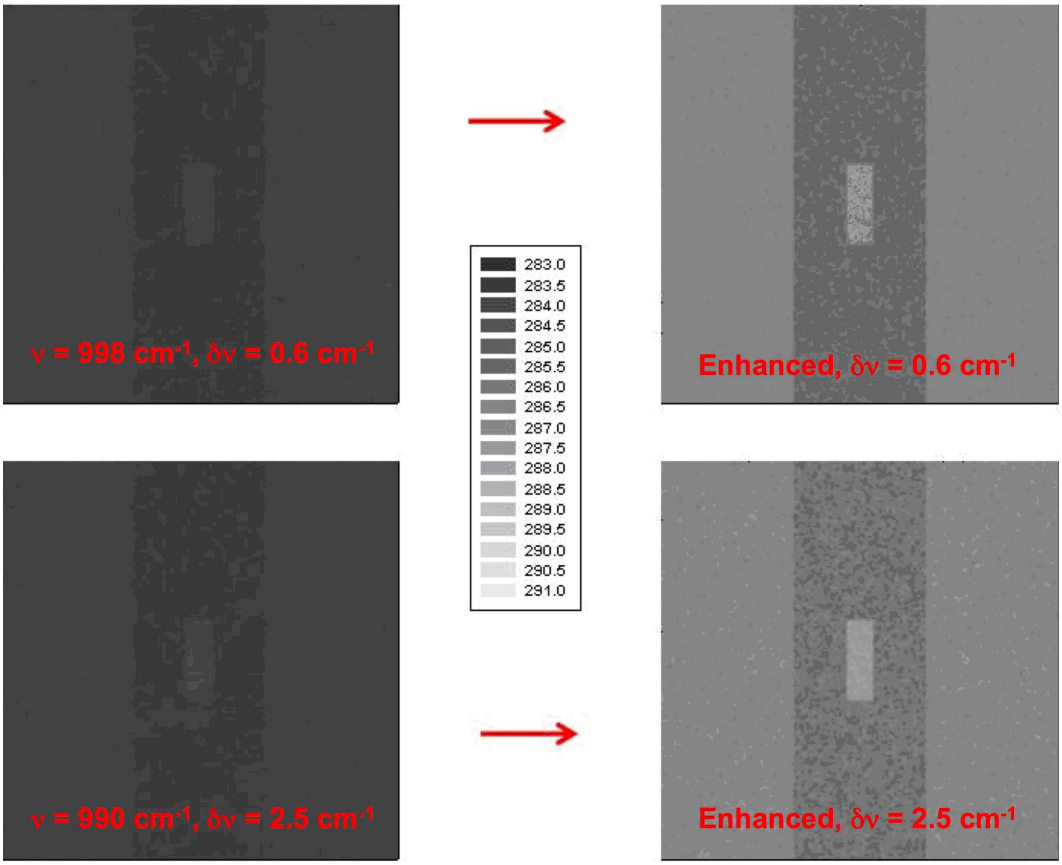

Figure 31. Visibility = 1 km, slant range = 3.6 km, noise level = 0.1 K.

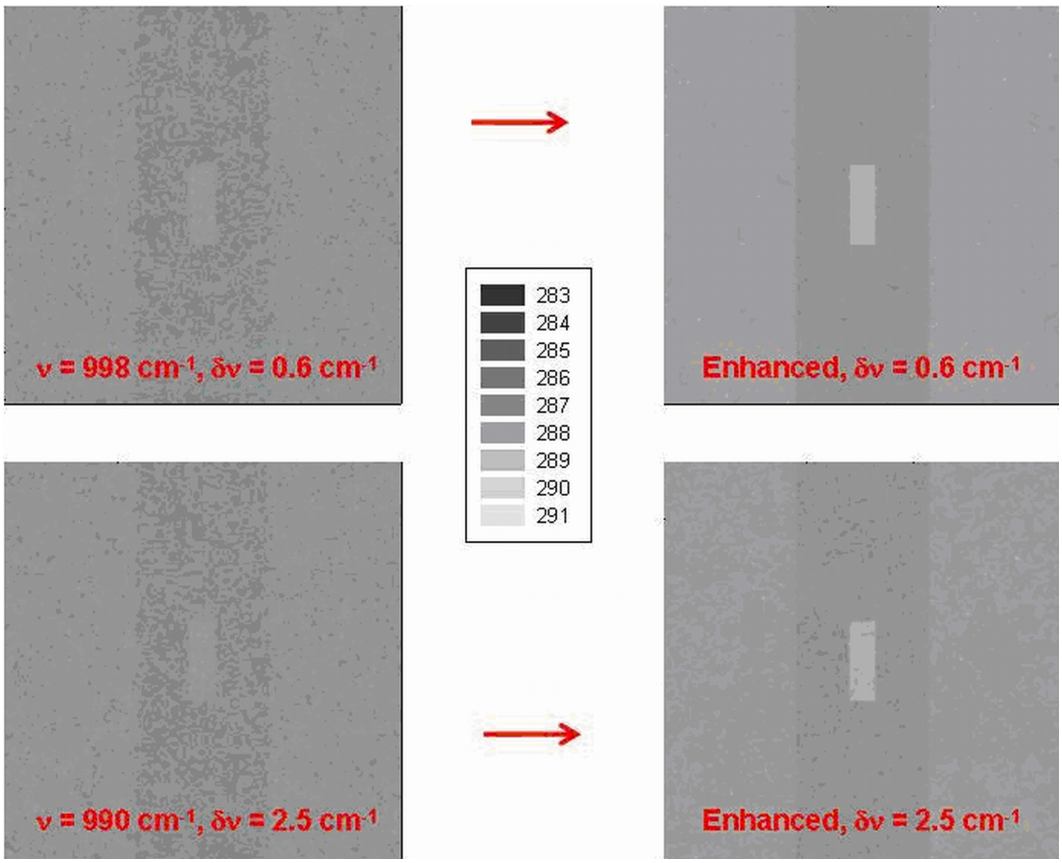

Figure 32. Visibility = 0.25 km, slant range = 0.8 km, noise level = 0.3 K.

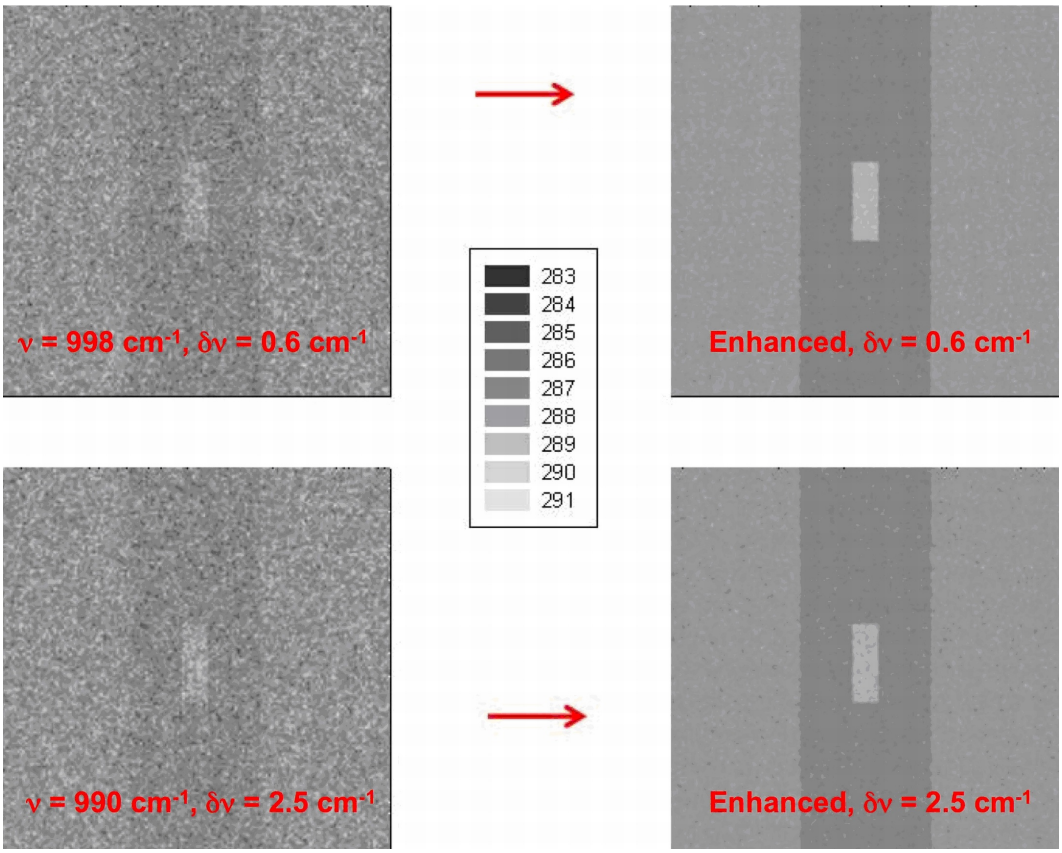

Figure 33. Visibility = 0.25 km, slant range = 0.8 km, noise level = 1.0 K.

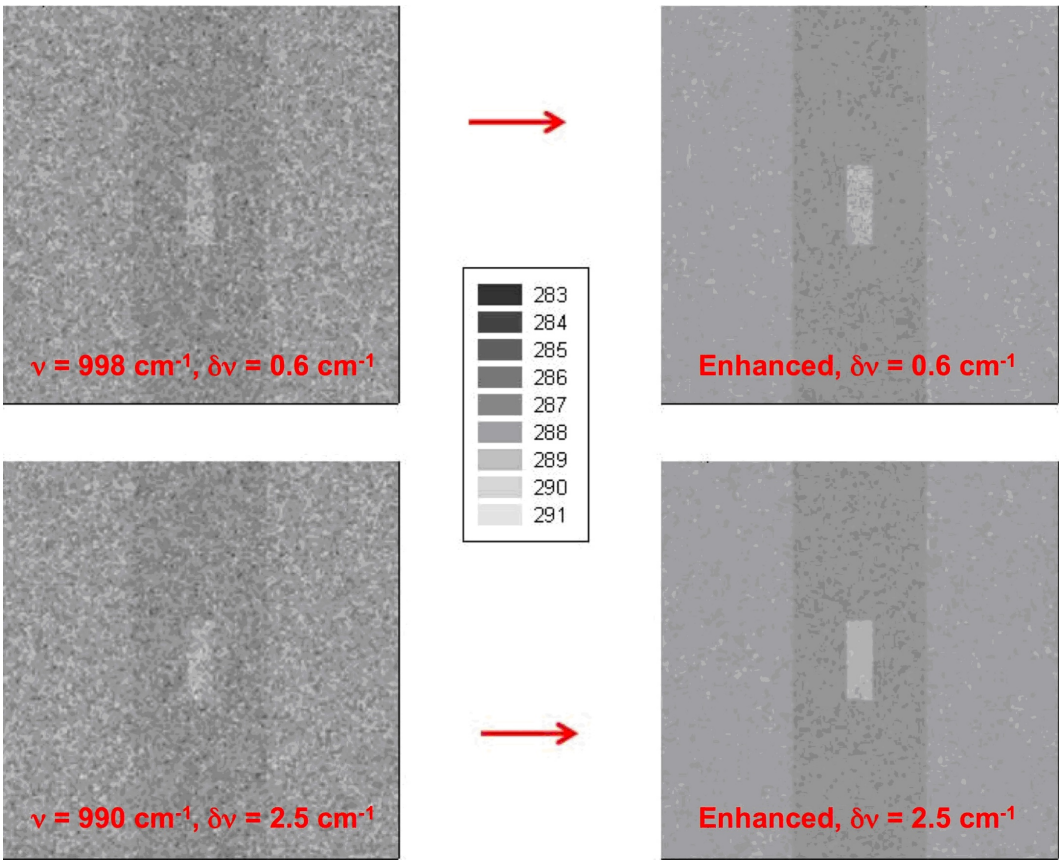

Figure 34. Visibility = 0.5 km, slant range = 0.8 km, noise level = 1.0 K.

at a temperature of 287 K, and a vehicle on the runway with a temperature of 289 K.

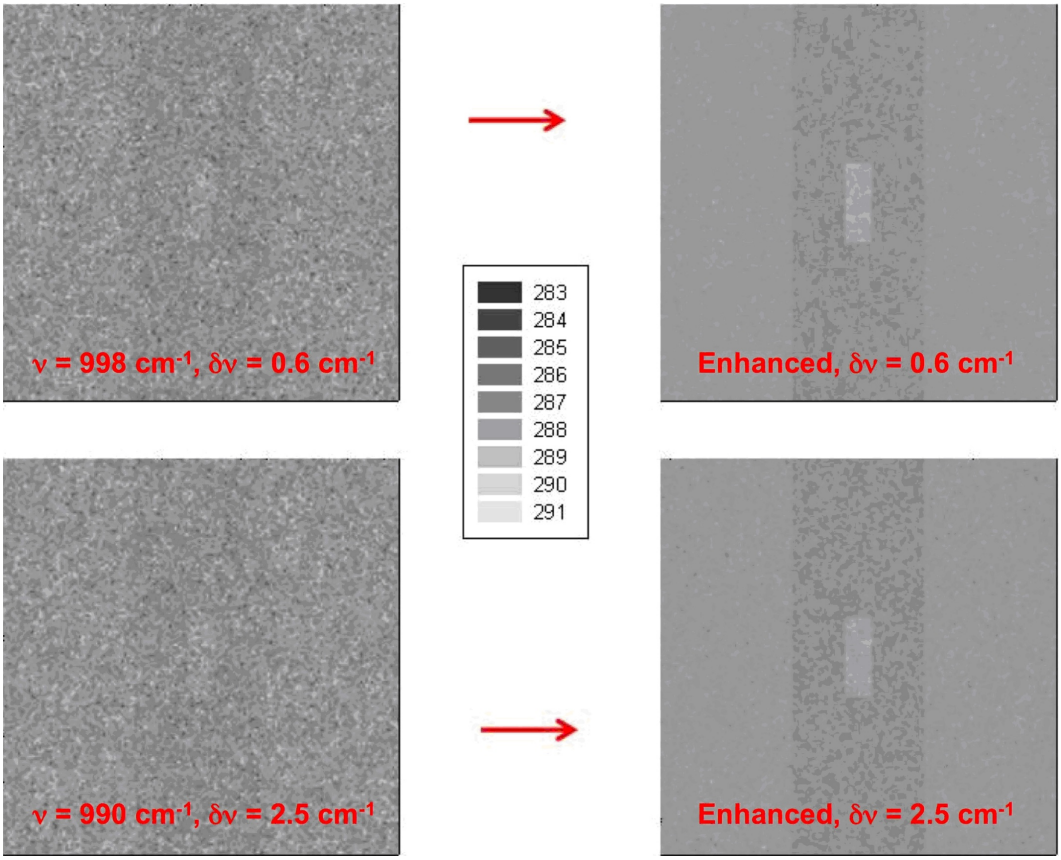

Figure 35. FLI settings from figure 33 but targets at higher temperatures.

Figure 35 is a comparison between most transparent channel brightness temperature imagery with EOF regression enhanced imagery for an aircraft altitude of 1000 ft (slant range equal to 0.8 km), and instrument noise level of 1.0 K, and surface visibility of 0.25 km ($\sim$ 0.16 mi) for 0.6 cm^{-1} and 2.5 cm^{-1} spectral resolutions. The scene is composed of three radiating target temperatures, grass at a temperature of 288 K, a concrete runway at a temperature of 287 K, and a vehicle on the runway with a temperature of 289 K.

Based on these sensitivity studies, an imaging FLI spectrometer is very useful for providing enhanced vision in the cockpit of an aircraft. The imagery can be greatly enhanced using a multi-spectral processing algorithm which retrieves the background scene temperature distribution from the observed radiance spectra. The algorithm is a simple linear operator and therefore could be implemented for the provision of real-time cockpit displays of enhanced vision of the scene ahead of the aircraft.

The algorithm was demonstrated under a restricted set of aircraft altitude and atmospheric conditions. Much more work needs to be performed to demonstrate the robustness of the algorithm and to define the actual measurement and display characteristics of a practical image enhancement system.

5 Characterization Studies of Other Hazards

Characterization studies have been performed to determine the possibility of detection of wake vortices, dry wind shear, and icing by an FLI instrument. Hazard phenomenology has been investigated that supports detection by an FLI sensor, such as temperature and water vapor content that were crucial to the sensitivity studies. In addition, other phenomenology, such as exhaust gas constituents and the optical properties of liquid water and ice, were examined as a further means of detection with an FLI.

5.1 Wake Vortex

The possibility of detecting wake vortices with an imaging FLI instrument has been investigated. A study of the temperature structure, time evolution, and exhaust entrainment in wake vortices was conducted so that the likelihood of detection with an FLI system could be determined. To prevent hazardous wake turbulence encounters between aircraft, airports operate with the Instrument Flight Rules (IFR) longitudinal spacing requirement. The spacing requirement is based on factors such as the geometry of the airspace and runways and the size of the aircraft involved. Through the Aircraft Wake VOrtex Spacing System (AVOSS) project, NASA set the goal of demonstrating a technology that could provide aircraft with real-time wake avoidance information, thereby allowing a greater capacity of aircraft landings by reducing the longitudinal spacing requirement. AVOSS focused on vortices created during takeoff and landing [17].

There are several models available that describe the vorticity, shape, size and temperature profiles of wake vortices created by aircraft. Temperature changes and water concentrations are based on the properties of fluid dynamics. Because of the interest in condensation trail (contrail) cloud formation and the effects on global climate, most of the data on exhaust entrainment is taken at or modeled for cruise altitudes. However, much of the information that is gathered during the study of contrails is relevant to wake vortices near the ground as well.

There are four phases of contrail evolution which include Jet, Vortex, Dissipation, and Diffusion. The Jet stage lasts 1-20 s; the Vortex phase lasts 20-100 s; the Dissipation phase lasts 100-1000 s; and the Diffusion phase can last hours.[3] During the Jet phase, aircraft engine exhaust material is entrained in the vortices. During the Vortex phase, the vortices descend due to mutual induction [20], [18]. This study focuses on the Jet and Vortex phases as the two most relevant for vortices that affect runway spacing requirements, though some vortices can last several minutes in the runway environment.

When a vortex is formed, the air in the core expands so that there is a pressure differential across the swirling air. The pressure differential provides the centripetal force that is required to keep the air in circular motion. Therefore, the air in the core is cooled by an initial adiabatic expansion. The temperature at the core of a wake vortex is typically $6-7\,^{\circ}\mathrm{C}$ cooler than the ambient air. However, this temperature differential depends strongly on the core size [21].

There have been several studies conducted that measured temperature drops in the vortices of an aircraft. Using anemometers, Hallock et al. often measured a $1\,^{\circ}\mathrm{C}$ decrease in temperature in vortices in a study at Frankfurt/Main International Airport [22]. Adamson and Morrison used a scanning multi-band radiometer in 1991 to make low-resolution images of wake vortices, using a two-band differential signal processing technique to maximize the

[3] There is some disagreement here on whether there are three or four phases, and what the timescales are. We have chosen to use the definitions outlined by Paugam et al. (2006) [18] but the definitions in reference [19] are similar. They define three regions of interest: jet, vortex, and plume dispersion. The time scales associated with these regimes are 0-10 s for the jet, 10-100 s for the vortex, and 100 s to tens of hours for plume dispersion.

system's response at a desired range. The vortex signature was normally a cold infrared wake at -2 to $-3\,^{\circ}$C below ambient, although the DC-10 produced a temperature difference of $-7\,^{\circ}$C on one occasion [23]. It should be noted that both Hallock and Adamson measured one incident where the vortex registered a warmer core, rather than a cooler core. As another example, Baumgardner et al. took measurements by penetrating the contrails of a Lear 35 during seven flight tests to evaluate the temperature, water vapor content, and velocity structure of the contrails and compare the measurements to the Aerodyne wake vortex model.[4] They found that the increase in temperature at 500 m from the aircraft exhaust release point is $0.6\,^{\circ}$C, and the increase in water vapor content was 8 ppmv. The measurements verified their temperature models, but showed that their models produced higher than actual values for the water vapor content [24]. Even with these studies, a lack of data still exists due to the variance in the size of aircraft and meteorological conditions.

As the vortex ages, it weakens and decays. Vortex decay has been modeled by several researchers, including Greene, Sarpkaya, and Holzäpfel, with the latest model accounting for conditions such as wind, turbulence, and proximity to the ground [25], [26], [27]. During decay, the core size stays the same, which means that the core pressure increases, causing adiabatic heating, so the temperature differential becomes smaller. In addition, the whole two-vortex system sinks toward the ground as time goes on. This sinking also causes adiabatic heating [21]. At ground level, vortex motion and decay are very dependent on meteorological conditions, as well as the aircraft type and position.

Figure 36 is an image of a vortex created by an aircraft that can be seen due to a smoke injection system [28]. It is apparent from the image that there is a central core of the vortex that is surrounded by swirling air. Aircraft engine exhaust gasses are entrained in the circulating air, but not in the core of the vortex. Contrails also show this phenomenon. The concentrations of exhaust particles in the vortex will be higher than that of the ambient air [19].

The fraction of the exhaust that gets entrained depends on whether the engines are on the wings or on the aircraft body. F. Garnier et al. analyzed the entrainment processes of aircraft engine exhaust within the wake vortex generated by the aircraft using modeling and simulation of a two-engine Airbus 330 and a four-engine Boeing 747. The investigation focused on a thirty-second timescale including the Jet and part of the Vortex phases of the wake vortex. The investigation found that entrainment rate is affected by many parameters including the jet engine location, which affects the early wake in the Jet stage, and the buoyancy effect in the Vortex phase after entrainment has occurred. Once entrained, the exhaust concentration is variable within the contrail due to stretching and distortion, as well as the descent of the vortex [20]. Even at the Dissipation phase, particle concentrations are still highly elevated over background levels of ambient species, but they are now at temperature and pressure conditions of the background atmosphere [19].

Aircraft engine exhaust consists of several species that have identifiable signatures. A report published by the US Environmental Protection Agency (EPA) in 1999, which evaluated the impact of ground-level aircraft emissions generated during takeoff and landing on ten US cities, found that volatile organic compounds (VOCs), CO, NO_x, particulate matter (PM), and SO_2 are the five most significant species emitted from commercial jet aircraft that affect local air quality. During idling and taxiing when engines are operating at low power, VOCs and CO emission rates are highest. The highest rates of NO_x and PM emissions occur during takeoff and climb-out. NO_x emissions rise with an increase in the operational power of the engine, and PM emissions rise due to the incomplete combustion of fuel during those same operational periods. During general combustion of fuel that contains sulfur, SO_2 emissions are created [29]. Another publication lists major species as H_2O, CO_2, CO, and NO_x and minor species as H_2SO_4, and HNO_3. [20].

[4]This study was funded by the NASA High Speed Research Program.

Figure 36. Example of red-colored smoke entrained in wake of aircraft.

Note that the Civil Aviation Authority in the United Kingdom hosts a website that provides access to the Council of the International Civil Aviation Organization's (ICAO) Engine Exhaust Emissions Databank of aircraft engines that have entered production. Engines are sorted by engine manufacturers such as Pratt & Whitney Aircraft Group and General Electric, and each manufacturer has a listing and corresponding datasheet of the various engines in production. The emissions quantified are unburned hydrocarbons (HC), CO, and NO_x [30].

5.2 Dry Wind Shear

In 1986, NASA and the FAA jointly set a timetable for developing and demonstrating a solution to the aviation hazard that was responsible for more than half of the US commercial aviation fatalities of the previous decade: wind shear. Several detection technologies were investigated, including radar, Doppler lidar, and infrared radiometry. During the course of this effort, five NASA - FAA wind shear conferences were held, with the most recent one in September, 1993.

During the wind shear research effort, passive infrared (IR) detection was studied extensively by H. P. Adamson, who founded the Turbulence Prediction System (TPS) company to commercialize his infrared Advance Warning Airborne Sensors (AWAS) [28] [29]. By 1988, Adamson had already planned a development program including extensive in-service evaluation of a radiometric hazard detection system on commercial airline flights, integration with other avionic systems, pilot training, and FAA certification [30]. Much of Adamson's work is described in the proceedings of the NASA - FAA wind shear conferences, and additional information is given in Appendix B of this report.

The term dry wind shear is used here to mean low level wind shear caused by downdrafts, as illustrated in Figure 37 [31]. The physical basis for radiometric detection of such wind shear is the atmosphere's temperature lapse rate, which causes air at higher altitude to be

colder. When the cold air is brought to lower altitudes by a downdraft, a large temperature anomaly is created.

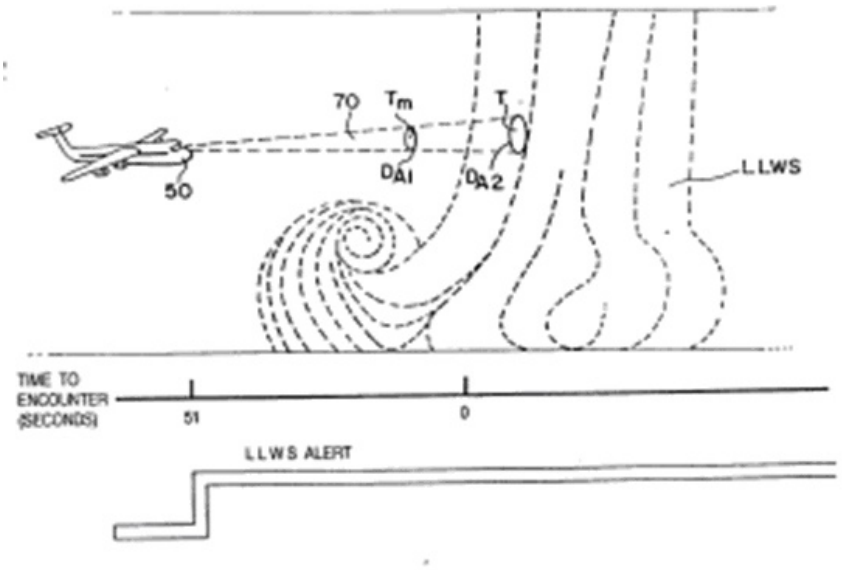

Figure 37. Dry wind shear detection illustration from Adamson.

5.3 Icing

Ice and liquid water have very different optical properties in the infrared molecular "window" region of the spectrum between 10 and 12 μm. As a result, it will be possible to use the FLI instrument to diagnose the existence of supercooled liquid water in clouds (i.e., detect water droplets at sub-freezing temperatures that causes airframe icing) and to discriminate between ice and water on surfaces, such as runways. The temperature of the cloud can be observed as the brightness temperature measured with the FLI near 12 μm, where the cloud emissivity is a maximum, or assumed to be close to the outside air temperature observed independently by the aircraft measurement system. Figures 38 and 39 show that the real (reflection) and imaginary (absorption) parts of the index of refraction for water and ice differ greatly in the range of infrared wavelengths where atmospheric molecular absorption is a minimum (i.e., the molecular absorption "window" between 10 and 12 μm) [32], [33].

In particular, when viewing cloud ice crystals or an icy runway surface, with an FLI, the radiance observed will increase rapidly between 10.5 and 12 μm. Whereas when viewing water droplets or a wet surface, the radiance observed will be relatively constant between 10.5 and 11 μm with the strong increase in radiance occurring between 11 and 12 μm. Thus, it is the small spectral shift in the wavelength at which the radiance emission abruptly increases across the atmospheric "window" region that will allow the FLI to determine whether cloud icing conditions, or a hazardous icy runway, may be encountered by the aircraft. There is a precedent for this type of discrimination; two-band IR radiometers are commercially available for detecting "black ice" on highways (black ice is the term for a thin layer of ice that is difficult to detect visually).

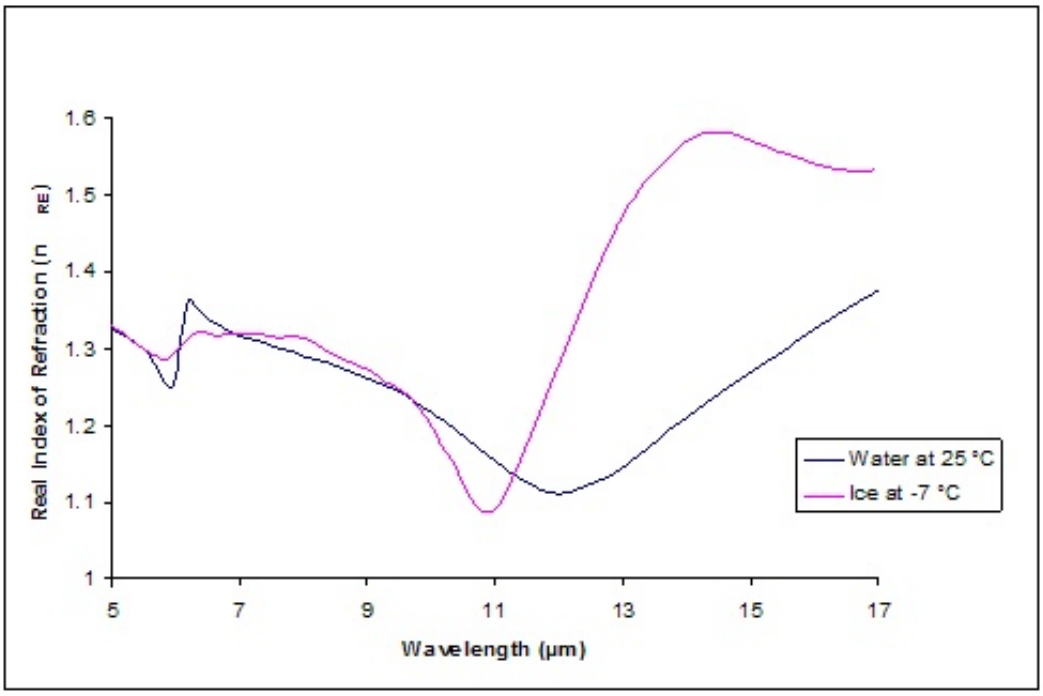

Figure 38. Real index of refraction for water and ice in infrared.

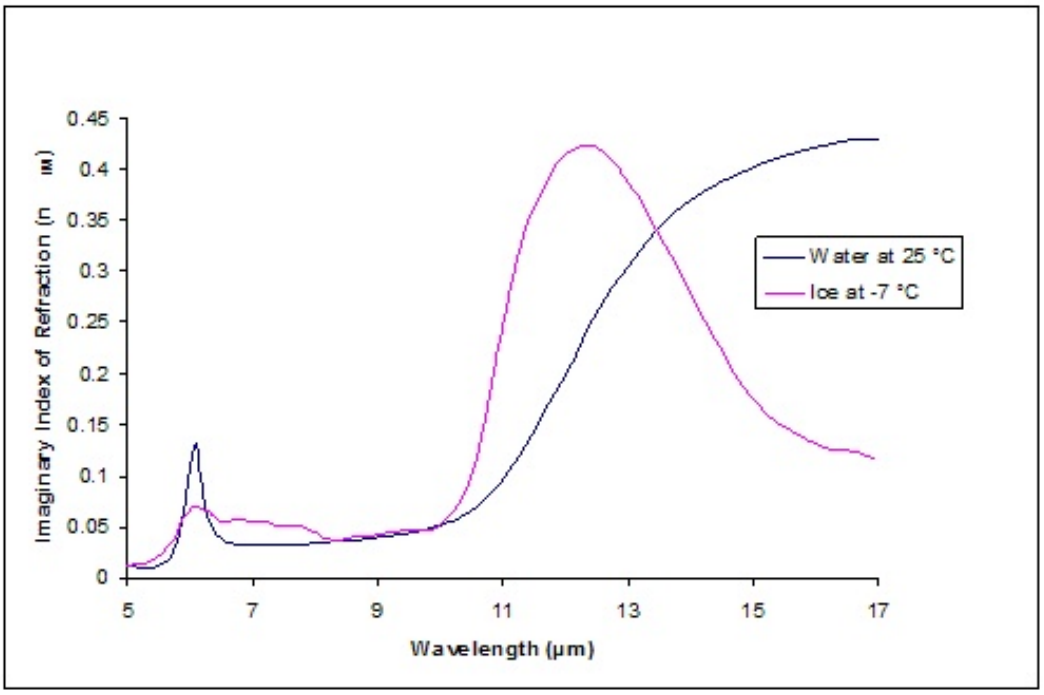

Figure 39. Imaginary index of refraction for water and ice in the infrared.

6 Instrument Design Concept and Specification

Based on the results of the sensitivity studies and characterizations shown in the previous sections of this report, a table of FLI radiance measurement requirements was developed.

Table 2 was developed to guide the development or selection of an instrument to observe various aviation weather hazards in future experimental studies. As discussed previously, there are two techniques for using FLI radiance data to detect turbulence: (1) the use of the CO_2 emission signal produced by the spatial variance of atmospheric temperature associated with the adiabatic heating and cooling resulting from turbulent updraft and downdrafts of the atmosphere, and (2) the use of the water vapor radiance signal produced by the temperature and associated humidity variations associated with turbulent updraft and downdrafts of the atmosphere.

In Table 2, the instrument spectral measurement and noise requirements for the use of these two techniques are quite different. For the temperature turbulence using the partial interferogram approach, the spectral region must contain the CO_2 emission spectral region (690 - 715 cm^{-1}) with a spectral resolution of 0.625 cm^{-1}, or better, in order to resolve the CO_2 emission line spacing of 1.5 cm^{-1}. As discussed earlier, Nyquist sampling of the CO_2 emission line spacing will produce a resonance in the 0.55 to 0.75 cm optical delay region of the measured interferogram. The partial interferogram signal amplitude is related to the degree of temperature variability (i.e., related to turbulence) ahead of the aircraft. For this type of detection, a single field of view/single pixel spatially scanning instrument would suffice, but better detection would certainly be provided by an imaging Fourier Transform Spectrometer (FTS) with a much larger field of view and smaller pixel size than that specified in Table 2.

The water vapor radiance turbulence measurement can be achieved with a lower spectral resolution ($\sim$2.5 cm^{-1}) FTS covering the water vapor emission bands of 1200 - 1600 cm^{-1} and/or 1600 - 2000 cm^{-1}. The reason for the potential of using one or the other of these water vapor bands is due to the fact that their emission characteristics are similar since they represent the longwave and shortwave sides of the 6.3 m band centered at a wavenumber of 1600 cm^{-1}. However, there are some subtle advantages to using one side of the band, versus the other, for the water vapor turbulence signal detection. The shortwave side has the advantage being free from absorption by spectrally overlapping trace gases, such as N_2O and CH_4, which overlap the H_2O lines along the longwave side of the band. On the contrary, because of the rapid fall-off of Planck radiance, for a given scene temperature, with increasing wavenumber (decreasing wavelength), the signal-to-noise ratio of an FTS will naturally be higher for measurements along the longwave side of the band, the degree of which is dependent upon the high wavelength cut-off of the detector used. In any case, the choice of the band to be used will depend upon the ultimate measurement objectives for the FLI, which will determine the total measurement spectral range, and the properties of the particular optical elements and detectors available for the development of an FLI instrument.

The volcanic ash detection requirements are similar to those for water vapor radiance turbulence, but the noise requirement is less stringent as a result of the aerosol being a much stronger absorber/emitter than gaseous water vapor. The band to be used for volcanic ash detection is extended to 1400 cm^{-1} in order to also observe the volcanic emissions of SO_2, which is a strong absorber and emitter between 1325 and 1375 cm^{-1}.

The three aviation hazards which require an imaging FTS for detection are slant range visibility, icing, and wake turbulence, though the detection of all other aviation hazards would benefit from the use of a spatially scanning imaging spectrometer, rather than a single pixel instrument. For slant range visibility, it has been previously shown in Section 4.5 that effective enhancement can be achieved with a relatively low spectral resolution (i.e., 2.5 cm^{-1}) instrument operating in the thermal "window" (i.e., 800 - 1200 cm^{-1}) region of

Table 2. FLI RADIANCE MEASUREMENT REQUIREMENTS

Measurement Specification	Aircraft Hazard					
	Turbulence (T)	Turbulence (T/H_2O)	Volcanic Ash	Slant Range Visibility	Wake Turbulence	Icing
	Technique					
	CO_2 emission Partial Interferogram	Water Vapor Radiance Variability	"Window" Spectral Signature	"Window" Imagery	Water Vapor Radiance Imagery	"Window" Imagery
Spectral Range (cm^{-1})	≤690 - ≥715	1200-1600 and/or 1600-2000	800-1400	800-1200	700-1600	1000-1200
Spectral Range (μm)	14.0-14.5	6.3-8.3 and/or 5-6.3	7.1-12.5	8.3-12.5	6.3-14.3	10-12.5
Spectral Resolution (cm^{-1})	≤0.625	≤2.5	≤2.5	≤2.5	≤2.5	≤2.5
Field of View (mrad)	≥50 (500m@ 10km)	≥50 (500m@ 10km)	≥50 (500m@ 10km)	≥500 (500m @1km)	≥500 (500m@ 1km)	≥500 (500m@ 1km)
Pixel Resolution (mrad)	≤50 (500m@ 10km)	≤50 (500m@ 10km)	≤50 (500m@ 10km)	≤0.1 (1.0m@ 1km)	≤0.1 (1.0m@ 1km)	≤0.1 (1.0m@ 1km)
NEdT @220K Scene T(K)	≤0.1	≤0.1	≤0.3	≤1.0	≤1.0	≤1.0
Dwell Time (sec)	≤2	≤2	≤2	≤0.1	≤0.1	≤0.1
Refresh Rate (frames/sec)	≥0.25	≥0.25	≥0.25	≥10	≥10	≥10

the spectrum, although improvements with higher spectral resolution (e.g., 0.6 cm^{-1}) were shown for very low visibility conditions.

For wake turbulence detection, the spectral range of the imaging FTS must be increased to obtain contributions from carbon dioxide and water vapor since it is the spatial structure of these emissions which delineate the temperature and water vapor spiral patterns associated with the wake vortices produced by an aircraft. The field of view needs to be relatively large to capture any wake, which might affect an aircraft on takeoff, landing, or in-flight. The large field of view, coupled with the very small pixel size (i.e., high spatial resolution) drives the requirement towards a fairly large focal plane array (e.g., $\sim$ 500 x 500 pixels) imaging device. A relatively high image refresh rate is required to enable expanded spatial coverage by stepping the instrument's telescope or an associated scene scan mirror, while at the same time providing near continuous imagery at high spatial resolution of the obstacle as the aircraft moves closer to the scene (i.e., the runway during landing or a wake vortex during takeoff or in-flight).

Although this measurement capability is challenging given the current state of the art, there are instruments which have the spectral imaging capability sufficient for experimentally demonstrating the concept. Also, the array size and associated field-of-view requirement could be relaxed by increasing the spatial stepping rate of the telescope or scene scan mirror of the imaging FTS. Detailed trade studies need to be performed by potential instrument manufacturers in order to optimize the FLI design. Such engineering studies are beyond the scope of the current theoretical study effort.

7 Future Research Needs

The sensitivity and characterization studies reported here addressed the phenomenology that supports detection by the FLI, in other words, which airborne hazards may be detectable, and how. The simulations revealed detectable signatures in both the interferogram and spectral domains for temperature anomalies, and detectable spectral signatures for humidity anomalies caused by CAT and wind shear. A literature search on wake vortex properties suggested that an FLI will be able to provide images of vortices. A simulation of multi-band imaging in low slant-range visibility conditions illustrated the potential of the FLI to provide essentially unobscured IR images of runway scenes as viewed from the air during an approach. In addition, the ability of an FLI to distinguish volcanic ash clouds from water and ice clouds was verified, and its ability to distinguish ice from liquid water on surfaces such as runways was investigated. Techniques for determining the range (and hence warning time) to hazards were also demonstrated.

The results of these studies are promising, but they are only a first step in assessing the full potential of an FLI to serve as a multi-hazard airborne sensor. Investigators must also develop a means to estimate the intensities of the hazards posed to an aircraft; develop instrument requirements for a commercial hazard warning sensor[5]; develop robust algorithms to relate hazard levels to sensor readings; and perform validation tests. In order to accomplish these goals, further research is required in four general categories including ground-based measurements, airborne measurements, further sensitivity studies, and simulations.

7.1 Ground Measurements

Ground-based measurements can be performed at lower cost than airborne measurements and may be achievable for several hazards including mountain waves (turbulence induced by

[5]Discussions have been held with two companies that have either a commercial or prototype system that could be used in future field tests. Information regarding these systems is included in Appendix C.

orography), wake vortices, low slant-range visibility, and volcanic ash. Mountain waves offer an excellent opportunity for ground-based measurements of turbulence, because they are predictable and fairly well understood. Imagery of mountain waves with an FLI may provide a good first comparison with the sensitivity studies. Imagery in low visibility conditions can be collected on any scenario where terrain or an elevated structure provides a slant viewing path to the earth, in a location where fog and haze occur. An airport would be the ideal location, and a control tower may provide the viewing platform. The airport weather data would document the weather conditions, and visible-light imagery would provide additional characterization.

Data has been collected on volcanic ash and SO_2 in the past, but no one has ever acquired multi-band IR imagery of a volcanic ash cloud viewed horizontally, as it would be viewed in flight. Such a view may be achievable with the sensor located on an adjacent mountain. This scenario is unpredictable because it is dependent on having an active volcano with an accessible adjacent mountain, but researchers should be prepared for it in case such an opportunity arises.

7.2 Flight Measurements

The number of atmospheric data sets available for the sensitivity studies reported here was very limited, and details of the atmospheric structures and fields associated with hazards remains largely unknown. For this reason, there is no substitute for future flight tests. They will be essential for establishing sensor performance. However, such flights must include truth data that can be used in the simulation environment described below to provide a physical understanding of the infrared signatures and to identify any issues. In order to keep the cost of airborne tests affordable, it may be necessary to align with larger projects. There are several ongoing research projects that may offer candidate airborne platforms along with relevant truth data, such as:

- The NOAA G-IV is operated in a Winter Storm series during which truth data is acquired with drop sondes.
- The NOAA HIAPER is sometimes flown with a wind-scanning Lidar.
- The DLR Falcon is flown with a wind-scanning Lidar.
- A UK Met aircraft located in Iceland is flown in turbulence studies.

7.3 Further Sensitivity Studies

The pilot studies reported here have successfully demonstrated that the spectral radiance measurements by an FLI mounted on an aircraft would be able to sense radiometric signatures associated with aviation weather hazards to safe flight. It has also been shown that, for the case of enhancing slant range visibility, Eigenvector (EOF) regression is a powerful method for transforming FLI spectra into useful physical products that can be used by the flight crew to insure safe flight. It is likewise expected that EOF regression can also be used to enable rapid and accurate predictions of other aviation safety hazards such as turbulence, wind shear, volcanic ash, wake turbulence, and icing.

The advantage of using EOF regression is that it enables the entire spectrum of information content to be used for the sensing of these phenomena, thereby multiplexing the emission signals from all the atmospheric gases of interest as well as the emission signals from clouds and aerosols. For example, it was shown that for turbulence the signal comes from the temperature and water vapor contribution to the emitted radiances in two different portions of the emission spectrum (i.e., the CO_2 emission region near 15 m and the H_2O

emission region near 6.3 μm). Furthermore, for the case of turbulence, the signal is relatively small so that a very high signal-to-noise ratio of the measurement variable is required. The advantage of the use of EOF regression is that by extracting the information content from the entire spectrum, the signatures of turbulence inherent in the large number (i.e., 1000 or more) of FLI spectral radiance measurements, are combined into a small number (i.e., 2 - 4) of EOF predictors. As a result, the signal-to-noise ratio of the FLI detection system is enhanced by an order of magnitude, or more, by using EOF regression to retrieve the geophysical characteristics of the otherwise small radiance turbulence signal. A similar signal-to-noise advantage will be gained for the detection of all other weather related hazards as well. Thus, the important next modeling step in the FLI applications research is to develop and apply the EOF regression technique to predicting the intensity, distance, and time to encounter for turbulence, volcanic aerosol, wake turbulence, and icing. The technique should be exercised for a wide variety of atmospheric situations to demonstrate the robustness of the algorithm.

7.4 Simulation Environment

It is not feasible to fly a sensor in all possible conditions, so simulations generally play a crucial role in characterizing phenomena and developing hazard detection algorithms and estimates of metrics such as probability of detection and false alarm rate. In addition, all flight and ground test data (both sensor data and truth data) should be processed using the same tools as those used for simulated data. Consistency in data processing will aid in understanding the phenomena and the mechanisms that create aircraft hazards. It will also help in understanding anomalies or inconsistencies between test data and simulations. Knowledge gained in the comparison of test data and simulations will both help validate the simulations and guide the planning of future flight tests.

8 Conclusions

In the study reported here, remote sensing techniques developed for space-based sensors were applied to aviation hazard detection problems in order to assess the feasibility of using such techniques in airborne sensors. Sensitivity studies were performed on clear air turbulence, volcanic ash clouds, and slant range visibility. Characterization studies were conducted on wake vortices, dry wind shear, and icing to determine if future sensitivity studies were warranted. Sensitivity studies were conducted using a limited set of temperature, wind, and humidity fields. The studies were performed spectrally with high enough resolution to resolve individual spectral lines of molecules such as CO_2, so as to support the use of interferometric sensors such as the FLI. The simulations were performed for single lines of sight from the sensor to/through the hazards.

CAT and Dry Wind Shear. Sensitivity studies for CAT detection included two techniques: sensing temperature fluctuations using the 650 - 780 cm^{-1} CO_2 band and sensing water vapor fluctuations in the 1300 - 1600 cm^{-1} region. The simulations revealed detectable signatures in both the interferogram and spectral domains for the CO_2 temperature technique at flight altitudes, although the maximum detection range appears to be about 5 km (assuming an instrument resolution of 0.3 K), which is not as large as early investigators have claimed, but humidity anomalies in the one case for which data exists were detectable from 30 km, or with a warning time of approximately 2 min, assuming a lower instrument sensitivity of 1.0 K. Wind shear near the ground is associated with the downward motion of cooler air from higher altitudes, and the anomalously low air temperatures should be easily detectable with an FLI during a landing approach.

Volcanic Ash. The ability of an IR imager to distinguish volcanic ash clouds from

water and ice clouds was verified in the 800 - 1100 cm^{-1} region, using an ash optical depth spectrum obtained from the literature. The optical properties of volcanic ash produce a large signature in the 8 - 12 μm window region, thereby making ash detection possible with the FLI.

Low Visibility. A simulation of multi-band imaging in low slant-range visibility conditions illustrated the potential of the FLI to provide essentially unobscured IR images of runway scenes as viewed from the air during an approach. This capability will give pilots a clear view of runways even when an obscurant such as a ground fog is present, and it will provide high quality images to support automated detection of airborne and ground obstacles or other hazards.

Wake Vortices. Typical wake vortex properties obtained from a literature search included the core temperature as well as the concentrations of exhaust gas constituents (including water vapor) that become entrained in the vortex. Vortex core temperatures have been measured to be several degrees below ambient temperature and this temperature difference should be detectable, which suggests that an FLI might provide real-time imagery of the motion and evolution of wake vortices. The entrained gasses, including water vapor, could provide additional means of detection with an FLI. Detection of wake vortices by FLI techniques is possibly the most challenging application considered due to the relatively small size of the phenomena and the geometry of the problem which would have the FLI looking down at a scene with ground, runway, and other objects as background during landing, the phase of flight that would be of most interest.

Icing. The optical properties of liquid water and ice are quite different in the spectral regions where the FLI will operate. This fact will give the FLI a capability to distinguish ice from liquid water on surfaces such as runways. In addition, the FLI may be able to detect icing conditions ahead of an aircraft during flight, by discriminating supercooled liquid water drops from ice crystals.

The sensitivity and characterization studies reported here addressed the phenomenology that supports detection by an FLI. Techniques for determining the range, and hence warning time, were demonstrated for several of the hazards, and a table of research instrument parameters was developed for investigating all of the hazards listed above. This work supports the feasibility of detecting multiple hazards with an FLI airborne sensor, providing enhancements to aviation safety. Future research should also address the additional information available in two dimensional images. This could be of particular value for turbulence and wake vortex detection, and is essential for enhanced imaging applications. Once feasibility of detection and determination of hazard levels has been established, more attention should be focused on issues including probability of detection, false alarm rates, efficient real-time processing algorithms, generation of displays, and instrument considerations such as hardware specifications required for selected hazards and sensitivity to vibrations.

FLI technology shows promise for a new class of airborne sensors; however, further research must be performed to develop a means to estimate the intensities of the hazards posed to an aircraft and to develop robust algorithms to relate hazard levels to sensor readings. In addition, validation tests need to be performed with a prototype system. In order to accomplish these goals, additional research should include ground-based measurements, airborne measurements, further sensitivity studies, and simulations. Additional possible applications not addressed in this study should be investigated. These include detection of runway contamination, observations of temperature and water vapor for use in weather models, and detection of pollution or other aerosols. Downward-looking atmospheric profiling for observations of quantities such as water vapor, temperature, and turbulence also merits consideration.

References

1. Gimmestad, G.; West, L.; Smith, W.; Kireev, S.; Liu, X.; Schaffner, P.; and Murray, J.: *Airborne Forward Looking Interferometer Turbulence Investigation*. 45th AIAA Aerospace Sciences Meeting and Exhibit, no. AIAA-2007-78, Reno, Nevada, Jan. 8-11, 2007.

2. Guffanti, M.; and Miller, E.: *Reducing the Threat to Aviation from Airborne Volcanic Ash*. 55th Annual International Air Safety Seminar, 2002.

3. Gimmestad, G.; Papanicolopoulos, C.; Richards, M.; Sherman, D.; and West, L.: *Feasibility Study of Radiometry for Airborne Detection of Aviation Hazards*. NASA Contractor Report CR-2001-210855, June 2001.

4. Oppenheimer, C.; Francis, P.; Burton, M.; Maciejewski, A.; and Boardman, L.: *Remote Measurement of Volcanic Gases by Fourier Transform Infrared Spectroscopy*. Applied Physics B: Lasers and Optics, vol. 67, 1998, pp. 505 – 515.

5. Clough, S.; Iacono, M.; and Moncet, J.: *Line-by-line calculation of atmospheric fluxes and cooling rates: Application to water vapor*. Journal of Geophysical Research, vol. 97, 1992, pp. 15761–15785.

6. Clough, S. A.; and Iacono, M. J.: *Line-by-line calculation of atmospheric fluxes and cooling rates, 2, Application to carbon dioxide, ozone, methane, nitrous oxide, and the halocarbons*. Journal of Geophysical Research, vol. 100, 1995, pp. 16,519–16,535.

7. Weaver, E. A.; Ehernberger, L. J.; Gary, B. L.; Kurkowski, R. L.; Kuhn, P. M.; and Stearns, L. P.: *The 1979 Clear Air Turbulence Flight Test Program*. Proc. Fourth Ann. Workshop on Meteorol. and Environ. Inputs to Aviation Systems, 1981.

8. Simkin, T.: *Volcanoes: Their Occurrence and Geography*. Proceedings of the First International Symposium on Volcanic Ash and Aviation Safety: U.S. Geological Survey Bulletin 2047, 1994.

9. Searcy, C.; Dean, K.; and Stringer, W.: *PUFF: A Lagrangian Trajectory Volcanic Ash Tracking Model*. Journal of Volcanology and Geothermal Research, vol. 80, 1998, pp. 1–16.

10. K.R. Papp, K. D.; and Dehn, J.: *Predicting regions susceptible to high concentrations of airborne volcanic ash in the North Pacific region*. Journal of Volcanology and Geothermal Research, vol. 148, 2005, pp. 295–314.

11. Smith, W. L.; and Platt, C. M. R.: *Comparison of Satellite-Deduced Cloud Heights with Indications from Radiosonde and Ground-Based Laser Measurements*. Journal of Applied Meteorology, vol. 17, no. 12, 1978, pp. 1796–1802.

12. Rodgers, C. D.: *Inverse Methods for Atmospheric Sounding : Theory and Practice*. World Scientific Publishing Company, 2000.

13. Smith, W.; and Woolf, H.: *The Use of Eigenvectors of Statistical Covariance Matrices for Interpreting Satellite Sounding Radiometer Observations*. Journal of the Atmospheric Sciences, vol. 33, no. 7, 1976, pp. 1127–1140.

14. Smith, W. L.; Zhou, D. K.; Larar, A. M.; Mango, S. A.; Howell, H. B.; Knuteson, R. O.; Revercomb, H. E.; and Smith, W. L.: *The NPOESS Airborne Sounding Testbed Interferometer Remotely Sensed Surface and Atmospheric Conditions during CLAMS*. Journal of the Atmospheric Sciences, vol. 62, no. 4, 2005, pp. 1118–1134.

15. Huang, H.-L.; and Antonelli, P.: *Application of Principal Component Analysis to High-Resolution Infrared Measurement Compression and Retrieval*. Journal of Applied Meteorology, vol. 40, no. 3, 2001, pp. 365–388.

16. Calbet, X.; and Schlssel, P.: *Technical note: analytical estimation of the optimal parameters for the EOF retrievals of the IASI Level 2 Product Processing Facility and its application using AIRS and ECMWF data*. Atmospheric Chemistry and Physics, vol. 6, no. 3, 2006, pp. 831–846.

17. Hinton, D. A.: *An Aircraft Vortex Spacing System (AVOSS) For Dynamical Wake Vortex Spacing Criteria*. AGARD 78th Fluid Dynamics Panel Meeting and Symposium on The Characterization & Modification of Wakes from Lifting Vehicles in Fluids, 1996.

18. Paugam, R.; Cariolle, D.; Paoli, R.; and Cuenot, B.: *Simulations of Aircraft Plumes Using a Meso Scale Code*. CERFACS Conference, 2006.

19. Karol, I.; Kelder, H.; Kirchhoff, V.; Ogawa, T.; Ross, M.; and Wennberg, P.: *Aviation and the Global Atmosphere*, Intergovernmental Panel on Climate Change, 2. Impacts of Aircraft Emissions on Atmospheric Ozone. 2000. URL `http://www.grida.no/climate/ipcc/aviation/022.htm` .

20. Garnier, F.; Brunet, S.; and Jacquin, L.: *Modelling exhaust plume mixing in the near field of an aircraft*. Annales Geophysicae, vol. 15, no. 11, February 1997, pp. 1468–1477.

21. Proctor, F.: Researcher, NASA Langley Research Center, Personal Communication, November 2006.

22. Hallock, J.; Osgood, S.; and Konopka, J.: *Wake Vortex Effects on Parallel Runway Operations*. 1st Aerospace Sciences Meeting and Exhibit, 2003.

23. Adamson, H.; and Morrison, C.: *Infrared Airborne and Ground Detection of Wake Vortices*. Proceedings of the Aircraft Wake Vortices Conference,, J. N. Hallock, ed., no. SD-92-1 in DOT/FAA, 1991.

24. Baumgardner, D.; Miake-Lye, R. C.; Anderson, M. R.; and Brown, R. C.: *An evaluation of the temperature, water vapor, and vertical velocity structure of aircraft contrails*. Journal of Geophysical Research, vol. 103, no. 8, 1998, pp. 8727 – 8736.

25. Greene, G.: *An approximate model of vortex decay in the atmosphere*. 12th Atmospheric Flight Mechanics Conference, 1985.

26. Sarpkaya, T.: *A new model for vortex decay in the atmosphere*. 37th Aerospace Sciences Meeting and Exhibit, 1999.

27. Holzpfel, F.: *Probabilistic Two-Phase Wake Vortex Decay and Transport Model*. Journal of Aircraft, vol. 40, 2003, pp. 323–331.

28. Chambers, J. R.: *Concept to Reality Wake Vortex Hazard*. Online report, NASA LaRC, 2003. URL `http://oea.larc.nasa.gov/PAIS/Concept2Reality/wake_vortex.html` .

29. *Evaluation of Air Pollutant Emissions from Subsonic Commercial Jet Aircraft*. Final Report EPA420-R-99-013, US Environmental Protection Agency, Engine Programs and Compliance Division, April 1999. URL `http://www.epa.gov/otaq/regs/nonroad/aviation/r99013.pdf` .

30. *Aircraft Engine Emissions: ICAO Engine Emissions Databank*. Online database, UK Civil Aviation Authority, Aircraft Environmental Section, June 2005. URL `http://www.caa.co.uk/default.aspx?catid=702&pagetype=90` .

31. Adamson, H. P.: *Method for producing a warning of the existence of low-level wind shear and aircraftborne system for performing same*. US Patent 4,965,572, 1990.

32. Warren, S. G.: *Optical constants of ice from the ultraviolet to the microwave*. Applied Optics, vol. 23, 1984, pp. 1206–1225.

33. G. M. Hale, M. R. Q.: *Optical constants of water in the 200 nm to 200 m wavelength region*. Applied Optics, vol. 12, 1973, pp. 555–563.

34. Adamson, H. P.: *Apparatus detecting air disturbance created by low level wind shear*. US Patent 4,342,912, 1982.

35. Adamson, H. P.: *Radiometer apparatus for air disturbance detection*. US Patent 4,427,306, 1984.

36. Kuhn, P. M.: *Method and apparatus for detecting clear air turbulences*. US Patent 4,266,130, 1981.

37. Delnore, V. E., ed.: *Airborne Windshear Detection and Warning Systems. Fifth and Final Combined Manufacturers' and Technologists' Conference, part 1*, NASA, July 1994. Conference held in Hampton, VA, 28-30 Sep. 1993 cosponsored by FAA.

38. Adamson, H. P.: *Development of the advance warning airborne system (AWAS)*. Airborne Wind Shear Detection and Warning Systems. Fourth Combined Manufacturers' and Technologists' Conference, part 2, no. 10105 in NASA CP, 1992.

39. Telops: *Accelerating Innovation in Optronics*. 2000. URL `http://www.telops.com` .

40. Chamberlain, M.: Telops Employee, Personal Communication, October 2006.

41. Crain, D.: I.T.T. Employee, Personal Communication, October 2006.

Appendix A

Workshop and Results

The Airborne Radiometric Detection of Aviation Hazards Workshop was held 14-15 August 2006 at the National Institute of Aerospace (NIA) in Hampton, VA. The goals of the workshop were to review the current status of research in this technical area, to assess the resources that are available for further work, and to familiarize interested participants with the research program. The workshop had 30 attendees from government, industry, and academia, with 11 technical presentations and additional discussions. The Workshop agenda and presentations are available online at a website hosted by NIA:

http://www.nianet.org/workshops/ardah06.php.

The Workshop resulted in lists of resources and other parties interested in participating in future research efforts. Simulation resources are available at Hampton University, the University of Wisconsin-Madison, and NCAR. Measurement resources will be provided by industry. Possibilities for equipment include Telops, Bomem, ITT, and Dr. Fred Prata's multi-spectral imager. Additional parties who will be included in the research as it moves forward are airline representatives, including Delta and Northwest Airlines, pilots, the Federal Aviation Administration (FAA), and airframe manufacturers, such as Boeing. Hampton University's modeling capabilities lie in single line-of-sight radiative transfer. Another potential resource is the University of Wisconsin-Madison SSEC/CIMSS (Space Science and Engineering Center/Cooperative Institute for Meteorological Satellite Studies) group, which has extensive modeling capabilities that include a 4-D simulation and visualization capability that can be used to generate modeled images of water and ice clouds and volcanic ash. ITT also has modeling capabilities that include simulation and visualization.

NCAR is the leader in turbulence research and forecasting. They have a broad database of information that can be used in future modeling efforts. Some data has already been furnished to HU by NCAR for the purposes of this reported feasibility study.

Telops has a lightweight and compact hyperspectral imaging sensor using FT-IR technology called FIRST. Other sensor technology options include Prata's multispectral imager that is currently configured for volcanic ash detection, ITT's interferometric imager, and Bomem's lamellar grating Fourier Transform Spectrometer system. Prata's imager is a non-commercial product that is configured for volcanic ash and SO_2 detection. It has been tested on the ground at several volcanoes. Each system has its own characteristics, and more than one system may be warranted for ground/flight tests, keeping in mind physical and budgetary limitations.

Other interested parties include airline representative from Delta and Northwest. Northwest Airlines was unable to attend the Workshop, but would like to participate in the research as it moves forward. Delta Airlines stated that their interest in CAT is mainly economic. Delta, as an example of a commercial airline that would be interested in mounting the sensor that results from the study into their fleet, understands the relevant needs and the business case for such a system. Lastly, Delta may offer a low-cost platform for evaluation of a commercial sensor.

Appendix B

Additional Information on Low Level Wind Shear studies by Adamson

Adamson has described airborne IR hazard sensor systems in three US patents [34], [35], [31]. The first device was a mechanically chopped single-band radiometer operating in the 20-40 μm region. The detector was not cooled. Automatic calibration was achieved by periodically inserting a paddle heated to 42 °C into the path of the received radiation. Much of the patent is concerned with an analog signal processing scheme to enhance the signal-to-noise-ratio, but the frequency response and noise figures are not given. An earlier patent by Peter Kuhn is included by reference [36].

Adamson's second device includes multiple bandpass filters on a rotating wheel. The filters span the wavelength ranges 14 - 14.5, 14.5 - 15, 15 - 15.5, and 15.5 - 16 μm. The input radiation was mechanically chopped and the detector was not cooled. The signal processing electronics had a low-pass filter with a cutoff frequency of about 1.6 Hz. No noise figures are given. Again, much of the patent is concerned with an analog signal processing scheme and the patent by Peter Kuhn is again included by reference.

Adamson's third patent describes a sensor based on an IR grating spectrometer, again with built-in calibration. The spectrometer provides a bandpass with adjustable width and center wavelength. A scheme is presented for integrating the radiometer with other sensors in order to combine predictive (radiometer) data with reactive (accelerometer) data, and the severity of the hazard is quantified in terms of the F factor.

Adamson named his sensor the Advance Warning Airborne Sensor (AWAS) and developed three generations of it, known as AWAS I, II, and III. The AWAS sensors pointed straight ahead in the flight direction; they did not scan in angle. During the summer of 1990, AWAS III was installed on a Cessna Citation operated by the University of North Dakota and operated on 66 test flights that included wet microbursts in Orlando, Florida and dry microbursts in Denver, Colorado. Good correspondence was obtained between hazard values predicted by AWAS and data from a Terminal Doppler Weather Radar (TDWR).

During February - June 1991, TPS installed AWAS III sensors with data recorders on three MD-80 aircraft operated by American Airlines, and three more on DC-9 aircraft operated by Northwest Airlines. The sensors recorded data during more than 10,000 hours of commercial flights. One important finding was that the system generated a "nuisance alert" on 20% of the American Airlines flights.

The NASA flight tests were reported by McKissick at the 5th wind shear conference [37]. With funding from a NASA Phase I SBIR grant in 1987, TPS had determined that a passive IR system appeared to be feasible for wind shear detection. Under a Phase II SBIR (1989-1991), AWAS I was flight tested on the NASA 515, and AWAS III was developed.

AWAS III was then flight tested on the NASA 515 at Orlando and Denver in 1991 and numerous changes were made, including improvements in the optics and periscope, a new method for compensating lapse rate effects, and filtering of the hazard indices. The hazard indices were applicable for approach speeds only (approximately 140 knots) and NASA's flight tests were conducted at much higher speeds, so an approximation was developed by NASA personnel to transform measured F-factors for comparisons with the AWAS III hazard indices. The improved AWAS III was flight tested in 1992, again on the NASA 515 at Orlando and Denver.

NASA's conclusions from the AWAS III flight tests were that the sensor did provide a predictive capability for wind shear with 11 to 55 seconds warning time, but that the hazard indices were not reliable predictors of measured F-factors, and so the development

of a reliable hazard index was incomplete. At the 4th wind shear conference, Adamson discussed the reasons why the NASA flight test results were not as promising as the previous results [38]. He stated that the NASA test had the following problems:

1) NASA personnel manually overrode the AWAS automatic mode selection routine (TPS personnel were not on the flights). 2) The location and method of mounting the IR window assembly impaired the sensor's line of sight and led to accelerated mirror damage that was not seen on previous flights, as well as problems with rain. 3) Airspeeds during the tests were in excess of the normal landing and takeoff speeds that the AWAS algorithms were developed for, and NASA's approximations for adjusting the test data to compensate for this problem were inadequate.

In a question-and-answer session after Adamson's talk, the consensus of the NASA participants appeared to be that IR radiometric technology was not sufficiently robust to provide both acceptable detection and false alarm rate performance.

NASA's previous conclusions about radiometry pertain to the AWAS series of sensors, which were all single-line-of-sight radiometers pointed along the direction of flight. The temperature resolution of the AWAS radiometers was not given in the patents nor in the conference proceedings, but it is perhaps on the order of $\pm$ 1 °C due to the use of un-cooled detectors. The spectral resolution of AWAS was not given either, but the radiometer with multiple filters on a wheel used 0.5 μm bandwidths.

In contrast, the FLI investigated in the study reported here is an imaging system that will provide information on the structure of the disturbed air ahead of the aircraft, with a temperature resolution on the order of 0.1 C and spectral resolution on the order of 0.5 cm^{-1} (0.005 μm at 10 μm wavelength), which is sufficient to resolve individual lines in the CO_2 spectrum and the windows between them. The combination of high spatial, spectral, and temperature resolution will provide a wealth of detailed data that has never before been obtainable, and that data is expected to enable much more sophisticated algorithms with high detection rates and low false alarm rates.

Appendix C

Further Discussion of Candidate Sensor Technologies

Discussions have been held with the Telops Corporation in Quebec, Canada and ITT Industries Space Systems Division in Fort Wayne, IN. Telops produces the FIRST instrument, one of the candidate imaging interferometers for experimentally validating the FLI aviation hazard phenomena by the detection techniques outlined in the report. ITT has a prototype hyperspectral testbed system, originally developed for the Hyperspectral Environmental Suite (HES). Each of the companies' instruments is discussed in more detail below.

C.1 Telops

Telops' FIRST sensor is shown in figure C1 [39]. FIRST is a lightweight and compact hyperspectral imaging sensor using FT-IR technology. It provides unparalleled spatial and spectral information about the IR targets under measurement. With its integrated calibration system and electronics, FIRST can be used in a standalone (and unmanned) configuration for over 24 hrs. The standard hardware interfaces make the sensor easy to use.

Figure C1. Telops' FIRST Imager.

The sensor specifications are nearly ideal for the purposes of the planned data collection efforts if the wavelength range can be expanded to include 12-15 microns. The system is compact and portable for field use and has a wide field-of-view and high spatial resolution, a variable spectral resolution down to $0.25cm^{-1}$, flexible data products utilizing real-time onboard digital processing, integrated calibration targets that ensure accurate measurements, simultaneous visible imaging, and an easy-to-use FT Pro data management suite. Table C1 lists the specifications of the FIRST imager [39].

However, the system operates in the $7.8 - 11.6\mu m$ range OR the $2 - 5.5\mu m$ range. One system cannot operate in both bands. Telops owns a long-wave unit for demonstration purposes only. Telops does not have a mid-wave unit in hand, but they have two customers who own mid-wave systems. These customers are the University of Madrid and Air Force Institute of Technology (AFIT) in Dayton, OH.

Making modifications to the system is not trivial. Extending the long-wave range below

Table C1. TELOPS' FIRST IMAGER SPECIFICATIONS

	Unit	Specification
Spectral Band	μm	8-11 (LW) 3-5 (MW)
Number of Pixels		320 x 256
Spectral Resolution	cm^{-1}	0.25 - 150
IFOV	mrad	0.35
Communication		Ethernet
Data Transfer		Cameralink
Acquisition Software		FT Pro
Detector Cooling		Closed Cycle
Power Source		28 V (DC) or 129 V (AC)
Weight	lbs	≤ 60

$7.8\mu m$ means changing a cold filter (this modification implies a custom instrument - there is no access to the cold filter). Perhaps the system can be extended to $6.5\mu m$, but the data will be noisier. To be beneficial to a follow-on project, the resolution would have to be on the order of a wavenumber. FIRST can achieve 1/4 wavenumber or higher resolution. The applications also require at least one frame per second (fps). The long-wave FIRST can achieve one fps, but only with a reduced image size. The mid-wave version has a higher frame rate [40].

Telops has conducted several tests and data collection efforts with their system. Enhanced visibility work has not been performed with this system, nor have flight tests.

C.2 ITT

ITT has developed a lab prototype hyperspectral system with internal research and development (IRAD) funding. The prototype was developed as part of a hyperspectral testbed program for Hyperspectral Environmental Suite (HES). HES has been canceled, freeing up the laboratory prototype for other uses, which potentially includes detection of aviation hazards[C1].

Currently at ITT, further IRAD funding is being sought for calendar year 2007 to package the lab prototype system. Hampton University has provided specifications to ITT for the proposed aviation hazard detection system to support the ITT IRAD proposal. By fall of 2007 through IRAD funding, the lab prototype may be turned into a system that could be used in the field and that meets the required specifications for the aviation hazard detection project. The current system operates from 3.5 to 16 μm with a 0.5 to 1 wavenumber resolution. The whole imaging array is populated, and the data system is a computer cluster. The field of regard is somewhat small, and a telescope is needed. The telescope addition would also be funded under the IRAD. Currently, the system is three separate arrays. Each array has been procured and demonstrated individually. The system was designed to operate all three at the same time, and the ITT IRAD funding would provide the means to do the integration [41].

[C1] Glen Davis at ITT led the development effort for the HES testbed.

Appendix D

NCAR Final Report for Airborne Forward-Looking Interferometer Turbulence Investigation

Under NIA TASK ORDER NUMBER 6083-UCAR Task

Monitors: Dr. David Peake (NIA), Dr. Melody Avery (NASA)

9/29/06-3/15/07

Prepared By: Larry Cornman UCAR/NCAR

3/15/07

Airborne Forward-Looking Interferometer Turbulence Investigation

Larry B. Cornman
National Center for Atmospheric Research
Boulder, CO.

D.1 Introduction

Turbulence is the leading cause of non-fatal accidents for Parts 121, 135, and 91 air traffic. In addition, the costs to the major US commercial air carriers are well over $100 million dollars per year. NASA and the FAA have sponsored very successful programs to detect and forecast turbulence. NASA has focused on forward-looking airborne sensors, such as Doppler radars and lidars - and is currently is supporting a program to investigate the feasibility of using a passive infrared sensor to detect turbulence ahead of an aircraft.

This report is divided into two parts: Part A discusses the work done investigating methodologies for measuring turbulence from an airborne IR interferometer; Part B provides an overview of the data sets that were delivered to Hampton University in support of their simulation activities.

Part A

D.2 Theory

It should be noted that the material presented below reflects preliminary work. A number of assumptions are made, which need to be supported. Furthermore, the equations need to be checked for errors, as well as further simplifications where possible. Nevertheless, it does present the basic concepts and methodologies.

Following on the methods used in the airborne radar problem, the concept is to derive equations that relate the statistics of the atmospheric turbulence (e.g., temperature field) to those of the sensor measurements (e.g., the irradiances). Two approaches can be considered: (1) the turbulent temperature field is homogeneous and extends along the whole measurement path, and (2) the temperature field is laminar, excepting for a "patch" of turbulence at a certain distance from the sensor.

Start with the Radiative Transfer Equation for a gas in thermal equilibrium, with negligible scattering, and the measurement is made along the direction x:

$$\frac{dI(x)}{dx} = h(x)[W_B(x) - I(x)] \tag{D1}$$

where $I(x)$ is the irradiance (or intensity), $W_B(x)$ is the Planck function and $h(x)$ is the absorption coefficient. It should be noted that the frequency dependence of each of these terms is being suppressed for notational clarity. Equation (D1) is a linear first order differential equation of the form,

$$\frac{dy}{dx} + a(x)y(x) = b(x) \tag{D2}$$

With the solution,

$$y(x) = \exp\left[-\int a(x)dx\right] \int b(x) \exp\left[-\int a(x')dx'\right] dx + const. \tag{D3}$$

Applying this to equation (D1), gives:

$$I(L) - I(0) = \exp\left[-\int_0^L h(x)dx\right] \int_0^L h(x) W_B(x) \exp\left[-\int_x^L h(x')dx'\right] dx \tag{D4}$$

Assume that $I(L)$ is zero, i.e., there is no radiation coming from $x > L$. Further, note that

$$\int_x^L h(x')dx' = \int_0^L - \int_0^x h(x')dx' \tag{D5}$$

and since the integral over $[0, L]$ is independent of x, it can be taken outside the integral over x, which gives

$$I(0) = -\int_0^L h(x) W_B(x) \exp\left[-\int_0^x h(x')dx'\right] dx \tag{D6}$$

This is a well-known result in the literature (e.g., Tourin and Krakow, 1965), the full derivation was given above to fill in the steps. Let $\beta(x) = \int_0^x k(x')dx'$, the so-called optical depth. Note that

$$\frac{d\beta(x)}{dx} = h(x) \tag{D7}$$

and hence

$$\frac{d}{dx} \exp\left[-\int_0^x h(x')dx'\right] = -\frac{d\beta(x)}{dx} \exp\left[-\beta(x)\right] \tag{D8}$$

Hence, equation (D6) can be written as

$$I(0) = \int_0^L W_B(x) \exp\left[-\beta(x)\right] \frac{d\beta(x)}{dx} dx = \int_{x=0}^L W_B(x) \exp\left[-\beta(x)\right] d\beta(x) \tag{D9}$$

This is a well-known form given in the literature (e.g., Gautier and Revah, 1975). Another way to write equation (D6) is to let $\alpha(x) = \exp\left[-\beta(x)\right]$, the transmittance. Equation (D9) then becomes

$$I(0) = \int_{x=0}^L W_B(x) \frac{d}{dx} \alpha(x) dx = \int_{x=0}^L W_B(x) d\alpha(x) \tag{D10}$$

It should be noted that some authors use the notation $\tau(x) = \beta(x)$, while others use $\tau(x) = \alpha(x)$, so care should be taken when trying to compare references.

Consider another measurement made at the point, $x = \rho \geq 0$,

$$I(\rho) = -\int_\rho^{L+\rho} h(x) W_B(x) \exp\left[-\int_\rho^{x+\rho} h(x')dx'\right] dx \tag{D11}$$

This means the correlation between $I(0)$ and $I(\rho)$ is

$$\langle I(0) I(\rho) \rangle = C^2 \left\langle \int_0^L \int_\rho^{L+\rho} h(x) h(x') W_B(x) W_B(x') \exp\left[-\int_0^x - \int_\rho^{x'+\rho} h(y)dy\right] dx'dx \right\rangle \tag{D12}$$

There are references that derive results for the mean value of equation (D1) for turbulent conditions. These include: Kabashnikov and G.I. Kemit (1979), Kabashnikov (1985), and Kabashnikov and Myasnikova (1985). These references deal with correlations between

the absorption coefficient and the Planck function. These references discuss assumptions that can be made to simplify the fairly intractable equations. Two references have been found that deal with the correlation $\langle I(0)I(\rho)\rangle$, Rybicki (1965, 1967). They do not take into account correlations between the absorption coefficient and the Planck function, and only consider the fluctuating parts of these two functions. In the following, we will compute $\langle I(0)I(\rho)\rangle$ - assuming no correlation between the absorption coefficient and the Planck function - but consider both the mean and fluctuating components. The increase in complexity in this approach is significant. Further work will have to deal with simplifying - yet justified - assumptions that can make the problem more tractable. Allusions to this process will be made below.

Assuming that the Planck function satisfies the Rayleigh-Jeans Law (low frequency limit), $W_B(x) = CT(x)$, where C is a constant (though a function of the frequency). Decompose the quantities into a mean and fluctuating part, $T = \langle T\rangle + T'$ and $h = \langle h\rangle + h'$, which by definition means that $\langle T\rangle = 0$ and $\langle h\rangle = 0$. Using the fact that $\langle\langle Z\rangle\rangle = \langle Z\rangle$, the integrand of equation (D12) can then be computed.

$$\begin{aligned}&[T'(x)T'(x') + \langle T(x)\rangle \langle T(x')\rangle]e^{-Q_1(x,x',\rho)}e^{-Q_2(x,x',\rho)}\\&\cdot [\langle h(x)\rangle \langle h(x')\rangle + \langle h(x)\rangle h'(x') + h'(x)\langle h(x')\rangle + h'(x)h'(x')]\end{aligned} \tag{D13}$$

Where,

$$\Theta_1 = e^{-Q_1(x,x',\rho)} = exp- \left[\int_0^x + \int_\rho^{x'+\rho} \langle h(y)\rangle\, dy\right] \tag{D14}$$

and

$$\Theta_2 = e^{-Q_2(x,x',\rho)} = exp- \left[\int_0^x + \int_\rho^{x'+\rho} \langle h'(y)\rangle\, dy\right] \tag{D15}$$

For the moment assume that the fluctuating parts of the absorption coefficient and the temperature are statistically uncorrelated. Taking the ensemble average of equation (D13) gives

$$\begin{aligned}&[\langle T'(x)T'(x')\rangle + \langle T(x)\rangle \langle T(x')\rangle]\,\Theta_1\\&\cdot [\langle h(x)\rangle \langle h(x')\rangle \langle\Theta_2\rangle + \langle h(x)\rangle \langle h'(x')\Theta_2\rangle + \langle h'(x)\Theta_2\langle h(x')\rangle\rangle + \langle h'(x)h'(x')\Theta_2\rangle]\end{aligned} \tag{D16}$$

This is a rather complicated expression, with double- and triple-correlations of the h' function. For now, consider the term, $\left\langle e^{-Q_2(x,x',\rho)}\right\rangle$. If h' is assumed to be a Gaussian random variable, then

$$\left\langle e^{-Q_2(x,x',\rho)}\right\rangle = exp\left[\frac{\Sigma^2_{Q_2(x,x',\rho)}}{2}\right] \tag{D17}$$

where,

$$\Sigma^2_{Q_2(x,x',\rho)} = \left\langle Q_2^2(x,x',\rho)\right\rangle = \left[\int_0^x \int_0^x + 2\int_0^x \int_{rho}^{x'+\rho} \int_{rho}^{x'+\rho} \langle h'(y)h'(y')\rangle\, dydy'\right] \tag{D18}$$

Note that for a homogeneous h' field, $\langle h'(y)h'(y')\rangle = R_{h'}(y'-y)$. In the first double integral make the change of variables $\eta = y' - y, \mu = (y'+y)/2$. This gives

$$\int_0^x \int_{-x}^x R_{h'}(\eta)d\eta d\mu \tag{D19}$$

If it is assumed that $R_h(\eta) \rightarrow 0$ for $|\eta| >> x$, then the integral over ηin equation (D19) can be written as

$$\int_{-x}^{x} R_{h'}(\eta)d\eta \approx \int_{-\infty}^{\infty} R_{h'}(\eta)d\eta = 2L_{h'} \left\langle h'^2(\mu) \right\rangle \tag{D20}$$

Where the integral scale of h', $L_{h'}$, is defined by

$$L_{h'} = \frac{1}{\langle h'^2(\mu) \rangle} \int_0^{\infty} R_{h'}(\eta)d\eta \tag{D21}$$

And so, equation (D19) becomes

$$\int_0^x \int_{-x}^{x} R_{h'}(\eta)d\eta d\mu \approx 2L_{h'} \int_0^x \left\langle h'^2(\mu) \right\rangle d\mu \tag{D22}$$

In a similar fashion, the other two double integrals in equation (D18), are given by

$$2\int_0^x \int_{\rho}^{x'+\rho} \langle h'(y)h'(y') \rangle \, dydy' = 2L_{h'} \int_{\rho/2}^{x+x'+\rho/2} \left\langle h'^2(\mu) \right\rangle d\mu \tag{D23}$$

and

$$\int_{\rho}^{x'+\rho} \int_{\rho}^{x'+\rho} \langle h'(y)h'(y') \rangle \, dydy' = 2L_{h'} \int_{\rho/2}^{x+x'+\rho/2} \left\langle h'^2(\mu) \right\rangle d\mu \tag{D24}$$

So finally equation (D17) becomes

$$\left\langle e^{-Q_2(x,x',\rho)} \right\rangle = exp\left\{ L_{h'} \left[\int_0^x + 2\int_{\rho/2}^{x+x'+\rho/2} + \int_{\rho}^{x'+\rho/2} \left\langle h'^2(\mu) \right\rangle d\mu \right] \right\} \tag{D25}$$

At least we can now evaluate the terms in equation (D16) - excepting for the double- and triple-correlations of the function (that will have to come at a later date). Recall that these terms are the integrand of equation (D12). Let us call this $\langle I(0)I(\rho) \rangle_1$

$$\begin{aligned} \langle I(0)I(\rho) \rangle_1 = C^2 \int_0^L \int_{\rho}^{L+\rho} \left[R_T(x'-x) + \langle T(x) \rangle \langle T(x') \rangle \right] exp\left\{ -[\int_0^x + \int_{\rho}^{x'+\rho} \langle h(y) \rangle dy] \right\} \\ \cdot \langle h(x) \rangle \langle h(x') \rangle \, exp\left\{ L_{h'} \left[\int_0^x + 2\int_{\rho/2}^{x+x'+\rho/2} + \int_{\rho}^{x'+\rho/2} \left\langle h'^2(\mu) \right\rangle d\mu \right] \right\} dxdx' \end{aligned} \tag{D26}$$

Assuming homogeneous turbulence, $R_T(x'-x) = C_T^2 g(x'-x) \cdot C_T^2$ is the intensity parameter of the turbulent temperature field - also known as the structure constant of the temperature turbulence, and $g(x'-x)$ is an assumed known functional form (e.g., Kolmogorov or von Kármán). Kabashnikov, (1985), in studying the equation for $\langle I(0) \rangle$, discusses conditions (the so-called optically thin fluctuation approximation, or OTFA) under which $\left\langle e^{-Q_2(x,x',\rho)} \right\rangle = e^{-Q_1(x,x',\rho)}$. Then equation (D26) is

$$\begin{aligned} \langle I(0)I(\rho) \rangle_1 \approx C^2 C_{T'}^2 \int_0^L \int_{\rho}^{L+\rho} \left[g(x'-x) + \langle T(x) \rangle \langle T(x') \rangle \right] \\ \cdot exp\left\{ -\left[\int_0^x + \int_{\rho}^{x'+\rho} \langle h(y) \rangle dy \right] \right\} \langle h(x) \rangle \langle h(x') \rangle \, dxdx' \end{aligned} \tag{D27}$$

In principle then, if the mean values of h can be estimated (from, say, a standard atmosphere model), and if the h-correlation terms in equation (D16) are small relative to the other terms (remains to be shown), then from equation (D27) the structure constant $C_{T'}^2$ can be estimated by the ratio:

$$\frac{\langle I(0)I(\rho)\rangle}{C^2 \int_0^L \int_\rho^{L+\rho} \left[g(x'-x) + \langle T(x)\rangle \langle T(x')\rangle\right] exp\left\{-\left[\int_0^x + \int_\rho^{x'+\rho} \langle h(y)\rangle dy\right]\right\} \cdot \langle h(x)\rangle \langle h(x')\rangle \, dxdx'} \tag{D28}$$

The denominator term can be computed a priori as a function of altitude, with the assumption that the airplane is in straight and level flight. $\langle I(0)I(\rho)\rangle$ would be calculated from the irradiance measurements at a given frequency. Evoking the Ergodic hypothesis, (replacing ensemble averages for space averages, given a homogeneous turbulent field), the average value, $\langle I(0)I(\rho)\rangle$, would be computed as a running spatial average (i.e., as the aircraft moves). Furthermore, instrumental characteristics (as a function of frequency) can be accommodated. Finally, since equation (D28) is an estimate for the structure constant at a given frequency, an averaged value of the structure constant can be constructed via an average over frequency. Note that the structure constant is frequency-independent, all the frequency dependence is on the right had side of Eq. (28).

Another approach - using the same methodology as presented above - would entail the development of a similar relationship between the power spectrum of the irradiance measurements and the spectrum of the temperature field. This would be accomplished by taking the Fourier transform of equation (D27). A third approach would be to use structure functions. The second-order structure function for the irradiance field is given by

$$D_I(0,\rho) = \left\langle [I(\rho) - I(0)]^2 \right\rangle = \left\langle I^2(\rho)\right\rangle + \left\langle I^2(0)\right\rangle - 2\langle I(0)I(\rho)\rangle \tag{D29}$$

We note that the last term in this equation is given directly by equation (D27). The first two terms of equation (D29) are given by replacing $I(0)$ by $I(\rho)$ and vice-versa, respectively. That is

$$\begin{aligned} \left\langle I^2(\rho)\right\rangle_1 \approx C^2 C_{T'}^2 \int_\rho^{L+\rho} \int_\rho^{L+\rho} \left[g(x'-x) + \langle T(x)\rangle \langle T(x')\rangle\right] \\ \cdot exp\left\{-\left[\int_\rho^{x+\rho} + \int_\rho^{x'+\rho} \langle h(y)\rangle dy\right]\right\} \langle h(x)\rangle \langle h(x')\rangle \, dxdx' \end{aligned} \tag{D30}$$

and

$$\begin{aligned} \left\langle I^2(0)\right\rangle_1 \approx C^2 C_T^2 \int_0^L \int_0^L \left[g(x'-x) + \langle T(x)\rangle \langle T(x')\rangle\right] \\ \cdot exp\left\{-\left[\int_0^x + \int_0^{x'} \langle h(y)\rangle dy\right]\right\} \langle h(x)\rangle \langle h(x')\rangle \, dxdx' \end{aligned} \tag{D31}$$

It is not clear whether using the structure function approach will result in any cancellations of the terms in equations (D16), (D27), (D30), and (D31). Simplifications often occur in the application of structure functions, especially a separation between mean and fluctuating parts, however, further analysis is required to flesh this out.

The methodology presented above assumed that the turbulence was homogeneous over the path (0,L). However, it can also cover the case of inhomogeneous turbulence with slowly

varying intensity (e.g. structure constant). As mentioned above, another avenue to investigate is the model of a fairly laminar atmosphere with a high-intensity, small patch (1-3 km wide, say) of turbulence a certain distance from the aircraft. It should be noted that this work is in a very preliminary stage; however, a sketch of the concept is given below.

Following Tourin and Krakow (1965), though reversing directions in their derivation, we consider taking the atmosphere along the sensor pointing direction and breaking it into n-distinct regions. Then $I(0) = \sum_{i=1}^{n} I(l_i)$, where l_i is the x-value for the i^{th} region. From equation (D6)

$$I(l_i) = -\int_{l_i}^{l} h(l_i) W_B(l_i) \exp\left[-\int_{l_i}^{x} h(x')dx'\right] exp\left[-\sum_{j=1}^{i}\int_{l_{j-1}}^{l_j} h(x')dx'\right] dx \tag{D32}$$

Working through all the steps, and letting $\alpha(l_k) = exp{-}h(l_k)[l_k - l_{k-1}]$, yields

$$I(l_i) = W_B(l_i)\left[\alpha(l_i) - 1\right]\prod_{j=0}^{i-1}\alpha(l_j) \tag{D33}$$

So, $I(0)$ is given by

$$I(0) = \sum_{i=1}^{n} W_B(l_i)\left[\alpha(l_i) - 1\right]\prod_{j=0}^{i-1}\alpha(l_j) \tag{D34}$$

Now assume that all the regions $i = 1, k-1$ and $i = k+1, n$ are laminar and $i = k$ is turbulent. As before, let $W_B(l_k) = CT(l_k)$, and $T = \langle T\rangle + T'$ and $h = \langle h\rangle + h'$, this gives

$$I(l_k) = \left[\langle T(l_k)\rangle + T'(l_k)\right]\left[\alpha_1(l_k) - 1\right]\prod_{j=0}^{k-1}\alpha_1(l_j) \tag{D35}$$

where

$$\alpha_1(l_m) = exp\{-\left[\langle h(l_m)\rangle + h'(l_m)\right]\left[l_m - l_{m-1}\right]\} \tag{D36}$$

Now the rest of the summation in equation (D34), will just contain the average quantities which can be estimated using a standard atmosphere (same for the average quantities in equation (D35)). The next steps could follow a similar path as that shown above: compute correlation, spectral or structure function equations - or even just computing the mean-square value of $I(0)$. These paths will have to be examined during any follow-on activity.

D.3 Estimating the impact on an aircraft

Unfortunately, the atmospheric quantity that dominates the response of an aircraft to turbulence is the vertical component of the wind vector - not the scalar temperature field. Therefore, a theoretical or empirical relationship between these two quantities must be established; specifically the connection between the intensity metrics, C_T^2 and the eddy dissipation rate to the two-thirds power, $\epsilon^{2/3}$. Given a von Kármán form for the velocity field, a straightforward relationship between $\epsilon^{2/3}$ and the variance of the velocity field, σ_w^2, can be made. Furthermore, in the airborne radar program, the relationship between the standard deviation of the velocity field (the square root of the variance) and the root-mean-square (RMS) vertical accelerations of a given aircraft was developed. Therefore, in principle, the IR sensor measurements can be related to the impact on an aircraft.

Of course, the term "in principle" hides the fact that a lot of work is required to show that these concepts are applicable to the real world and that a system can be developed (sensor and algorithms) to produce operationally useful performance metrics, e.g., probabilities of detection (PODs) and false alarm ratios (FARs). In the airborne radar program, it was found that analytical and realistic simulations of the turbulent field and the subsequent sensor measurements were invaluable in the development and testing of the turbulence detection algorithms. Of course, simulations can go only so far in this process; hence, field testing is another important component of a successful program.

D.4 Feature extraction from the sensor data

Another aspect of detecting turbulence from a passive IR sensor is feature extraction. This is in distinction from the turbulence intensity methodology described above. By "feature" we mean characteristics in the sensor data that are the result of the turbulence - and not the background. Preliminary feature extraction algorithm concepts have been applied to simulated brightness temperatures and interferogram data.

D.4.1 Brightness temperature data

Consider the severe turbulence encounter case shown in figure D1 below. The top panel in this figure is the vertical acceleration time series and the bottom panel is the temperature field. Figure D2 illustrates the brightness temperatures differences calculated from the IR sensor simulation. That is, the measured temperature field from the encounter is used to simulate the irradiances, which are then converted into brightness temperatures. The brightness temperature is computed as the temperature that satisfies, $T_B = W_B(I(0))$. The brightness temperature difference is obtained by subtracting the standard atmosphere temperature from the brightness temperature.

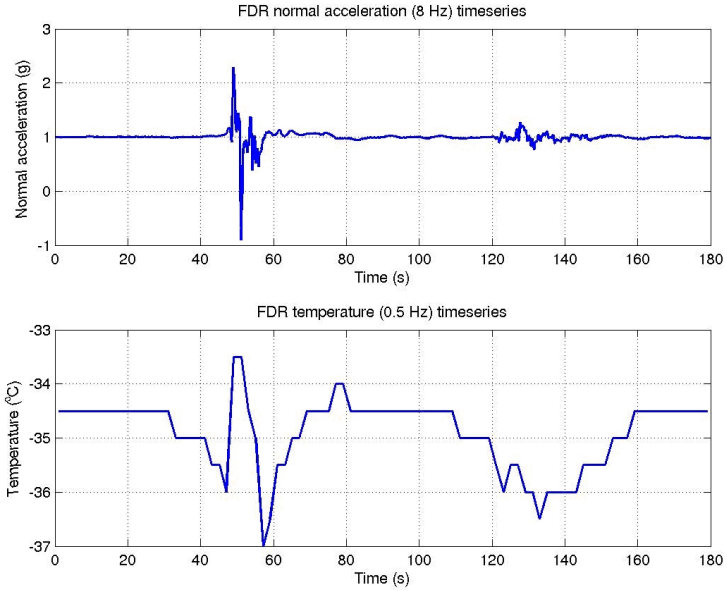

Figure D1. Vertical acceleration and temperature time series.

In figure D2 the black curve is the brightness temperature differences. The red curve is obtained by using a wavelet filter. Wavelet transforms decompose the signal into coefficients that are a function of two parameters: the "scale" parameter and the "position" parameter. As a comparison, the Fourier transform decomposes the signal into coefficients that are a function of the single parameter, wavelength. The scale parameter in the wavelet transform is akin to the wavelength parameter in the Fourier transform. The position parameter, in this case, is the wavenumber value. The advantage of wavelet transforms is that discontinuities in the data can be resolved without "smearing," as would occur with a Fourier transform. The wavelet filter used to produce the red curve in this figure is obtained by setting the coefficients above a chosen scale value to zero, and then reconstructing the signal. It can be seen that this wavelet filter acts in part like a Fourier low-pass filter, removing the higher frequency oscillations, but unlike a Fourier filter it leaves the larger-scale discontinuities intact.

The wavelet filter is useful in helping to isolate the discontinuities from the higher-scale regular oscillations; however, it does not determine which points are associated with the discontinuities. A valuable tool for performing this task is the UCAR-developed Intelligent Outlier Detection Algorithm (IODA). Referring to figure D2, it can be seen that the discontinuities in the wavelet-filtered signal can be thought of as outliers or distinct features separate, from the rest of the wavelet filtered signal. IODA is a powerful algorithm for feature detection, and as seen in figure D3 - applied to the wavelet-filtered signal - it isolates the "regular" points (inside the contours) from the discontinuities (points outside the contours). Thus, figure D3 is the same data as shown in figure D2 but on a different scale, illustrating how IODA identifies those points associated with the sharp discontinuities (points outside the contours).

D.4.2 Interferogram data

Another prototype feature-extraction algorithm was created for the interferometric data. This process contained a number of steps. The first step was to take the raw interferogram and compute local minima and maxima, in effect creating an envelope function. This can be seen in the top panel of figure D4, where the black points are the raw data and the red points are the local minima and maxima. It is easy to see that the envelope of the data between optical depths (OPD) 0.6 and 0.7 cm is quite different that that of the rest of the data. That is, the envelope in this region is very monotone, as opposed to oscillatory in the other regions. This naturally leads to the concept of creating a "difference" function, the difference being the local maxima subtracted by the local minima. This is shown in the bottom panel of figure D4. There is clearly an exponential trend in the difference function, so the next step was to remove this trend. This was accomplished by doing a line-fit in log-space, between approximately OPDs 0.05 and 0.55 - as can be seen by the red line in the second panel from the top of figure D5. The trend curve is shown in linear-space in the third panel from the top of figure D5. Finally, the bottom panel of figure D5 shows the effect of the trend removal. Since this trend-removed data is still somewhat noisy, a wavelet filter was applied to it, and the results are shown in figure D6. The oscillatory nature of the data at OPDs out to approximately 0.6 cm is quite clearly seen. Given the available time, this was as far as the methodology was worked out. However, it is clear that the next steps involve the differentiation between the oscillatory parts and the non-oscillatory parts. A preliminary attempt, using running mean filters, was made - but with mixed results. Nevertheless, we are confident that the final feature detection can be made. Obviously, more cases need to be examined, especially cases where the turbulence was further from the aircraft. At those distances, the signal becomes weaker, so having an algorithm that can extract features associated with the turbulence becomes even more important.

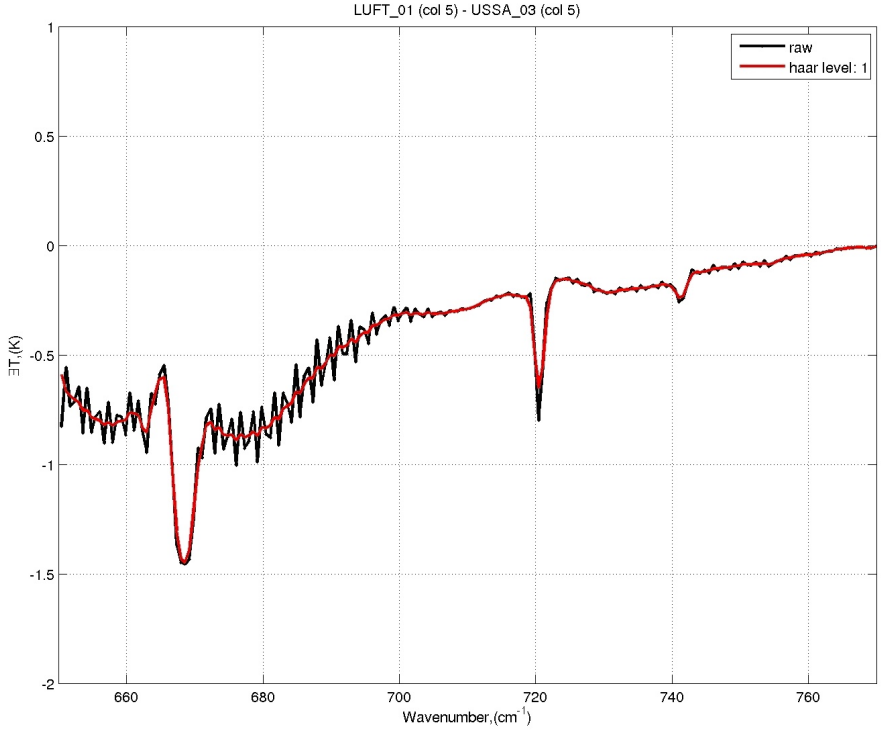

Figure D2. Brightness temperature difference and wavelet values.

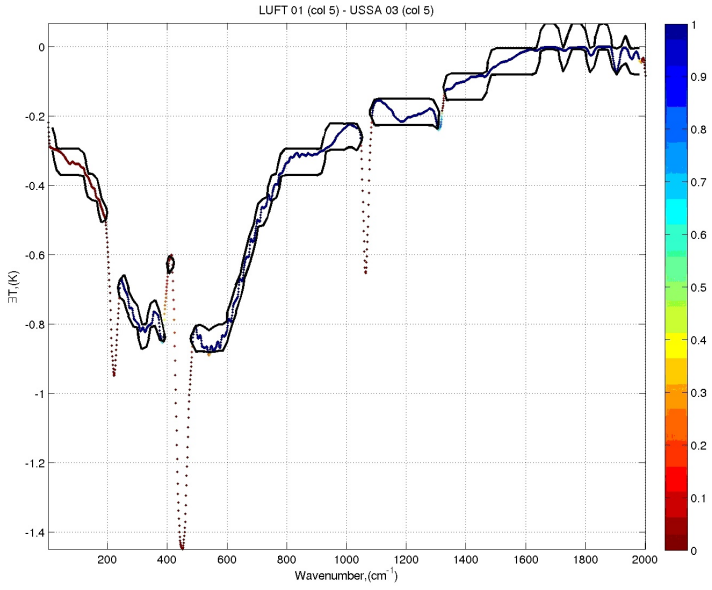

Figure D3. IODA identification of sharp discontinuities.

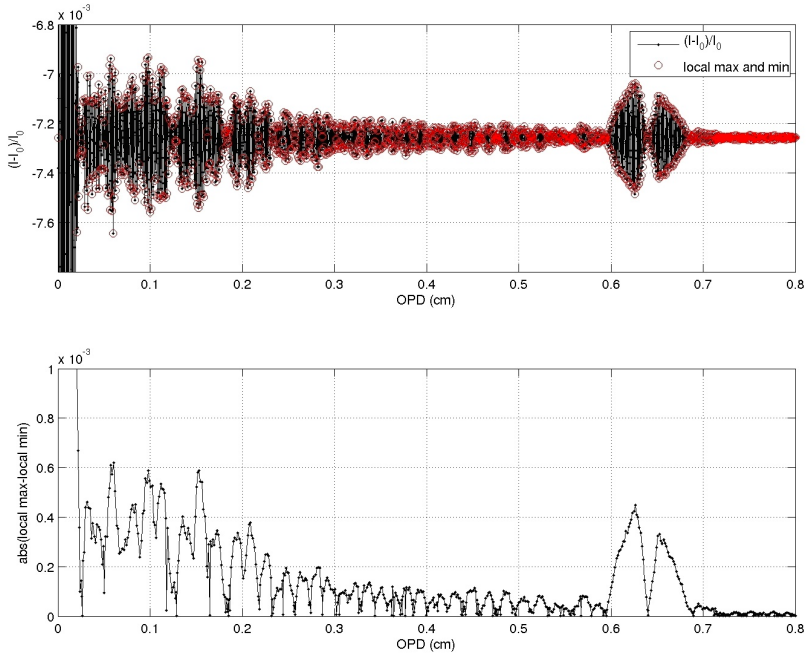

Figure D4. Interferogram, envelope function, and envelope differences.

D.5 References for Part A.

1. Gautier, D. and I. Revan, 1975: Sounding of planetary atmospheres: A Fourier analysis of the radiative transfer equation. Journal of the Atmospheric Sciences, Vol. 32, pp. 881-892.

2. Kabashnikov, V.P., 1985: Thermal radiation of turbulent flows in the case of large fluctuations of the absorption coefficient and the Planck function. Journal of Engineering Physics, vol. 49, issue 1, pp. 778-784.

3. Kabashnikov V.P. and G.I. Kmit, 1979: Influence of Turbulent fluctuations on thermal radiation. Journal of Applied Spectroscopy, vol. 31, issue 2, pp. 963-967.

4. Kabashnikov V.P. and G,I. Myasnikova, 1985: Thermal radiation in turbulent flows - temperature and concentration fluctuations. Heat Transfer - Soviet Research, vol. 17, no. 6, pp. 116-125.

5. Rybicki, G.B., 1965: Transfer of radiation in stochastic media. Research in Space Science Special Report no. 180, Smithsonian Institution - Astrophysical Observatory, Cambridge, Mass.

6. Rybicki, G.B., 1967: Radiative transfer in turbulent atmospheres: the diagnostic problem. I.A.U. Symposium no. 28, 1967.

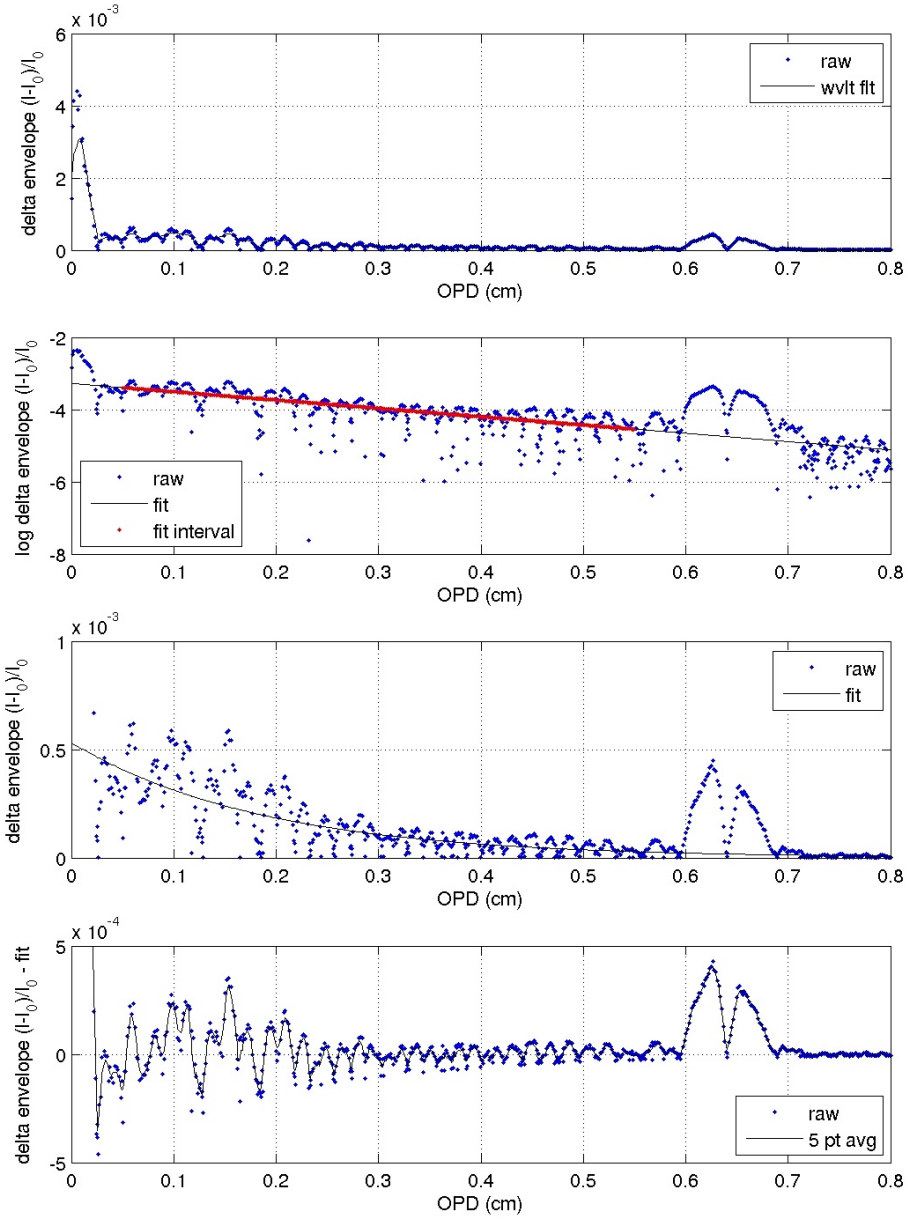

Figure D5. Difference function, trend line, trend curve, and difference signal.

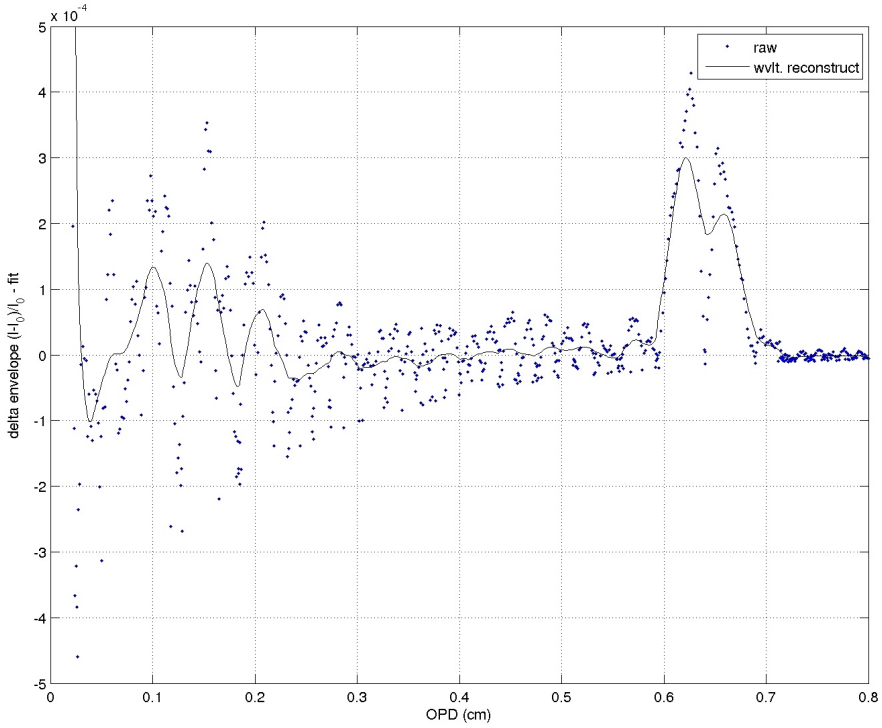

Figure D6. Wavelet filter applied to trend-removed difference function.

7. Tourin, R.H. and B. Krakow, 1965: Applicability of infrared emission and absorption spectra to the determination of hot gas temperature profiles. Applied Optics, Vol. 4, No. 2, pp. 237-242.

Part B

D.6 Inputs to FLI simulation

The FLI produces both the interferogram and the retrieved brightness temperature from the temperature and humidity profiles along the viewing axis. For airborne detection of turbulence, the FLI would observe atmospheric conditions ahead of the aircraft with a fixed line of sight with a few different elevation angles. Accurate warnings of a turbulence hazard requires a reliable connection between thee FLI signatures and the turbulence in the vertical velocity field on the scales of motion that affect a given aircraft, typically 100-1000 m. In addition, the number of false alarms must be small to gain the confidence of the pilots. So there are two fundamental research tasks that must be performed as part of the development of a reliable FLI turbulence detection algorithm:

- Develop methods to differentiate temperature signatures that are turbulent from non-turbulent spatial temperature variations, such as fronts and even waves,
- Develop a (probably statistical) connection between temperature turbulence to velocity turbulence.

These tasks can be readily addressed in a simulation environment where realistic turbulent and non-turbulent atmospheric conditions are contained in a digital data cube which can be used as input to an FLI simulation. In initial work preformed in FY06 NCAR provided Hampton University some turbulence data to be used as input to the simulations. These were in the form of three-dimensional idealized turbulence simulation volumes, and aircraft data from a commercial flight data recorder and a research aircraft, both of which experienced a strong turbulence encounter.

D.7 Idealized turbulence simulations

A first evaluation of the FLI system for turbulence detection was produced by extracting the FLI signatures from idealized high resolution numerical simulations of von Kármán turbulence. In spite of some limitations, the von Kármán turbulence spectrum has been shown to provide a reasonable approximation for localized turbulence events at mid to upper levels (Murrow et al. 1982, Murrow 1987).

D.7.1 Background

Assume that each component of the turbulent velocity field is described by a homogeneous and isotropic Gaussian random process. Then the turbulence statistics are completely defined by the longitudinal (B_{LL}) and transverse (B_{NN}) covariance functions given by (Monin and Yaglom 1975, p. 19)

$$B_{LL}(r) = \left\langle \Big[u(x) - \langle u \rangle\Big] \Big[u(x+r) - \langle u \rangle\Big]^2 \right\rangle \tag{D37}$$

$$B_{NN}(r) = \left\langle \Big[\nu(x) - \langle \nu \rangle\Big] \Big[\nu(x+r) - \langle \nu \rangle\Big]^2 \right\rangle \tag{D38}$$

where $u(x)$ and $\nu(x)$ are the velocity components along and transverse to the displacement vector $\vec{r} = (x, y, z)$, respectively, and $\langle\rangle$ denotes an ensemble average. The longitudinal

(F_L) and transverse (F_N) one-dimensional spatial spectra of the velocity field are given by (Monin and Yaglom 1975, p. 43)

$$F_L(k) = \frac{1}{2\pi}\int_{-\infty}^{\infty} e^{-ikr} B_{LL}(r)dr \tag{D39}$$

and

$$F_N(k) = \frac{1}{2\pi}\int_{-\infty}^{\infty} e^{-ikr} B_{NN}(r)dr \tag{D40}$$

For the von K*árm*án turbulence model (e.g., Hinze 1959)

$$F_L(k) = \frac{\sigma^2 L_i}{\pi(1+L_0^2k^2)^{5/6}} \tag{D41}$$

$$F_N(k) = \frac{\sigma^2 L_i(3+8L_0^2k^2)}{6\pi(1+L_0^2k^2)^{11/6}} \tag{D42}$$

where σ^2 is the variance of the given velocity component, L_0 is the outer scale of turbulence, and

$$L_i = \frac{\sqrt{\pi}\Gamma(5/6)}{\Gamma(1/3)}L_0 = 0.7468L_0 \tag{D43}$$

is the integral length scale. The approximation for high wavenumber k (Monin and Yaglom 1975, p. 355) is

$$F_L(k) = \frac{2C\epsilon^{2/3}k^{-5/3}}{3\Gamma(1/3} = 0.4977096\epsilon^{2/3}k^{-5/3} \tag{D44}$$

$$F_N(k) = \frac{8C\epsilon^{2/3}k^{-5/3}}{9\Gamma(1/3} = 0.6636128\epsilon^{2/3}k^{-5/3} \tag{D45}$$

where ϵ is the energy dissipation rate, and the Kolmogorov constant C is taken as 2.0 (Monin and Yaglom 1975 pp. 483-485). Equating the high wave number form of equation (D41) and equation (D44) produces

$$L_0 = 0.933668\sigma^3/\epsilon \tag{D46}$$

which connects the outer scale to the variance and energy dissipation rate.

The spatial statistics of the temperature field for localized turbulent events can also be approximated by the von K*árm*án model for the longitudinal velocity, i.e., the one-dimensional spatial spectrum is

$$F_T(k) = \frac{\sigma^2 L_i}{\pi(1+L_0^2k^2)^{5/6}} \tag{D47}$$

and the inertial range behavior becomes

$$F_T(k) = \frac{2C_T^2k^{-5/3}}{3\Gamma(1/3} = 0.2488548C_T^2k^{-5/3} \tag{D48}$$

where C_T^2 is the temperature structure constant.

The spatial spectra $F_q(f)$ can be related to the corresponding temporal spectra $S_q(f)$, $S_v(f)$ and $S_w(f)$ derived from in situ tower data or aircraft data assuming Taylor's frozen hypothesis is valid (Hill 1996; Wyngaard and Clifford 1977). The temporal spectra become (with $k = 2\pi f/U$)

$$S_q(f) = \frac{2\pi}{U} F_q(\frac{2\pi f}{U}) \tag{D49}$$

where U is the magnitude of the mean along stream velocity or the true airspeed of an aircraft.

D.8 Simulation of von K*árm*án turbulence

One-dimensional homogeneous and isotropic turbulence fields can be generated for a wide range of turbulent conditions by constructing many realizations of a von K*árm*án temperature field. Each realization is generated with a spectral technique that produces the exact spatial covariance defined by the parameters of a von K*árm*án model (Frehlich 1997), i.e., the random temperature is produced by generating statistically independent zero mean Gaussian random numbers for the real and imaginary parts of the Fourier coefficients. The variance of each Fourier coefficient is chosen to produce the desired spatial correlation function. The spatial realizations are calculated from the random Fourier coefficients using the Fast Fourier Transform (FFT). Each simulation produces two (one-dimensional) turbulence fields - one corresponding to the real part and the other to the imaginary part of the FFT. One simulation output (with to two realizations) was provided to Hampton University on 6 June. Each realization contained 1D temperature fluctuations in the longitudinal direction with a spacing of 1 m. This was produced using an outer scale of 2000 m and a standard deviation of 1 K, which gives a peak-to-peak variation of $4 - 5$ K. The output could be scaled up or down to correspond to different turbulence intensities. These realizations of temperature were scaled to typical temperature signals for KH instabilities observed in research aircraft measurements (Whiteway et al. 2004) and located at various distances in front of the aircraft.

The simulation algorithm is numerically efficient and can be easily extended to two- and three-dimensional random processes (Frehlich et al. 2001). In principle, the von K*árm*án model for the temperature and velocity fields could be modified to include correlations between the temperature and velocity. However, this would require more research to provide a defendable correlation functional form.

D.9 Research Aircraft Data

Since a von K*árm*án field does not provide a realistic connection between the temperature and velocity fields, examples of traces of spatial variability derived from the NCAR research aircraft were collected and provided to GTRI/HU for evaluation as ASCII data files. The test cases are described below.

D.9.1 INDOEX

The NCAR C-130 research aircraft deployed as part of the INDOEX (Indian Ocean Experiment) campaign in the tropics during 1999 contained a turbulent event (see figure D7) at an altitude of 4.8 km. This figure shows an INDOEX case with time series plots of along track velocity u, across track velocity v, vertical velocity w, temperature T, true airspeed (TAS), altitude, heading (HDG), and water vapor density ρ as a function of track distance. Data file is indoex.1. The magnitude of turbulence of interest to aircraft response is defined by the spatial spectrum of vertical velocity $S_w(k)$ as a function of the spatial wavenumber k which is shown in figure D8. This figure shows spatial spectra of u, v, w, and T from the middle half of the data of figure D7. The $k^{-5/3}$ regions are indicated by dashed vertical lines. The classical $k^{-5/3}$ spectrum is produced from about k=0.003 - 0.02 m^{-1} with an EDR value of approximately 0.30 $m^{2/3}s^{-1}$, which would put the turbulence experience in

roughly the moderate intensity category. The temperature and water vapor density have some correlated features to the enhanced vertical velocity and also to some features that are not correlated. This may be related to the conditions in the tropics.

D.9.2 T-REX cases

The new NCAR HIAPER G5 aircraft collected considerable data over the Rocky Mountains and the Sierra-Nevada Mountains in March and April of 2006 in support of the Terrain Induced Rotor Experiment (T-REX). This data was collected at a higher altitude than the INDOEX data. Case 1 is an example of a topographically-induced gravity wave (or mountain wave) recorded by the HIAPER is shown in figure D9 with the corresponding spatial spectra in figure D10. Time series plots from T-REX case 1 with along track velocity u, across track velocity v, vertical velocity w, temperature T, true airspeed (TAS), altitude, heading (HDG), and water vapor density ρ as a function of track distance are shown in figure D9. Shown in figure D10 are the corresponding T-REX spatial spectra of u, v, w, and T from the middle half of the data of figure D9. The $k^{-5/3}$ regions are indicated by dashed vertical lines. The temperature fluctuations are large and should produce a large signature in the FLI analysis. However, the vertical velocity spectrum in wavenumber region k=0.0025-0.01 m^{-1} has an EDR of about 0.012 $m^{2/3}s^{-1}$ for the vertical velocity which is a rather low turbulence intensity for aircraft induced turbulence. This is a common condition in the upper atmosphere where most of the energy is confined to larger scales, i.e., k=0.0001-0.002 m^{-1} as shown in figure D8.

Another mountain wave case (Case 2) observed by the HIAPER is shown in figure D11 with time series of along track velocity u, across track velocity v, vertical velocity w, temperature T, true airspeed (TAS), altitude, heading (HDG), and water vapor density ρ as a function of track distance. Figure D12 is the sampled spatial spectra of u, v, w, and T from the middle half of the data of figure D11. The $k^{-5/3}$ regions are indicated by dashed vertical lines. This case is for a lower altitude and with a humidity feature nearby. Again, this is a case with a large temperature variation but an EDR of only about 0.0085 $m^{2/3}s^{-1}$ from the vertical velocity spectrum in the spatial wavenumber region that affect aircraft.

D.9.3 ATReC case

During the Atlantic THORPEX Regional Campaign (ATReC) the NOAA G4 weather reconnaissance aircraft experienced severe clear-air turbulence on 6 Dec 2003 while above a region of active moist convection, to the east of a surface low pressure system off the north-east coast of the United States. This case has been analyzed in detail and numerical simulations of the event have been performed (Lane et al. 2005). The in-situ measurements from the G4 were taken at 1 Hz time resolution, and are shown in figure D13. Shown in the figure are in-situ data from the NOAA G4 aircraft between 15:20:35 and 21:43:55 UTC 6 December 2003 are time series plots of longitudinal velocity (u), transverse velocity (v), vertical velocity (w), temperature (T), true air speed (TAS), altitude (Alt), aircraft heading (HDG), and relative humidity (RH). The severe turbulence was initially encountered at approximately 20:06.This figure shows that shortly after 2000 UTC, the aircraft measured strong fluctuations in all three velocity components, especially vertical velocity, temperature, true air speed, and relative humidity. These turbulent fluctuations occurred at approximately 13.5 km altitude. Of note is the relative humidity which attains a maximum value of approximately 40%. Therefore, this turbulence did not occur within cloudy air. Nevertheless signals are obvious in the relative humidity field, but not as well-defined in the temperature field.

The in-situ measurements of velocity and temperature taken during 500 seconds surrounding the turbulence encounter were analyzed using spectral decomposition. The spec-

tral analysis shows that all of these four variables possess a well defined inertial range at scales of motion less than approximately 1800 meters, with the inertial range extending to larger scales for the horizontal velocity components and temperature. Using the method described in Sharman and Frehlich (2003), the power spectra levels are used to determine the eddy-dissipation rate $\epsilon^{1/3}$ for the three velocity components and were determined to be $\epsilon_u^{1/3}$ = 0.301 $m^{2/3}s^{-1}$ (longitudinal), $\epsilon_v^{1/3} = 0.277\ m^{2/3}s^{-1}$ (transverse), and $\epsilon_{-w}^{1/3}$=0.139 $m^{2/3}s^{-1}$ (vertical). In a similar way, C_T^2 was derived to be 0.029 $K^2m^{-2/3}$. The standard deviations of the velocity components and temperature are σ_u=10.8 m/s, σ_v=8.0 m/s, σ_w=0.93 m/s, and σ_T=1.8 K, respectively. Figure D14 is a plot of longitudinal (u), transverse (v), vertical velocity (w), and temperature (T) spatial spectra developed from the time series of data in figure D13. The area contained between the vertical dashed lines exhibit a $k^{-5/3}$ spectral slope. Note that, in this case, the turbulent velocity fluctuations were much stronger in the horizontal components compared to the vertical component, emphasizing the anisotropic behavior of discrete events.

D.10 Commercial aircraft Flight Data Recorder (FDR)

Analysis of the FDR information from 7 turbulent events produced a couple of interesting cases. Unfortunately, in all cases, humidity information is not recorded, and for several of the cases temperature information was not recorded either. The three datasets that seem to have useful information are summarized below.

D.10.1 Severe turbulence encounter case, Houston, TX, 6 Aug 2003

This turbulence encounter case occurred on August 6, 2003 at 20:57 UTC as an Airbus A340 was at cruise altitude over Walnut Ridge, AR (approximately 36:33 N latitude, 90:42 W longitude, and 31,000 ft (9448.8m)) en route to Houston, TX. The radar reflectivity (as measured by a nearby NEXRAD radar) grew from about 10 to 30 dBZ at the location of the encounter during this time, but its magnitude would likely not have appeared dangerous to the pilots. Figure D1 above shows the vertical acceleration and temperature time series from the flight data recorder.

D.10.2 Convective case over southeastern Iowa, 22 Oct 2004

A commercial aircraft encountered what was reported as severe turbulence over southeastern Iowa on 22 Oct. 2004 at FL370 at about 1636 UTC. A time series of the recorded vertical acceleration, total air temperature (TAT) and derived static air temperature (SAT) is shown in figure D15. This figure shows the FDR trace of turbulence encounter in or near convection over southeastern Iowa on 22 Oct 2004. Shown are the measured vertical acceleration (red) recorded at 8 Hz, TAT (green) recorded at 1 Hz, and corresponding SAT (blue) based on a constant Mach number during the encounter. The vertical acceleration is measured at 8 Hz on the recorder and shows a large swing from a maximum of 1.80 g to a minimum of 0.18 g in just a few seconds. The TAT is recorded at 1 Hz and shows a sharp increase at about the time of the event, followed by a more gradual decrease and then followed by a gradual recovery. But the TAT includes the effects of adiabatic compression in the temperature probe. It is related to the SAT or ambient temperature through the relation $SAT = TAT/(1 + CM^2)$, where M is the aircraft Mach number and C is a sensor specific constant. For the cruise Mach number, $SAT/TAT \approx 0.5$. Using this conversion gives the derived SAT curve in the figure.

D.10.3 Convective case over northwestern TN., 22 July 2002

A commercial B757 aircraft encountered what was reported as severe turbulence over northwestern Tennessee on 22 July 2002 at 1848 UTC at about 35,000 ft. while climbing to a destination cruise altitude of FL390. A time series of the recorded vertical acceleration and total air temperature (TAT) is shown in figure D16. This figure shows the FDR trace of turbulence encounter in or near convection over northwestern Tennessee on 22 Jul 2002. Shown are the measured vertical acceleration (red) recorded at 8 Hz and TAT (green) recorded at 1 Hz. Abscissa is 8 Hz counts from 18:45:07 UTC. The vertical acceleration is recorded at 8 Hz and shows a large swing from a maximum of 1.74 g to a minimum of -0.37 g in just a few seconds. The TAT is recorded at 1 Hz. Unfortunately, SAT was not recorded, so a conversion factor could not be applied to derive a high rate SAT during the event. However, the TAT does show a gradual decrease, as expected during a climb, prior to the event, with oscillations coincident with the event. Thus in this case there seems to be a temperature signature during the time of the event, but it is difficult to know how much of this may be due to Mach variations. Note though that this event occurs only over a very small time/space interval and is superposed on a larger more gradual temperature trend, making FLI detection of the event challenging.

D.11 Questions

The FLI also can produce estimates of the temperature and humidity profiles by careful inversion of the brightness temperature relations. Does this information offer any advantages to identifying turbulent regions? What are the unresolved technical issues?

The most pressing unresolved issue for evaluation of the FLI technique is the determination of the false alarm rate and the detection rate for typical flight conditions.

Do the EOF simulations include the effects of correlated noise and is this possible? The large dynamic range in the eigenvalues may be sensitive to correlated noise.

D.12 References for Part B.

1. Frehlich, R., 1997: Effects of wind turbulence on coherent Doppler Lidar performance. J. Atmos. Oceanic Technol., 14, 54-75.

2. Frehlich, R. G., L. Cornman, and R. Sharman, 2001: Simulation of three dimensional turbulent velocity fields. J. Appl. Meteor., 40, 246-258.

3. Hill, R. J., 1996: Corrections to Taylor's frozen turbulence approximation. Atmos. Res., 40, 153-175.

4. Hinze, J. O., 1959: Turbulence, An Introduction to its Mechanism and Theory, McGraw-Hill, 586 pp.

5. Kaimal, J. C., and J. J. Finnigan, 1994: Atmospheric Boundary Layer Flows: Their Structure and Measurement. Oxford University Press, 289 pp.

6. Lane, T. P., R. D. Sharman, H.-M. Hsu, W. D. Hall, M. A. Shapiro, R. Plougonven, and J. J. Murray, 2005: Numerical simulations of gravity waves and turbulence during the ATReC campaign. Proceedings of the 43rd Aerospace Sciences Meeting and Exhibit, AIAA 2003-194.

7. Sharman, R., and Frehlich, R., 2003: Aircraft scale turbulence isotropy derived from measurements and simulations. Proceedings of the 41st Aerospace Sciences Meeting and Exhibit, AIAA 2003-194.

8. Monin, A. S., and A. M. Yaglom, 1975: Statistical Fluid Mechanics: Mechanics of Turbulence, Volume 2, MIT Press, 874 pp.

9. Murrow, H. N., 1987: Measurements of atmospheric turbulence. In Atmospheric Turbulence Relative to Aviation, Missile, and Space Programs, NASA Conference Publication 2468, 137-154.

10. Murrow, H. N., W. E. McCain, and R. H. Ryne, 1982: Power spectral measurements of clear-air turbulence to long wavelengths for altitudes up to 14000 meters. NASA Technical Paper 1979, 161 pp.

11. Whiteway, J. A., G. P. Klaasen, N. G. Bradshaw, and J. Hacker, 2004: Transition to turbulence in shear above the tropopause. Geophysical Research Letters, 31, L02118, doi:10.1029/2003GL018509.

12. Wyngaard, J.C., and S.F. Clifford, 1977: Taylor's hypothesis and high-frequency turbulence spectra. J. Atmos. Sci., 34, 922-929.

D.13 Figures for Part B.

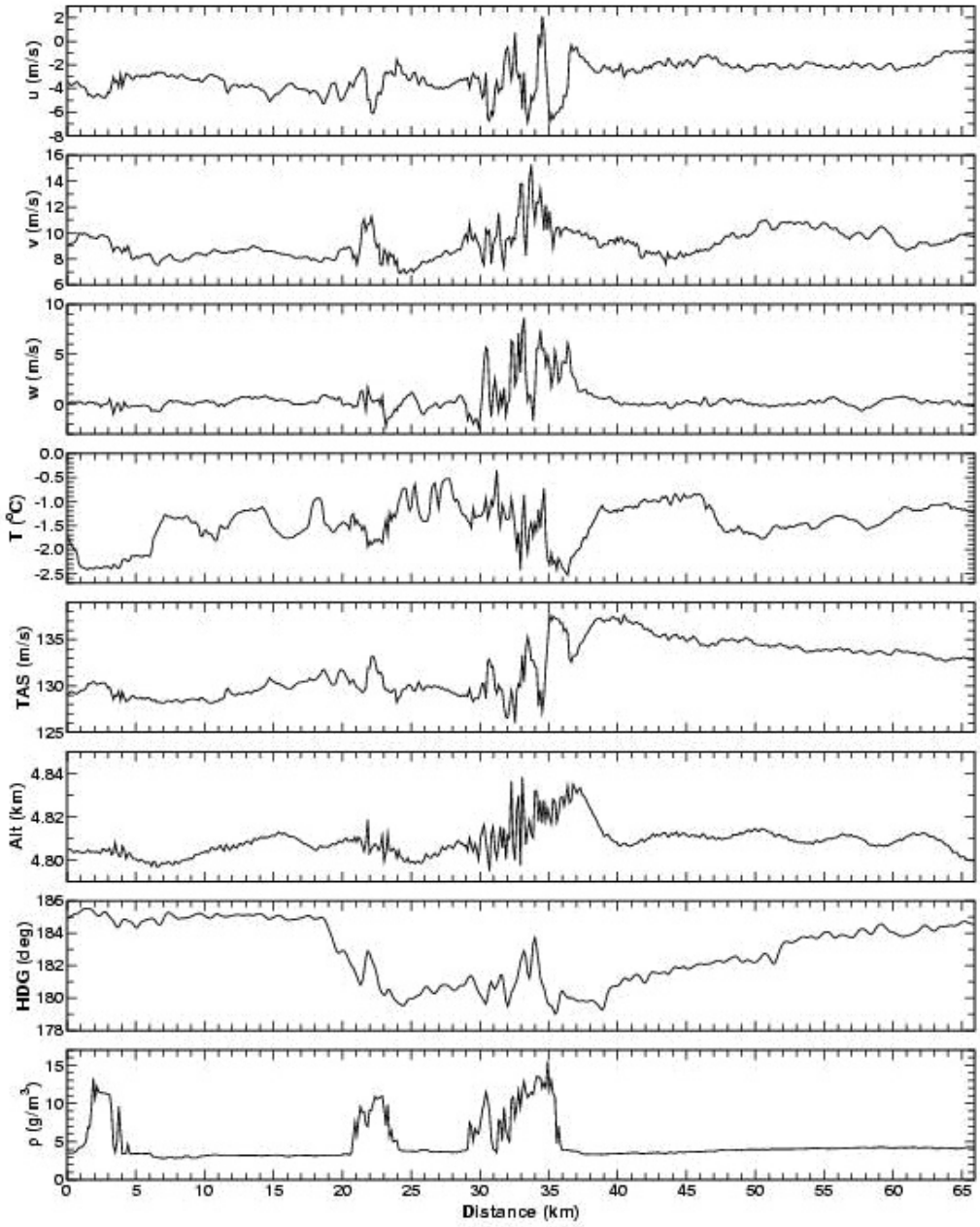

Figure D7. INDOEX case time series plots

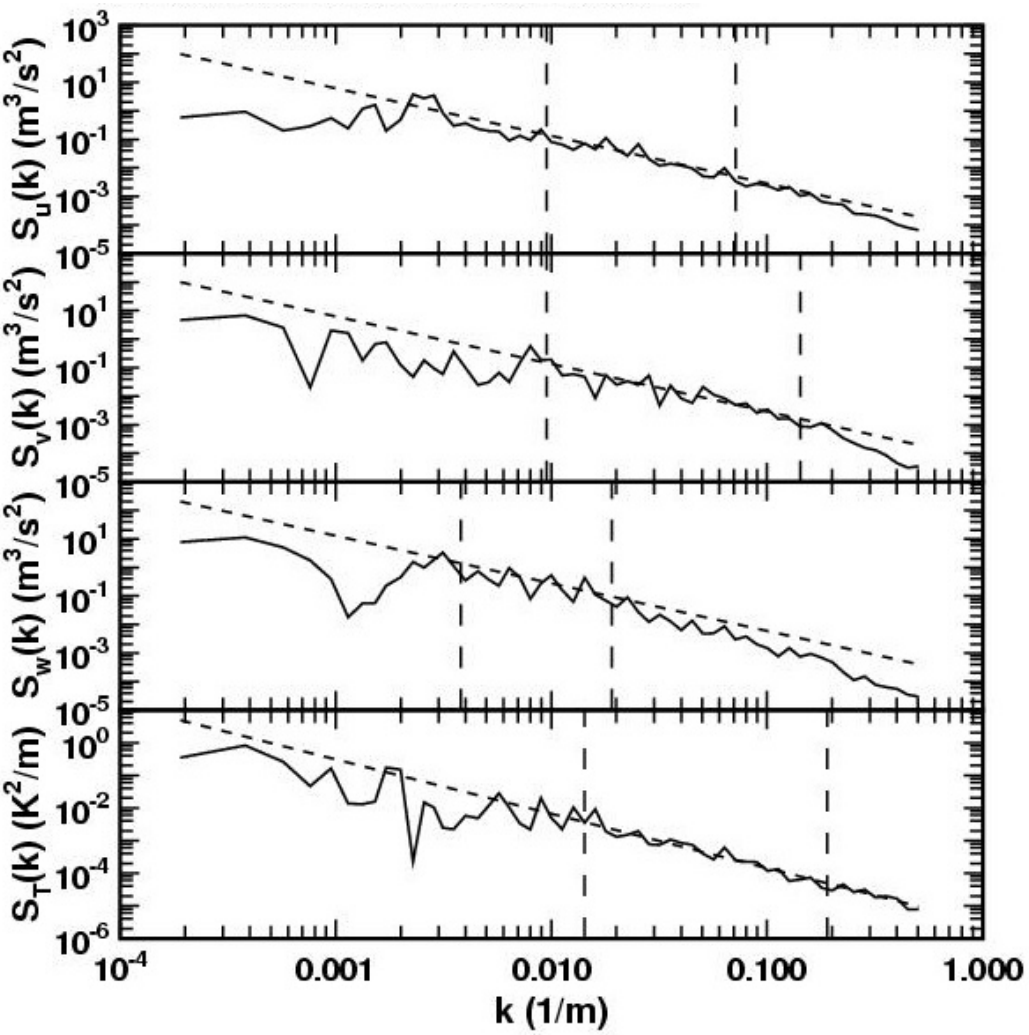

Figure D8. Sample spatial spectra of u, v, w, and T from INDOEX

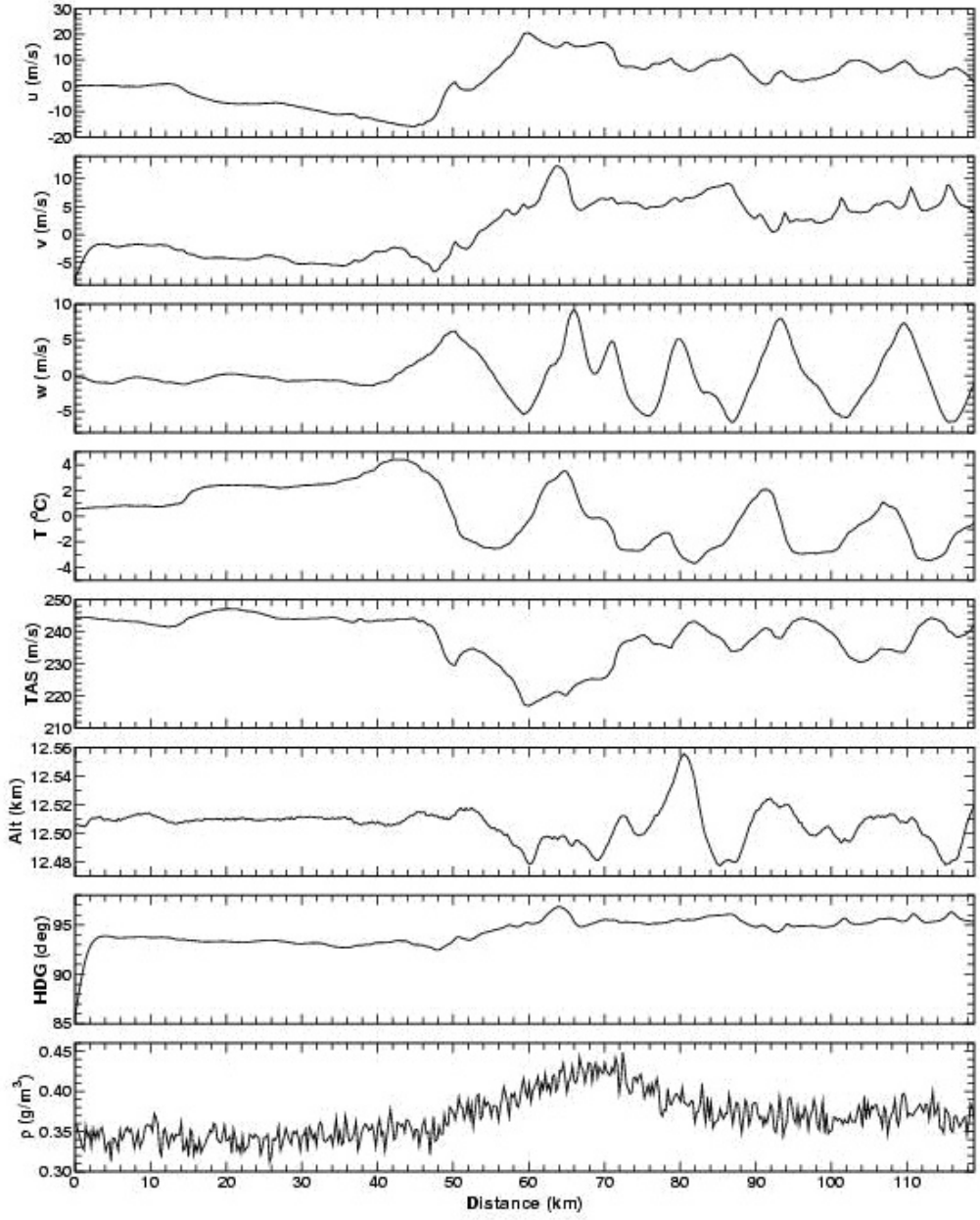

Figure D9. T-REX case 1 along track time series data.

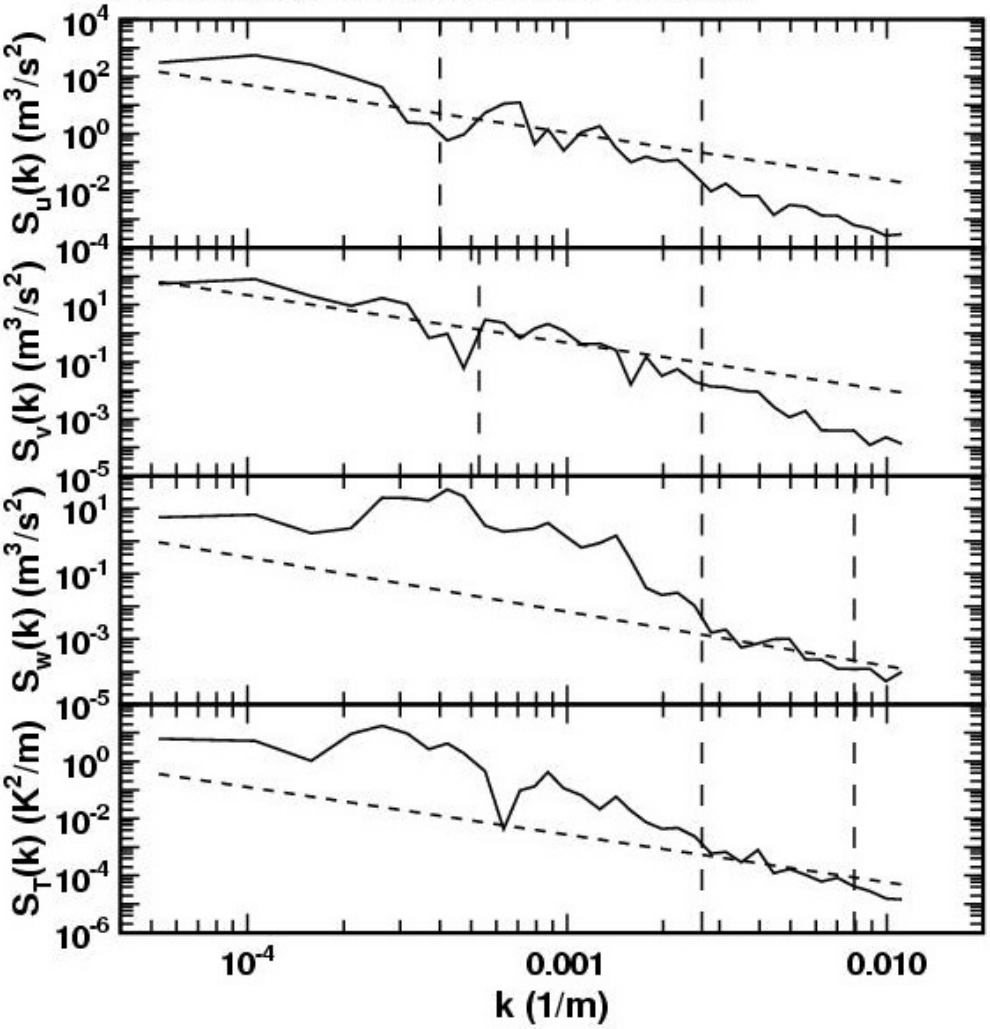

Figure D10. T-REX case 1 sample spatial spectra.

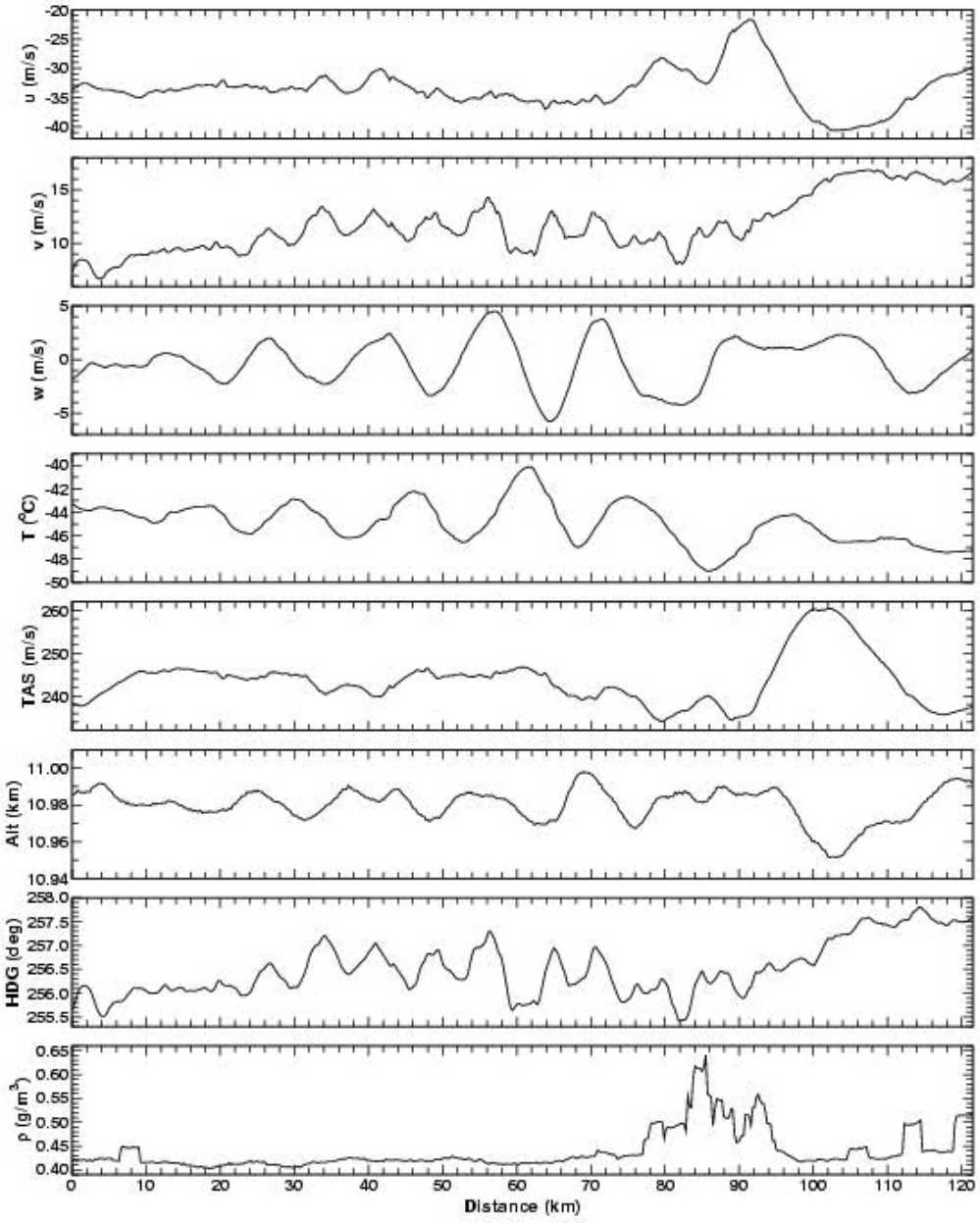

Figure D11. T-REX case 2 along track time series data.

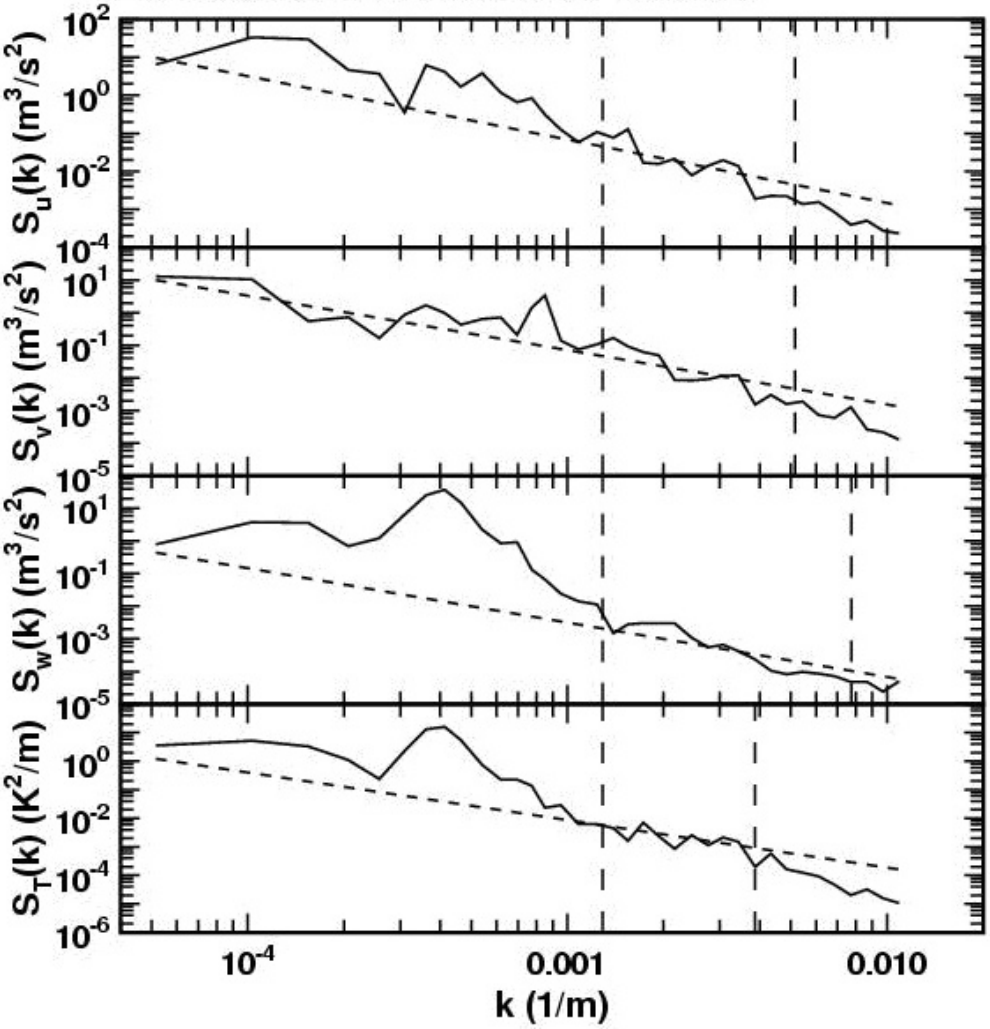

Figure D12. T-REX case 2 sample spatial spectra.

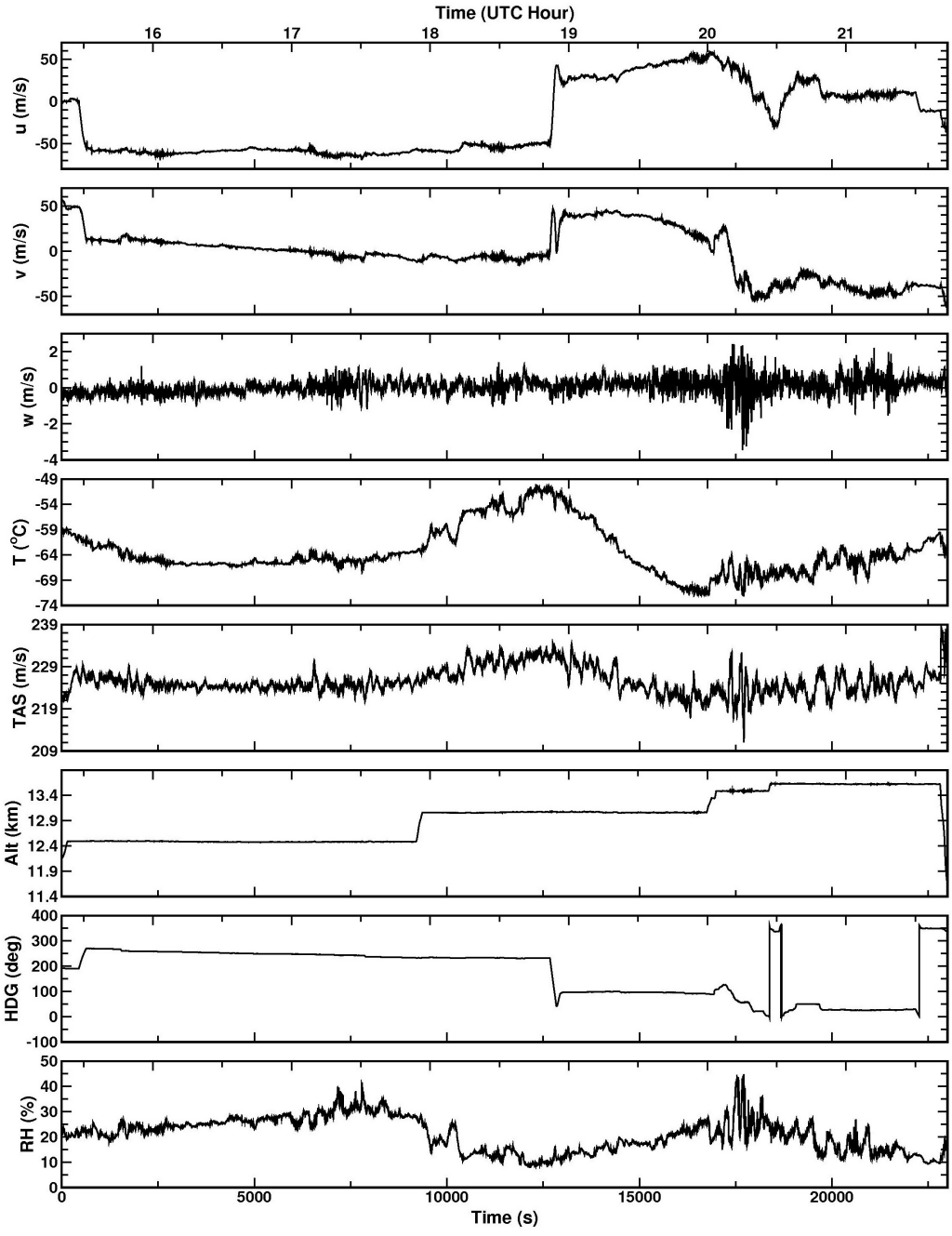

Figure D13. In-situ time series turbulence data from the NOAA G4 aircraft.

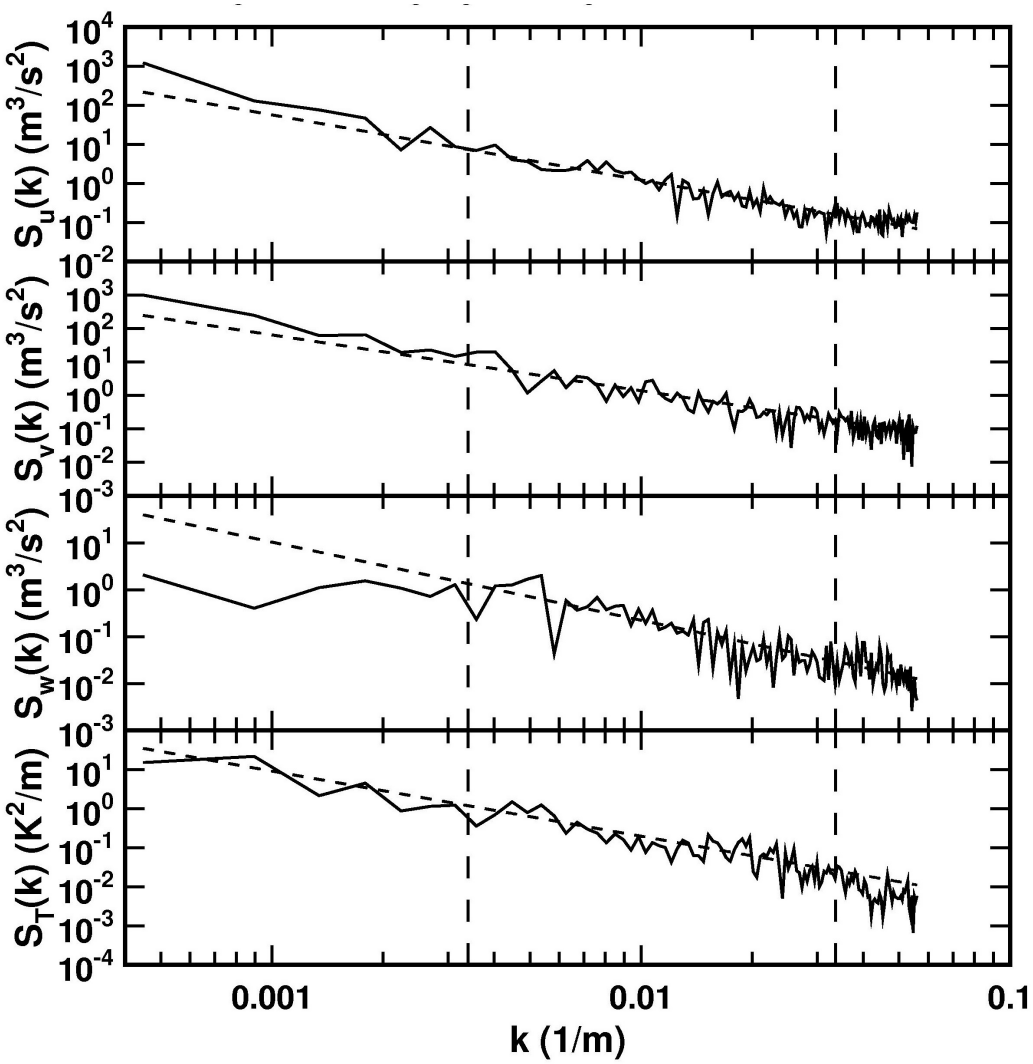

Figure D14. Spatial spectra of turbulence data from NOAA G4 aircraft.

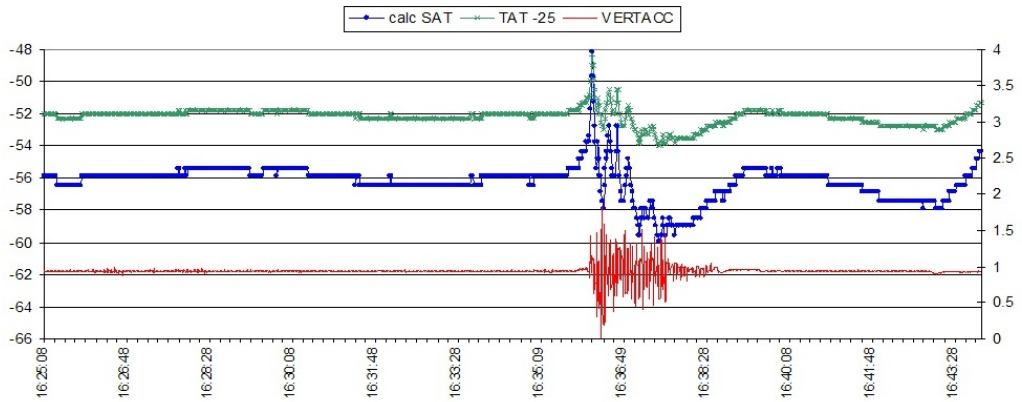

Figure D15. Commercial transport aircraft turbulence over Iowa.

Figure D16. Commercial transport aircraft turbulence over Tennessee.

Appendix E

Airport Runway Friction Detection System

William L. Smith
Science System and Applications, Inc.

George Tsoucalas
NASA Langley Research Center

E.1 Introduction

Since the beginning of commercial aviation, there have been hundreds of accidents caused by poor runway friction induced by rain, frost, and snow. During 2007 alone, 289 people were killed in two accidents related to poor runway friction. On July 17, 2007, a passenger jet skidded off a rain-slicked runway in Sao Paulo Brazil and crashed into a cargo terminal and fuel station, bursting into flames. Everyone (187) on board and 13 more on the ground were killed in the accident, killing 200 people in the country's worst aviation disaster. More recently on September 16, 2007, 89 passengers were killed when an airliner landing at Phuket Thailand in a torrential rain skidded off the runway, ran through a low retaining wall, split in two, and caught fire. Although hindsight might indicate that the pilots of these two aircraft made poor judgments in trying to land under such meteorological conditions, in most instances rain and snow do not cause the runway to be too slick for a safe landing. Thus, what is needed to prevent such tragic accidents in the future is a runway detection system, with a display in the cockpit, which can detect the runway condition just prior to touchdown and alert the pilot to the total length of runway needed after touchdown to come to a safe stop.

E.2 Potential Airborne Sensor Approach

The motivation for the detection system proposed here is the use of a Forward-Looking Interferometer (FLI) spectrometer under study for the detection of a variety of in-flight aviation weather hazards, including clear air turbulence. The FLI is a highly sensitive imaging spectrometer operating in the infrared portion of the electromagnetic spectrum. The ability to detect and quantify the runway friction condition with a FLI is based on the fact that the spectral distribution of radiance emitted by a runway within the 8-13 μm region of the spectrum has a unique spectral feature depending upon whether the runway surface is bare concrete or asphalt, or covered with water, and/or ice, and/or snow. Moreover the strength of this spectral radiance emission feature, relative to that expected for a dry runway condition, will depend on the amount of rain, ice, or snow cover, which together with the known aircraft weight and landing speed, provides a quantitative measure of the runway coefficient of friction (i.e, COF defined as the ratio of the horizontal braking to the vertical loading forces acting on aircraft tires). Using an imaging interferometer to detect the runway spectral radiance emission enables the COF to be determined over the entire length of the runway surface, providing with an accurate measure of stopping distance before the pilot of an aircraft chooses to land.

E.3 Physical Basis

The radiance observed by an imaging spectrometer takes the analytical form

$$R(\theta) = \epsilon_s \tau_s(\theta) B(T_s) + [1 - \epsilon_s]\tau_s(\theta) \int B(T) d\tau(\theta) + \int B(T) d\tau(\theta) \tag{E1}$$

where all variables are wavelength (λ) dependent. θ is the angle at which the instrument views the ground from the aircraft, ϵ_s is the emissivity of the surface which has a different spectral character for different surface conditions (e.g., dry concrete, asphalt, or various degrees of rain, frost, snow, or ice covered surfaces), B is the Planck function, which, unlike the surface emissivity, is a very smooth monotonic function of wavelength. The transmittance of the atmosphere between the aircraft and any position along the viewed path is $\tau(\theta)$, $\tau_s(\theta)$ being the transmittance of the atmosphere between the aircraft and the surface. The first term represents the contribution of the measured radiance coming from the surface and the second and third terms represent the contributions from the atmosphere. The first integral is the contribution of the down-welling radiation from the entire atmosphere above the ground that is reflected by the ground surface to the instrument, whereas the third term is the contribution of the upwelling radiance from the atmosphere between the instrument and the ground surface. For an instrument viewing the runway from an aircraft close to the runway surface across the 8-13 μm "window" portion of the spectrum where atmospheric transmittance is close to unity, equation E1 simplifies to

$$R(\theta) = \epsilon_s B(T) \tag{E2}$$

According to equation E2, the spectral character of the observed runway radiance signal will be dominated by the spectral character of runway surface emissivity, ϵ_s.

Figure E1 shows the emissivity of various types of runway surfaces in which the runway surface is either dry or saturated with pure water, snow, or ice. The runway spectral radiance distribution, formed by a mixture of these surface conditions, will be a linear combination of the spectral radiance distributions forming the mixture, where the weights are the fractions of cover by each constituent.

The unique spectral character of the radiance emission by each of these runway surface types together with the knowledge that any particular runway condition will be characterized by a linear combination of these spectral distributions enables one to determine the COF for any viewed spot under clear line of sight conditions.

E.4 Runway Stopping Distance Retrieval Algorithm

For a clear atmosphere between the aircraft and the runway surface, the retrieval of the spectral character of the surface emissivity spectrum from the observed radiance spectrum is straightforward. The system of linearized equations to be solved is

$$R_\lambda = \epsilon_\lambda B_\lambda(T_0) + \epsilon_\lambda (T - T_0) \frac{\partial B_\lambda(T)}{\partial T_0} \tag{E3}$$

where ϵ_λ is the surface emissivity, T is the true surface skin temperature, T_0 is an estimate of the surface skin temperature, such as the reported surface air temperature, and B_λ is the Planck function. Now assuming that

$$\epsilon_\lambda = \sum a_i \epsilon_{\lambda i}, i = 1, 4 \tag{E4}$$

where a_i, is the fraction of each emissivity spectrum shown in figure 1 and

$$\sum a_i = 1, i = 1, 4 \tag{E5}$$

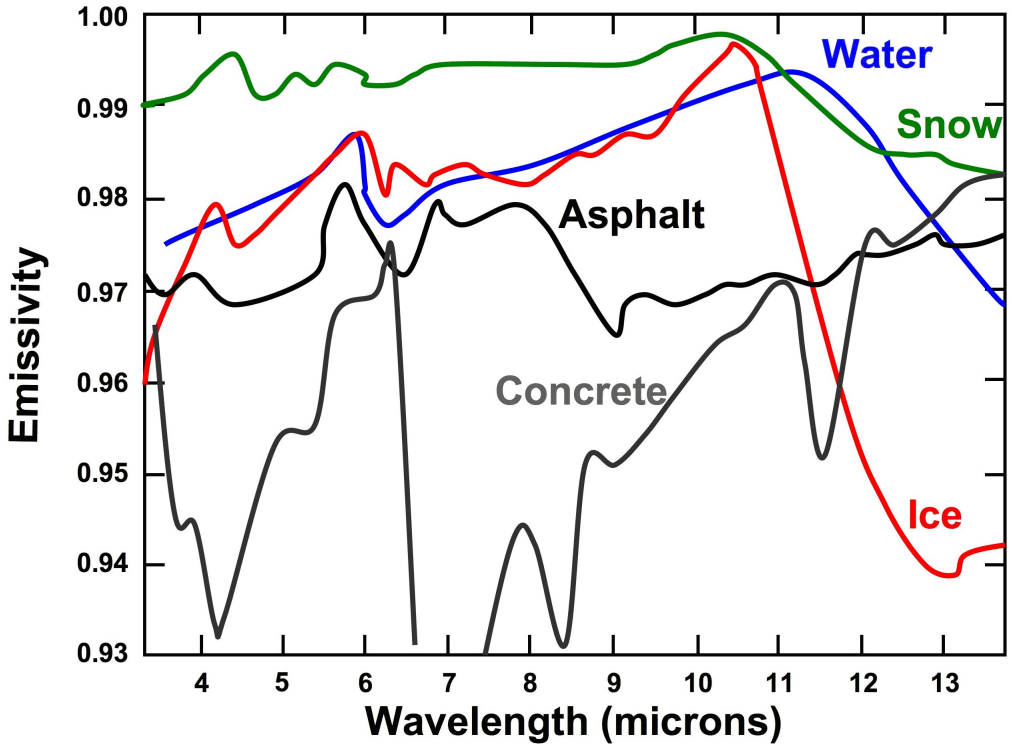

Figure E1. The spectral distribution of emissivity of various types of runway surfaces.

The combination of equations E3, E4, and E5 provide a system of $N + 1$ equations, where N is the number of spectral radiances measured, to solve for five unknowns (i.e., the four a's and T). Since an interferometer spectrometer provides hundreds of spectral radiance observations within the 8-13 μm region of the spectrum, the system is heavily over determined providing stable estimates of the unknown parameters.

The a_i's provide an estimate of the state of the runway surface from which the COF can be estimated. Given the spatial distribution of COF throughout the entire length of the runway and given the aircraft weight and landing speed characteristics, the length of runway needed for stopping can be determined, dependent on touchdown point.

E.5 Low Visibility Atmospheric Conditions

For a low visibility atmospheric condition, which often co-exists with deteriorating runway surface conditions, it has been shown that there is sufficient information in the measured radiance spectrum to account for the attenuation of the surface emitted radiance spectrum for a simple constant surface emissivity condition (i.e., emissivity equal to unity). Figure E2 shows an example of how a poor visibility ($\prec$1000 ft) ($\prec$305 m) image of a runway obscured by haze and fog can be cleared using a Principal Component analysis surface radiance retrieval algorithm. The atmospheric attenuation enhanced image of a runway with a rectangular object in the middle using radiance observations from a Forward Looking lnterferometer (FLI) were shown in Section **??**.

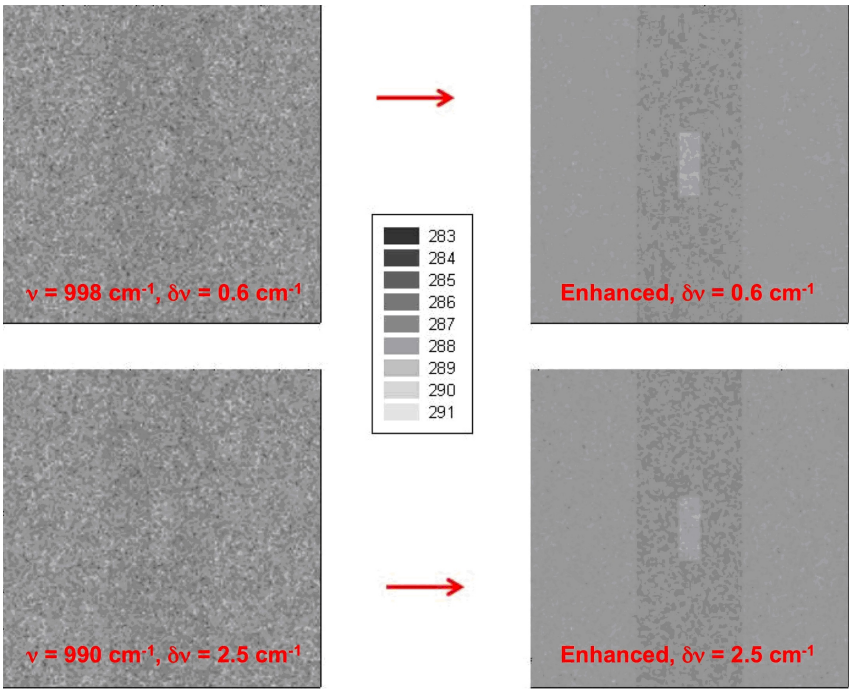

Figure E2. Runway object image enhancement.

For this simulation, the instrument was assumed to be 1000 ft (305 m) above a spectrally "black" runway surface in which the runway temperature was one degree warmer than the surrounding grass and the object in the middle of the runway surface was 2 degrees colder than the runway. The simulation shows that the spectral character if the atmospheric attenuated runway emission can be used account for the optical depth of the atmosphere between the runway surface and the aircraft mounted instrument. However, it remains

to be determined whether or not there is sufficient information in a measured atmospheric attenuated radiance spectrum emitted from a runway with a more complex surface emissivity condition, such as those shown in figure E1. However, assuming that the spectrum of aerosol and fog optical depth possesses a sufficiently different spectral and spatial character than the runway surface emissivity, and/or surrounding grass emissivity, it is possible that these two contributing components to the observed radiance spectrum can be separated given a sufficient observation of the three dimensional (x, y, λ) radiance distribution as would be obtained with an imaging forward looking interferometer spectrometer.

E.6 Conclusion

It appears to be theoretically and technically feasible that a relatively low spectral resolution ($\lambda/\delta\lambda \approx 400$) imaging FLI spectrometer, operating from an aircraft, could be used to detect the runway condition from which the COF and braking distance can be calculated. Assuming that this information could be obtained with sufficient lead-time to alert the pilot of a hazardous landing condition, slick runway airline disasters could be avoided. It is recommended that both theoretical and observational studies be performed to demonstrate the ability to determine hazardous runway conditions using an appropriate forward-looking interferometer spectrometer.

REPORT DOCUMENTATION PAGE

Form Approved
OMB No. 0704-0188

1. REPORT DATE *(DD-MM-YYYY)*	2. REPORT TYPE	3. DATES COVERED *(From - To)*
01- 10 - 2008	Technical Publication	

4. TITLE AND SUBTITLE

Applications of a Forward-Looking Interferometer for the On-board Detection of Aviation Weather Hazards

5a. CONTRACT NUMBER

5b. GRANT NUMBER

5c. PROGRAM ELEMENT NUMBER

6. AUTHOR(S)

West, Leanne; Gimmestad, Gary; Smith, William (Bill); Kireev, Stanislav; Cornman, Larry B.; Schaffner, Philip R.; and Tsoucalas, George

5d. PROJECT NUMBER

5e. TASK NUMBER

5f. WORK UNIT NUMBER

609866.02.07.07.04

7. PERFORMING ORGANIZATION NAME(S) AND ADDRESS(ES)

NASA Langley Research Center
Hampton, VA 23681-2199

8. PERFORMING ORGANIZATION REPORT NUMBER

L-19522

9. SPONSORING/MONITORING AGENCY NAME(S) AND ADDRESS(ES)

National Aeronautics and Space Administration
Washington, DC 20546-0001

10. SPONSOR/MONITOR'S ACRONYM(S)

NASA

11. SPONSOR/MONITOR'S REPORT NUMBER(S)

NASA/TP-2008-215536

12. DISTRIBUTION/AVAILABILITY STATEMENT

Unclassified - Unlimited
Subject Category 06
Availability: NASA CASI (301) 621-0390

13. SUPPLEMENTARY NOTES

14. ABSTRACT

The Forward-Looking Interferometer (FLI) is a new instrument concept for obtaining measurements of potential weather hazards to alert flight crews. The FLI concept is based on high-resolution Infrared (IR) Fourier Transform Spectrometry (FTS) technologies that have been developed for satellite remote sensing, and which have also been applied to the detection of aerosols and gasses for other purposes. It is being evaluated for multiple hazards including clear air turbulence (CAT), volcanic ash, wake vortices, low slant range visibility, dry wind shear, and icing, during all phases of flight. Previous sensitivity and characterization studies addressed the phenomenology that supports detection and mitigation by the FLI. Techniques for determining the range, and hence warning time, were demonstrated for several of the hazards, and a table of research instrument parameters was developed for investigating all of the hazards discussed above. This work supports the feasibility of detecting multiple hazards with an FLI multi-hazard airborne sensor, and for producing enhanced IR images in reduced visibility conditions; however, further research must be performed to develop a means to estimate the intensities of the hazards posed to an aircraft and to develop robust algorithms to relate sensor measurables to hazard levels. In addition, validation tests need to be performed with a prototype system.

15. SUBJECT TERMS

Hyperspectral; Turbulence; Icing; Volcanic ash; Fourier transform spectrometer; Airborne hazard detection; Aviation safety

16. SECURITY CLASSIFICATION OF:			17. LIMITATION OF ABSTRACT	18. NUMBER OF PAGES	19a. NAME OF RESPONSIBLE PERSON
a. REPORT	b. ABSTRACT	c. THIS PAGE			STI Help Desk (email: help@sti.nasa.gov)
					19b. TELEPHONE NUMBER *(Include area code)*
U	U	U	UU	107	(301) 621-0390